5-15-2014

Principles of Structure-Function Relationships Applicable To Sensing Materials — Explosives and Bio-Diagnosis

Hyun-Sook Jang
University of Connecticut - Storrs, hs84.jang@gmail.com

Principles of Structure-Function Relationships Applicable To Sensing Materials -Explosives and Bio-Diagnosis

Hyun-Sook Jang, Ph. D

University of Connecticut, 2014

Functions of nanomaterials can be strongly dependent on their structures. Therefore, the knowledge of structure-function relationship can provide important information for designing functional materials. This dissertation aims to gain fundamental knowledge through structural analysis of nano-sensing materials for explosives and bio-diagnosis in order to enhance the sensitivity.

The main project of my research involved the investigation into the fluorescence and quenching mechanisms of pyrene with a series of organic salts and/or polystyrene of a variety of architectures as well as the function of explosive detection. The major findings of this dissertation includes: (1) the formation of pyrene excimers can be enhanced by high solvent vapor pressure annealing with the polystyrene (2) tetrabutylammonium cation (TBA^+) can effectively suppress the fluorescence but hexafluorophosphate anion (PF_6^-) with TBA^+ can counteract this effect at high solvent vapor pressure driven by temperature. This process is reasoned by dynamic quenching, (3) Polystyrene can effectively lower LUMO (lowest unoccupied molecular orbit) level of pyrene, thus facilitating the detection of the nitro-aromatic explosives. This process is presumably accomplished through radiationless energy transfer from polystyrene emission to pyrene absorption resulting in

the efficient photoinduced electron transfer (PET) to explosives, (4) the diffusion coefficients of 2,4-DNT (dinitrotoluene) through pyrene/polystyrene films was evaluated and film thickness is found to be a key parameter affecting the diffusion of 2,4-DNT.

The second project mainly focused on constructing potential nanotemplates for biocompatible sensing and diagnosis by using the complexes made of phospholipid/gold nanoparticles and phospholipid/polymer. The 2-nm surface-modified gold nanoparticles can be incorporated in the phospholipid bilayers. Such template can be further developed into theranostic carriers for medical imaging or hyperthermia treatment. In addition, I have shown that lipid vesicles can interact with a triblock copolymer forming clusters of vesicles – this template can also be used as sensitive biosensors.

Principles of Structure-Function Relationships Applicable To Sensing Materials

-Explosives and Bio-Diagnosis

Hyun-Sook Jang

B.E., Sogang University, 2006

A Dissertation

Submitted in Partial Fulfillment of the Requirements

For the Degree of Doctor of Philosophy

at the

University of Connecticut

2014

2014

Approval Page

Doctor of Philosophy Dissertation

Principles of Structure-Function Relationships Applicable To Sensing Materials

-Explosives and Bio-Diagnosis

Presented by

Hyun-Sook Jang, Ph.D.

Major Advisor _____

Mu-Ping Nieh

Associate Advisor _____

Yu Lei

Associate Advisor _____

Douglas H. Adamson

Associate Advisor _____

Jing Zhao

Associate Advisor _____

Steven L. Suib

University of Connecticut

2014

DEDICATON

To my beloved mom (Sun-hee Jun), brother (Jae-hyuk Jang)

and papa (Dong-wee Jang) whom I will see for sometime in the heaven

for their dedication, encouragement and endless love.

ACKNOWLEDGEMENT

The years of pursuing my PhD in UCONN have been the most memorable time for me. There are many great people that I got to know during this period deserve my heartfelt gratitude.

First and foremost, I would like to express my sincere gratitude to Prof. Mu-Ping Nieh for his patience, insightful advice, and endless support for the research. Without him, my Ph.D. journey could have not been possible. He was a remarkably active adviser to initiate my potentials and support me with positive views. His door was always widely opened for students and ready for the discussion regardless of topics. I want to thank him that he has given a number of opportunities to expand my network outside of school by attending many national meetings, national lab experiment and National X-ray/Neutron school. I truly respect his educational philosophy and I am grateful that you were with me to get through many things together along my up and down Ph.D. life.

I also would like to thank Prof. Yu Lei for his inspiration and creative suggestions, Prof. Douglas Adamson for his support, three classes that I have taken and advice, Prof. Jing Zhao for the guidance about lifetime experiment and warm words for the encouragement and Prof. Steven Suib for his insightful suggestions and experiences about research topic. Because of their profound knowledge, I was exposed to a tremendous amount of learning opportunities. Before coming to USA, I did not have any background about this research topic, but I learned a lot from you. I truly

want to thank each of you for your valuable time to guide me, review my dissertation and to attend my final defense.

I appreciate many people for their supports and assistances with various aspects of this project: Dr. Flavio Maran (Univ. of Padova, Italy) for providing gold nanoparticles, Dr. David Uhrig (Oak Ridge National Lab) for synthesizing different architectures of polystyrenes, Dr. Hyun-Seok Cho (Univ. of Alabama) for conducting the cyclic voltammetry experiment for me, and Dr. Boualem Hammouda (NIST) for helping the neutron scattering experiment in NIST.

Indeed, I should thank to all the IMS staffs (Jack Gromek for XRD, Marcurs Giotto for NMR, Lichun Zhang and Rogers Ristau for SEM/(HR)-TEM, Gary Lavigne for fluorescence, Raman/IR spectrocopy) who not only trained me to run the instruments but also gave many great suggestions to solve my experimental challenges.

I would like to thank everyone in my group members and undergraduate students as well for working and dealing with me for all these years, especially for Ming-Li who was a great batch and lab mate (Hope you get well soon.) and Ying Liu who shared many of those experiences together. It was enjoyable to interact with Andrew Hu, Yan Xia, Wafa Aresh and Chenlu Yu as well. Also, I learned a lot from my undergraduate students (Joshua Lemkin, Rose Cersonsky, Nicholas Fleming and Naomi Tennakoon). Thanks for all the failures and results from your hands. All the best for you guys!

It was a great pleasure to be friends with the amazing people. I was lucky to meet Dr. Ying Wang who taught me about the initial experiment setup of explosives detection and Dr. Ching-Chang Chung who helped many of my experiments (XRD/SEM) initially. A special thanks goes to Aaron Baldwin for proof reading some of this dissertation. After I arrived in Storrs alone, many Korean seniors or friends in IMS/UCONN helped me to adjust my life safely. I appreciate their support and friendship of Dr. Suk-kyun Ahn, Dr. Ki-Ryong Lee and Joon-Sung Kim. I also thank all my friends and mentors from previous company and KIST in Korea and/or USA for their encouragement and just being there.

I deeply appreciate Younghee and Bob Chudy for their warmest care and thoughtful encouragement in my Storrs life. Thanks you for giving me a memorable chapter in my life with you and your family.

Finally, I wish to express my deepest gratitude to my lovely family, my mom and brother. They always trusted me undoubtedly and encouraged me with endless love during the most stressful time. I have no adequate words that can express my love to them. Their unconditional love gave me unbelievable motivation and power to accomplish my dissertation research. Thank you being my family and always love you.

TABLE OF CONTENTS

LIST OF TABLES

LIST OF FIGURES

LIST OF SCHEME

LIST OF SYMBOL

I_M (I_{mon})	Pyrene monomer emission
I_E (I_{exc})	Pyrene excimer emission
I_1/I_3	Fluorescence intensity ratio of I_1 (373±1 nm) and I_3 (385±1 nm) in the monomer emission
I_{exc}/I_{mon}	Fluorescence intensity ratio of I_{exc} (465±3 nm) and I_{mon} (395±2 nm)
$\Delta\lambda$	Degree of red-shifting in the spectra
M*	Excited state of fluorophore
Q	Quencher
F_0	Fluorescence intensity of the fluorophore in absence of quencher
τ_0	Lifetime of the fluorophore in absence of quencher
F	Fluorescence intensity and lifetime in presence of the quencher
τ	Fluorescence lifetime in presence of quencher
k	*S*um of the rate constants of all radiative and non-radiative relaxation processes
r	the center-to-center distance between fluorophore and quencher molecule
r_0	the distance of closest approach at molecular contact

S_0	the lowest-energy state of molecules
λ	wavelength of the incident beam
M	mass
h	Planck's constant
υ	velocity of light
q	The scattering vector
d	Reciprocal space
$\rho(\vec{r})$	The scattering length density
R_g	Radius of gyration of particles
P_c	Ccritical pressure
$T_{c,}$	Critical temperature
ω	Acentric factor
V	Volume of the container
Z_{THF}	Compressibility factor of THF
N_{THF}	Mole number of THF
R	Gas constant
d	Film thickness (cm),
C_o	Concentration of 2,4-DNT at t = 0
C	Concentration of 2,4-DNT at certain time during diffusion
M_t	Amount of 2,4-DNT that diffuses into the film at certain time

M_∞	Amount of 2,4-DNT that diffuses into the film at t = $_\infty$, respectively.
I_0	Fluorescence intensity in presence of the 2,4-DNT initially
I	Fluorescence intensity in presence of the 2,4-DNT at certain time
k_q	Bimolecular quenching rate constant
D_p	Diffusion coefficients of the excited fluorophore
D_q	Diffusion coefficients of quencher
p	Quenching probability per collision
R	The sum of the collision radii ($R_P + R_q$)

LIST OF ABBREVIATION

Tetryl	2,4,6-Trinitrophenyl-N-methylnitramine
2,4-DNT	2,4-dinitrotoluene
DDS	drug delivery systems
RDX	hexahydro-1,3,5-trinitro-1,3,5triazine
PETN	Pentaerythritoltetranitrate
PCS	photon correlation spectroscopy
RES	reticuloendothelial system
TBACl	Tetrabuthylammonium chloride
TBANO3	Tetrabuthylammonium nitrate
TNT	Trinitrotoluene
DHPC	1,2-dihexanoyl-sn-glycero-3-phosphocholine
DMPG	1,2-dimyristoyl-sn-glycero-3-phospho-(1'-rac-glycerol) (sodium salt)
DMPC	1,2-dimyristoyl-sn-glycero-3-phosphocholine
DPPG	1,2-dipalmitoyl-sn-glycero-3-phospho-(1'-rac-glycerol) (sodium salt)
DPPC	1,2-dipalmitoyl-sn-glycero-3-phosphocholine
1H-NMR	^{1}H-Nuclear Magnetic Resonance
DCMSS	4-dichloromethylsilylstyrene
^{13}C-NMR	^{13}C-Nuclear Magnetic Resonance
CFD	Constant Fraction Discriminator

CMC	Critical Micellation Concentrations
CV	Cyclic Voltammetry
$CDCl_3$	Deuterated cholorform
DLS	Dynamic Light Scattering
EPR	Enhanced permeation and retention effect
FRET	Fluorescence resonance energy transfer or Föster resonance energy transfer
AuNPs	Gold nanoparticles
HOMO	Highest occupied molecular orbital
HR-TEM	High-Resolution Transmission Electron Microcopy
LUMO	Lowest unoccupied molecular orbital
MW	Molecular weight
MCA	Multi-Channel Analyzer
MLVs	Multilamellar vesicles
PCT	Photoinduced charge transfer
PET	Photoinduced Electron Transfer
PEO-PPO-PEO	poly (ethylene oxide)-poly (propylene oxide)-poly (ethylene oxide)
PPO-PEO-PPO	poly (propylene oxide)-poly (ethylene oxide)-poly (propylene oxide)
PPE	Poly(phenylenethynylene)
PAH	Polyaromatic hydrocarbon
PS	Polystyrene

Py	Pyrene
Q.E.	Quenching Efficiency
RET	Resonance Energy Transfer
SEM	Scanning Eelectron Microscopy
SANS	Small Angle Neutron Scattering
SAXS	Small Angle X-ray Scattering
SERS	Surface Enhanced Raman Scattering
TBAAcetate	Tetrabuthylammonium acetate
$TBAPF_6$	Tetrabuthylammonium hexafluorophosphate
$TBABF_4$	Tetrabuthylammonium tetrafluoroborate
$TEMPF_6$	Tetraethylammonium hexafluorophosphate
HMX	Tetrahexamine tetranitramine
$THAPF_6$	Tetrahexylammonium hexafluorophosphate
THF	Tetrahydrofuran
$TMAPF_6$	Tetramethylammonium hexafluorophosphate
TMS	Tetramethylsilane
TAC	Time-to-Amplitude Converter
UV	Ultra-Violet (UV)
ULVs	Unilamellar vesicles
XRD	X-Ray Diffraction

Chapter 1.

Introduction

1.1. Explosives Detection

The demand for high sensitivity and selectivity in the detection of explosives has emerged as a result of national security risks. Explosives are classified as highly energetic materials because their decomposition is extremely exothermic, releasing tremendous amounts of heat and gas, typically within a fraction of a second. Fig.1.1.1 shows the most common explosives such as trinitrotoluene (TNT), dinitrotoluene (2,4-DNT), penta-erythritoltetranitrate (PETN), cyclotrimethylenetrinitramine (RDX) and trinitrophenyl-*N*-methylnitramine (Tetryl). In reality, it is extremely difficult to detect these explosives due to its intrinsic characteristics. First of all, the low volatility of explosives at room temperature is a limiting factor for the efficient detection. For instance, at 25°C, the saturated concentration of TNT vapor is 10 ppb and in the case of RDX it is less than 1 ppb.[1] In the field, these concentrations can never be reached since a little perturbation in air may affect the system. Indeed, some types of explosives (i.e. 2,4-DNT) tend to adsorb onto surfaces, causing reduced concentrations in the volume of sample. However, a promising property of nitroaromatic

explosives for detection is its electron accepting capability due to the electron-withdrawing nitro groups which lower the energy of the empty π* orbitals. These reduction potentials become more favorable (less negative) as nitro substitution increases, according to the series of nitrobenzene (-1.15 V), DNT (-0.9 V), and TNT (-0.7 V) *versus* the normal hydrogen electrode.[2]

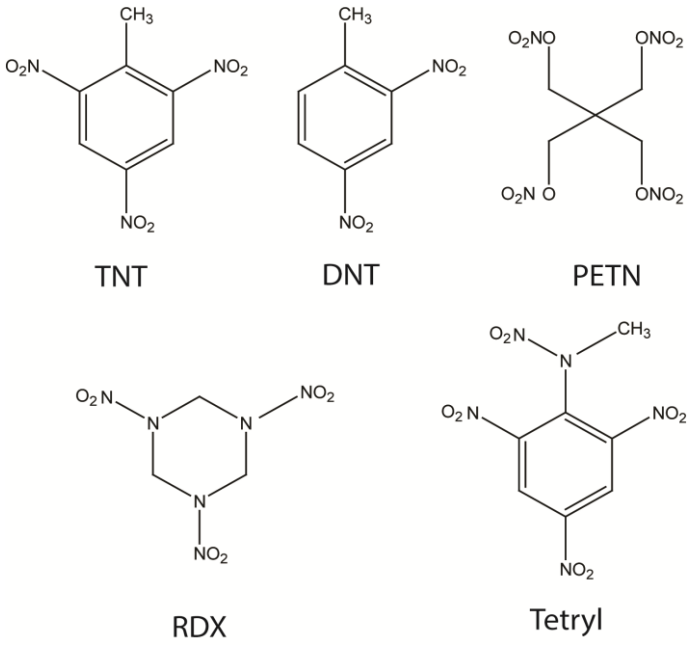

Fig.1.1.1 Structures of common explosives

Several technologies have been developed for the detection of explosives. In general, explosives detection could be separated into two separate categories, 'real-time' and ‘laboratory', which are designed for (1) screening any harmful explosive regardless of quantification and/or identification and (2) 'after-the-fact' applications along with accurate quantification and identification, respectively. The approved standard technology for trace

amounts of TNT detection involves reverse-phase HPLC with a UV detector.[3-5] However, their application in the detection of explosives is limited because they do not satisfy real-time measurements with high sensitivity and selectivity. Other methods such as surface acoustic wave sensors,[2, 6-8] sensors based on conducting or fluorescent polymers,[9-12] immunosensors[13-15], or surface plasmon resonance[16] were introduced. With the help of the electro-deficient nature of explosives, the fluorescence quenching has emerged as an effective method for detecting explosives.[2] One of the most effective materials in sensing nitro-explosives is fluorescent conjugated polymers, which promote exciton migration along the polymer chain resulting in fluorescence quenching over a long distance by a single quencher-binding, referred to as "molecular wire" amplification.[17] Also, it has been reported that a nanofibrous film composed of pyrene (Py) as a fluorophore /polystyrene (PS) /Tetrabutylammonium hexafluorophosphate ($TBAPF_6$) exhibited a high sensitivity in detecting nitro explosives through a non-direct contact method shown in Fig.1.1.2.[18] In this dissertation, an investigation of the optical properties of Py in the presence of polymers and salts to understand the detection mechanisms with explosives through different structure characterization techniques will be made.

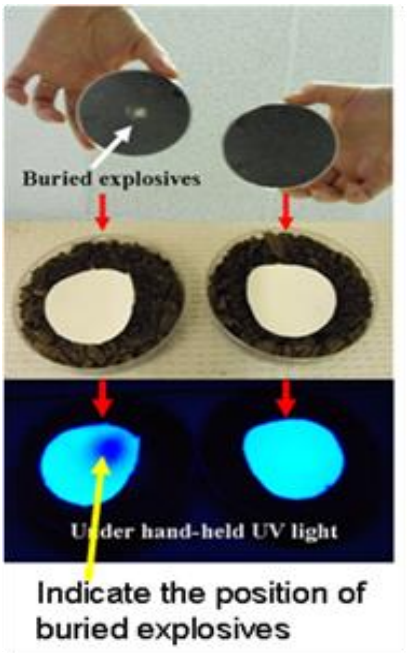

Fig 1.1.2. Fluorescence quenching of Py/PS/$TBAPF_6$ films with buried DNTs[18]

1.2. Pyrene as a Fluorophore

Pyrene ($C_{16}H_{10}$, Py) is a type of rigid, planar polycyclic aromatic hydrocarbon (PAH) made of four fused benzene rings. Due to its electron-rich structure, Py absorbs strongly in the UV region with extinction coefficients on the order of 10^4 $M^{-1}s^{-1}$.[19] Also, Py has unique optical properties compared to other fluorohphores such as different fluorescence species (i.e., monomer, excimer), high quantum yield, and long lifetime (discussed below). These characteristics allow for Py to be a potential candidate for the identification and quantification of electron-deficient compounds. In this regard, Py has been successfully applied to a variety of sensing areas including ions[20-23], explosives[18, 24], optical switches[25-26],

monitors for micelles formations[27-28], and biological probes[29-30].

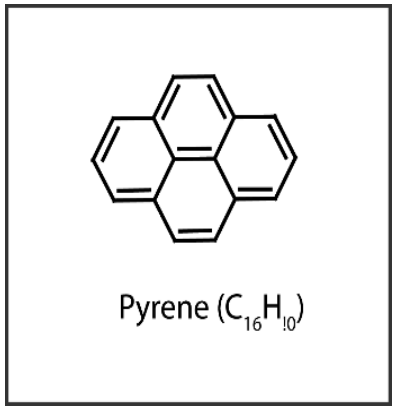

Fig. 1.2.1. Structure of Pyrene ($C_{16}H_{10}$)

1.2.1. Pyrene Monomer (I_M) and Excimer (I_E)

One of the distinct optical features of Py is its two ranges of emissions: 370 ~ 400 nm (monomer emission, I_M) and 420 ~ 600 nm (excimer emission, I_E), respectively. As a result of extensive and insightful research, the photophysical properties of Py are well-established. Py has five well-resolved major vibronic bands between 370 and 400 nm in the π–π* emission spectrum, labeled as 1, 2, 3, 4, and 5.[31-33] Those peaks are termed as a Py monomer and are very sensitive to the polarity of the surrounding environment. Measurement of the ratio of emission intensities of I_1/I_3 (I_1 at ~ 373 nm, I_3 at ~ 384 nm) in different solvents is used as an indicator for the determination of the polarity around Py ─ the higher the I_1/I_3 value, the more polar the solvent environment. It is generally believed that the solvent dependence is attributed to the symmetry distortion of the Py structures

induced by dispersion or van der Waals forces[34]. Since those vibronic bands are closely related to its absorption spectra, the absorption or excitation spectra of fluorophores was used to examine the fluorescence emission spectra. The excitation of Py from the ground-state (S_0) to the higher electronic energy levels of S_1, S_2, S_3, and S_4 can be observed around 372, 334, 272 and 243 nm, respectively, in different solvents (i.e. cyclohexane, CH_2Cl_2) and are shown in Fig. 1.2.1 and Table 1.1, respectively.[35] As the very weak intensity of $S_1 \leftarrow S_0$ band was observed in Fig.1.2.1 due to the forbidden symmetry between the S_0 and S_1 electronic states, $S_2 \leftarrow S_0$ transition peak between 334 and 345 nm has been used as an excitation wavelength for the fluorescence emission. In this regard, this thesis also focused on this $S_2 \leftarrow S_0$ transition band to study the formation of Py excimer.

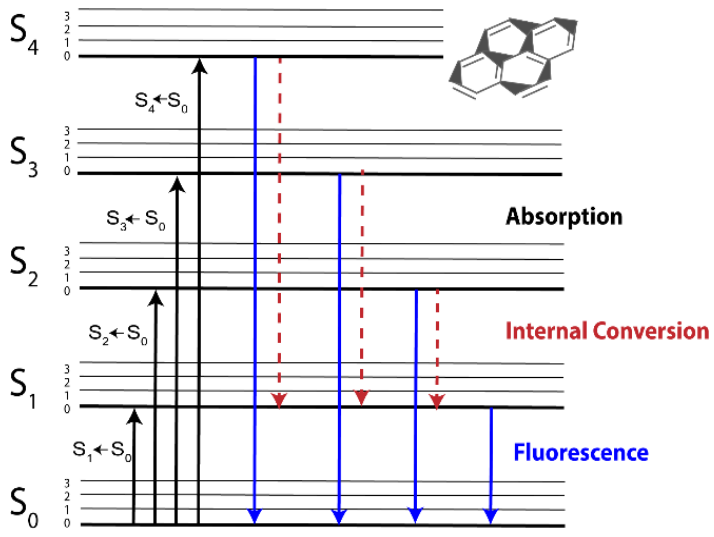

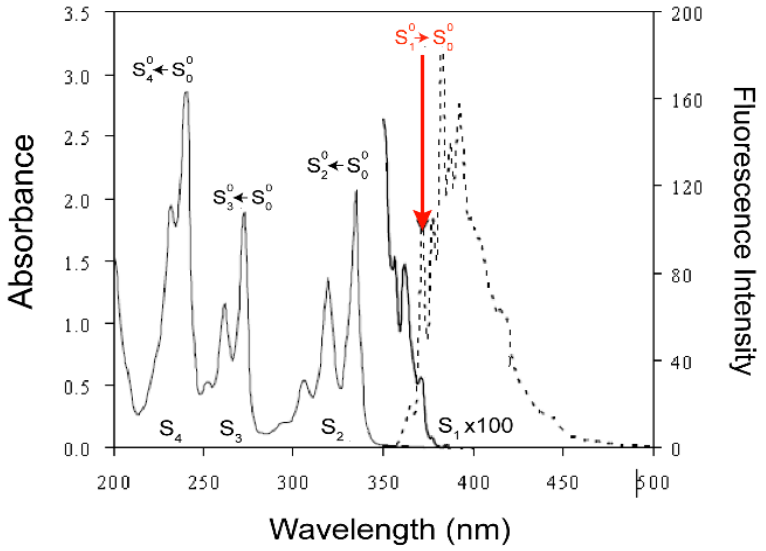

Fig 1.2.2. The Jablonsky diagram (top) and the corresponding transitions (bottom) found in the absorption (solid line) and fluorescence emission (dash line) spectra of Py in cyclohexane with [Py] =2.5×10 M and λ_{ex} = 334 nm

In addition, it should be noted that no and/or very little overlap between the absorption and fluorescence emission spectra of Py was shown in Fig. 1.2.2. This suggests the minimized energy transfer between an excited and a ground-state Py results in a high quantum yield ($\Phi_F \sim 0.65$).

Following absorptions, an excited Py monomer (Py*) can either return to the ground state with different radiation pathways, or associate with a ground-state Py. In general, where aromatic rings are involved, weak interactions can bring them within van der Waals contact distances, resulting in an excited-state dimer or "excimer".

Excited state	Ground state	Vibronic level	Wavelength	
			cm^{-1}	nm
$1L_b$	1A	1	26870	372.1623
		2	27610	362.1876
		3	28000	357.1429
		4	28420	351.8649
$1L_a$	1A	1	29680	336.9272
		2	31150	321.0273
		3	32500	307.6923
		4	33780	296.0332
$1B_b$	1A	1	36470	274.198
		2	37990	263.2272
		3	39490	253.2287
$1B_a$	1A	1	41270	242.3068
		2	42880	233.209

Table 1.1 Absorption spectra of Py in CH_2Cl_2 solution at 298K

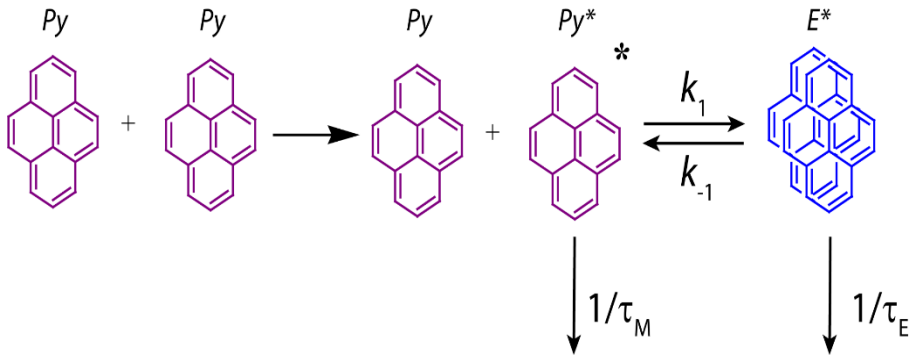

Scheme 1.1. Birks's scheme and structures of the excited Py excimer,

where τ_M and τ_E are the lifetimes of the excited Py monomer and the excimer, and k_1 and k_{-1} are the rate constants of formation and dissociation, respectively.

The process of excimer formation was described by Birks[19, 36-37] and is shown in scheme 1.1. Excimer emission typically provides a broad structureless fluorescence band without a vibrational structure in which the maximum is shifted to lower energies compared to that of the uncomplexed ("monomer") fluorophore emission. Excimers are more likely to be produced by the relatively long-lived monomer excited states. In this regard, Py shows an enhanced excimer fluorescence due to it relatively longer singlet lifetime (~ 450 ns).[38] It has known that the formation of Py excimers is governed by a diffusion controlled process.[19, 37-38] As a result, a high concentration of Py promotes the formation of Py excimers prior to self-quenching.[36] Therefore, the viscosity of solvent is a limiting factor for efficient excimer formation. Moreover, the formation of Py excimers depends on the orientation and proximity between two molecules.[38-41] The

distance between two Py molecules is roughly equivalent to that between layers of graphite (~3 to 4 A^o).[19] Fig. 1.2.3 illustrates the ground and excited state potential-energy curves for pairs of Py in a crystal.[42] In this diagram various processes are explained, including: 1) Excitation to a singlet monomer exciton state, 2) monomer exciton migration, 3) excimer formation, 4) excimer-to-excimer transfer, 5) excimer fluorescence, and 6) Franck-Condon forbidden transition between a pair of ground-state molecules and the excimer state. With this diagram one can readily understand why the excimer emission (Process 5) is red shifted relative to the monomer emission (Process 1) and why the excimer emission is so broad and structureless.[42] Due to the energy loss during the formation of excimer, the excimer can be termed as a type of fluorescence quenching. It is possible to observe the absorption process corresponding to direct excitation to the excimer state (Process 6) at 430 nm,[37] however, in reality, this absorption peak is extremely weak due to large displacements of the equilibrium configuration of the excited-state.

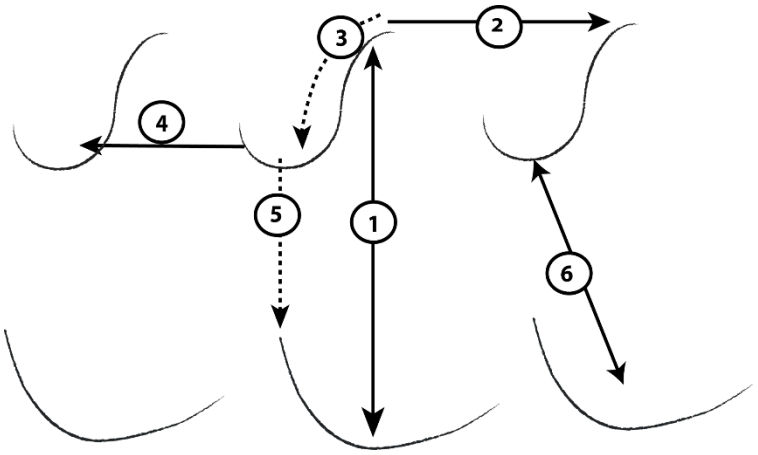

Fig. 1.2.3. Schematic diagram of the potential-energy curves for pairs of Py molecules in a crystal.

1.2.2. Ground-Associate Dimers

Py excimer is formed by a collision between the excited state of Py* and the ground state of Py. Another analogous type of collision can be present between two ground-state Py molecules. Winnink[38] suggests a theory that the ground-state could be purely repulsive, and introduces the concept of ground-state dimers in Py. The excitation and subsequent emission of these dimers is said to lead to an "associative" state. However, a ground associate dimer also possesses a broad emission like that of an excimer which makes it difficult to distinguish between the two species from the fluorescence emission spectrum. This can be explained via simple molecular orbital interaction theory as shown in Figure 2.1.4.[43-44]

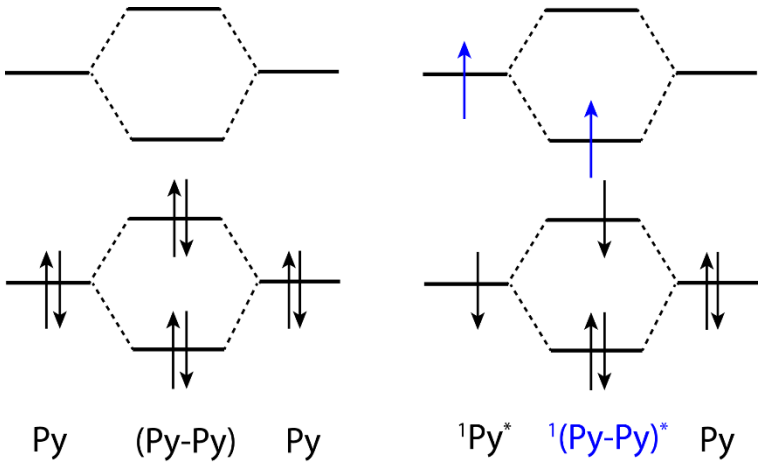

Fig 1.2.4. Molecular orbital interactions between ground state dimer and excimer

When two ground-state pyrenes interact, two electrons are stabilized and two electrons are destabilized, leading to a zero net gain in energy and thus the molecules dissociate.[44] However, in the excimer, three electrons are stabilized and only one electron is destabilized, resulting in an overall stabilization of two electrons.[43-44] A binding energy for the Py excimer was correlated to 38-42 kJ/mol in previous research.[45-47] Several experimental methods were devised to differentiate between excimers and ground-associate dimers. Winnink[38] proposed an examination of the peak-to-valley ratio (PA) of the 0-0 transition peak ($S_0 \rightarrow S_1$), in other words, the peak broadness and the degree of red-shifting ($\Delta\lambda$) of the excimer compared to that of the Py monomer in the excitation spectrum to identify the ground-associate dimer as shown in Fig.1.2.5[37] Also a relative weight rise time in the excimer fluorescence decay was suggested to determine the ground-assoicate dimer.[48-49] The formation of excimer will be delayed relative to

the initial excitation, resulting in a rise time of fluorescence decay. Those excimers formed by the direct excitation of ground associate dimers form excimer quasi-instantaneously and therefore the fluorescence decay does not exhibit a rise time as shown in Fig.1.2.6..[50]

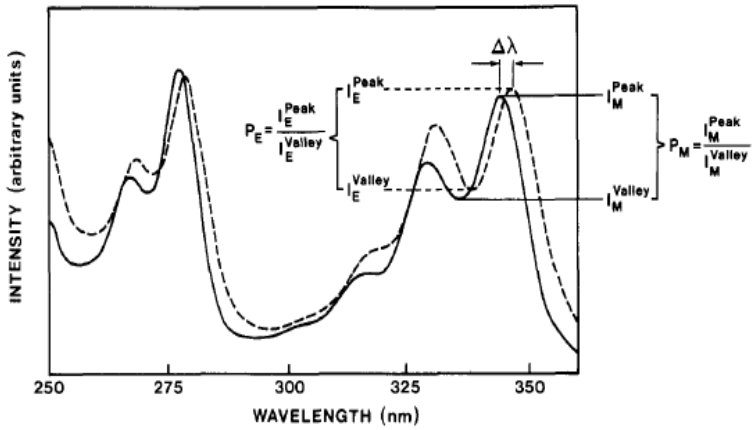

Fig.1.2.5. Normalized excitation spectra of HPC-Py/26 in water, monitored at 380 nm (monomer, full line) and at 489 nm (excimer, dashed line).[37]

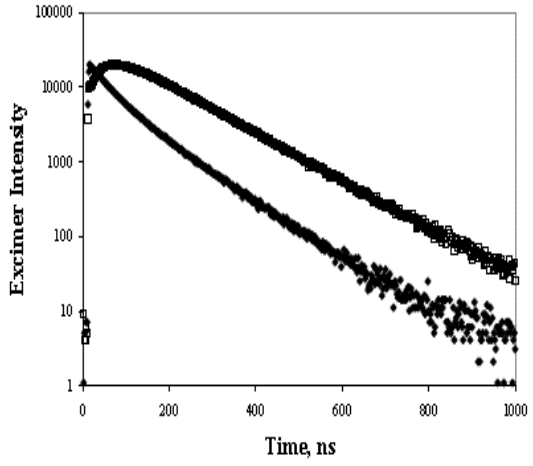

Fig. 1.2.6.. Excimer fluorescence decays excited at 344 nm and obtained at 510 nm for excimer-like (□) and monomer (♦)[49]

1.3. Fluorescence Quenching Mechanism

Fluorescence quenching is a decrease of fluorescence intensity due to other relaxation processes of an excited molecule (M*). Fluorescence quenching provides information about the environment of the fluorophore and interactions with quencher, Q. This is occasionally accompanied by a Q such as heavy ions or with paramagnetic species (e.g. O_2, $NO\cdot$). Also, a variety of processes give way to fluorescence quenching, such as

- Static and dynamic quenching (Collisional quenching)
- Excited state reactions (i.e. formation of excimer, exciplex)
- Photoinduced Electron Transfer (PET)
- (Fluorescence) Resonance Energy Transfer (RET)

1.3.1. Static and Dynamic Quenching[51]

Both static and dynamic quenching are reversible processes and occur upon collision of an excited fluorophore with heavy ions or with paramagnetic species (e.g. O_2, $NO\cdot$) and other quenchers. This collision occasionally causes an intrinsically forbidden intersystem crossing (ISC) from the first excited singlet state (S_1) to the excited triplet state (T_1) due to spin-orbit coupling with heavy atoms. The efficiency of spin-orbit coupling depends on the fourth power of the atomic number.

Static quenching can be observed in two cases: (i) non-fluorescent complexes (MQ) are formed between quencher (Q) and fluorophore (M) (ii) the Q lies within close distance to M*, so-called the radius of the effective

sphere of quenching, and then, no fluorescence of M* is observed due to quenching. This process is attributed to high concentrations of Q or viscous/rigid matrices as shown in Fig.1.3.1.

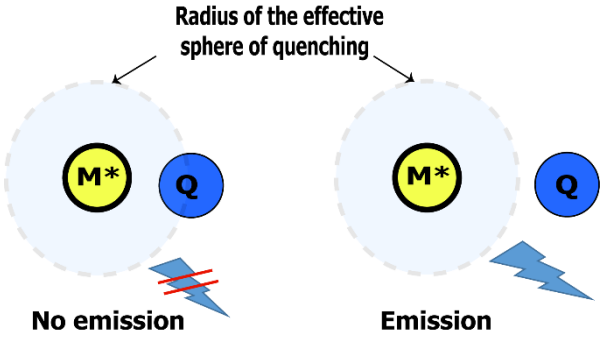

Fig.1.3.1. Static quenching of M* at high concentrations of Q or in viscous or rigid matrices.

Dynamic quenching is also known as Stern-Volmer quenching and involves a diffusion process to form an encounter pair of M*Q. The kinetics, considering rate constants of deactivation in a photophysical intermolecular interaction between M* and Q, is illustrated by the Stern-Volmer equation in Eqn. 1.1.

$$\frac{\tau_0}{\tau} = \frac{F_0}{F} = 1 + k_q \tau_0 [Q] = 1 + K_{SV}[Q] \qquad (1.1)$$

F_0 and τ_0 are the fluorescence intensity and lifetime of the fluorophore in absence of quencher, and F and τ are the fluorescence intensity and lifetime in presence of the quenching with quenching species, respectively. Plotting the ratio of F_0/F against the quencher concentration gives the Stern-Volmer quenching constant K_{SV}. Fluorescence lifetime (τ) is inversely proportional

to the sum of the rate constants, *k*, of all radiative and non-radiative relaxation processes as expressed in Eq (1.2). Also, the fluorescence intensity is related to quantum yield (Φ) and rate constants (*k*). Hence, the lifetime of fluorophores helps to distinguish quenching mechanisms of static and dynamic quenching.

$$\tau = \frac{1}{k} = \frac{1}{(k_f + k_{nr})} \tag{1.2}$$

$$\text{Intensity} \propto \Phi = \frac{\#\ of\ photon\ emittied}{\#\ of\ photon\ absorbed} = \frac{k_f}{k_f + k_{nr}} \tag{1.3}$$

According to Eqn.1.1 and 1.2 the fluorescence lifetime and therefore also the fluorescence intensity of M* depends on the concentration of Q. In this dissertation, the lifetime measurement was conducted for the determination of the quenching mechanism. While the fluorescence lifetime remains constant in the case of static quenching, a dynamic quenching will show a shorter lifetime due to more non-radiative decay pathways.

1.3.2. Quenching mechanisms

Photoinduced Electron Transfer (PET)[51]

Photoinduced electron transfer is one type of deactivation processes of the excited state fluorophore (M*), resulting in the reduced emission of fluorescence. The photoinduced electron transfer can be classified into inter- and intra-molecular transfer of electrons between an electron donor (D) and an electron acceptor (A). There could be two possible ways to transfer an electron from donor to acceptor: (i) oxidative and (ii) reductive

intermolecular electron transfer illustrated in Fig. 1.3.2. For quenching, which is related to an electron transfer process, a distance between fluorophore (M) and quencher (Q) is an important parameter. This is because quenching requires a molecular contact at the van der Walls radii for electron clouds being strongly localized. Marcus[52-53] developed an expression for the distance dependent rate of electron transfer as expressed in Eqn.1.4.

$$Q(r) = A\exp(-\beta(r - r_0)) \tag{1.4}$$

where r is the center-to-center distance between fluorophore and quencher molecule, and r_0 is the distance of closest approach at molecular contact. A and β are constants.

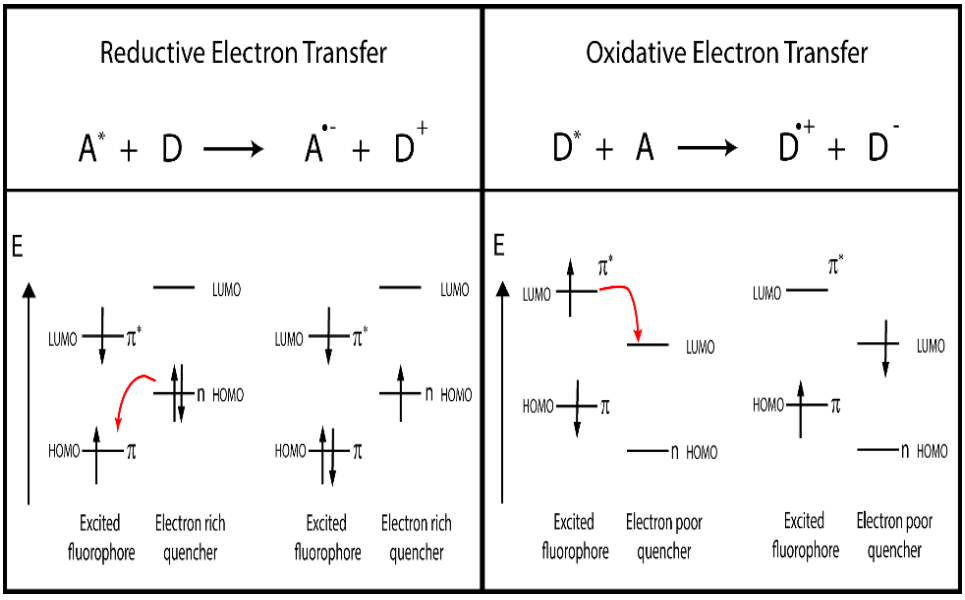

Fig. 1.3.2. Intermolecular reductive and oxidative PET between an excited fluorophore and a quencher

Fluorescence Resonance Energy Transfer (FRET)[51]

Fluorescence resonance energy transfer (FRET) is a transfer of the excited-state energy from the initially excited donor (D) to an acceptor (A). FRET efficiency is defined as the fraction of the photon energy transferred to the acceptor from the donor through long-range dipole-dipole interactions. FRET is influenced by three factors: the distance between the donor and the acceptor, the extent of spectral overlap between the donor emission and acceptor absorption spectrum (Fig. 1.3.3), and the relative orientation of the donor emission dipole moment and acceptor absorption moment.[54-56]

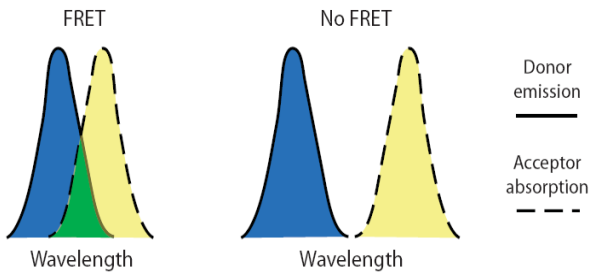

Fig. 1.3.3. Spectral overlap between donor and acceptor for FRET

The distance dependence of FRET has resulted in its widespread use to measure distances between donors and acceptors. The distance at which FRET is 50% efficient is called the Förster distance, and is typically in the range of 20-60 Å.[51, 54-55] The quenching rate of energy transfer from a donor to an acceptor (k_T) is given by Eqn.1.5.

$$Q(r) = \frac{1}{\tau_D}\left(\frac{R_0}{r}\right)^6 \qquad (1.5)$$

where τ_d is the decay time of the donor in the absence of acceptor, R_0 is the Förster distance, and r is the donor-to-acceptor distance. The rate of FRET depends strongly on distance and is inversely proportional to r^6. If the transfer rate is much faster than the decay rate, then the energy transfer will be efficient. If the transfer rate is slower than the decay rate, then little transfer will occur during the excited-state lifetime.

1.4. Bio-diagnosis

1.4.1. Current methods for cancer diagnosis and therapy

There are increasing interests in medical research regarding the use of bio-compatible molecules, such as phospholipids and nanoparticles, specifically for cancer detection and therapy. Recently, much research has been conducted using functionalized nanoparticles with antibodies that specifically bind to target analytes such as biomarkers on cancer cells.[57-61] To relate the nanoparticle and cancer cell, the characteristics of a cancer cell and normal cell needs to be understood. Unlike that of the cancer cell, normal tissues have tight, continuous vessel walls interspersed with 9 nm pores frequently and 50 nm pores infrequently.[62] Therefore, small molecules can easily penetrate all types of tissues in contrast to large molecules such as polymers that do so very slowly. However, tumor tissues, inflammatory tissues and certain organs such as the liver, spleen and bone marrow have discontinuous capillary walls and a large number of ~ 100 nm pores.[63] It is known that tumor tissues lack a lymphatic system for eliminating lipophilic and polymeric materials from them[64], therefore, once

the particles penetrate the tumor tissues, they cannot be eliminated easily. Accordingly, tumors exhibit enhanced permeation and retention effect (EPR effect) for 10-100 nm particles.[65] Hence, many nanoparticles, especially AuNPs, have used for cancer imaging, therapy purposes via special synthesis with mean sizes in 10-100 nm range.[57-58, 60-61, 66] In this dissertation, an attempt to design a possible template for the bio-diagnosis with nanoparticle and bio-compatible molecules via self-assembly is done.

1.5. Dissertation Objective

Overall, the dissertation will be divided into two projects possibly applicable to explosives detections and bio-diagnosis.

Throughout ***Part I***, the optical properties of Py applicable to detecting explosives (i.e.2,4-DNT) via fluorescence quenching techniques in the presence of different film preparation methods, molecular structures of salts (i.e. cation, anion) and architectures of polystyrene (i.e., linear, centipede and 4-arm star) are examined.

Interestingly, Py has been studied extensively previously due to its intrinsic optical properties (i.e. absorbance, excimer, and polarity). The important background of this dissertation was reviewed in ***Chapter 1***.

In ***Chapter 2***, the instrumental methods for structure characterization (i.e. fluorescence, lifetime, scattering and electron microscopy) will be introduced.

In ***Chapter 3***, the effect of film preparation methods on the formation of Py excimer in the presence of PS and $TBAPF_6$ will be discussed, with focus on

three important parameters – evaporation rate, temperature and solvent vapor pressure – that most likely influence the formation of Py excimers carefully examined.

In ***Chapter 4***, a variety of anion structures (i.e., PF_6^-, BF_4^-, $Acetate^-$, NO_3^-, and Cl^-) and cation chain lengths (i.e. TMA^+, TEA^+, TBA^+, THA^+) were introduced to examine interactions between Py and salts for the formation of Py excimer in solution and solid state, respectively. The fluorescence lifetime measurement was conducted to determine a possible quenching mechanism.

In ***Chapter 5***, the function of PS with Py are investigated for explosive detections through fluorescence quenching. A variety of molecular weights (i.e., 2.5K, 35K, 192K, 350K and 900K) and architectures (i.e, linear, centipede and 4-arm star) of PS were introduced to determine a quenching process between Py/PS films and 2,4-DNT. Electrical and optical properties of Py/PS film were also measured to confirm the HOMO-LUMO level and bandgap of Py/PS films. Based on these results, the diffusivities of 2,4-DNT in vapor phase to the Py/PS films were evaluated from time-resolved fluorescence quenching with two different film thicknesses of 110 and 560 nm, respectively.

Part II focuses on designing a simple and sustainable platform for bio-diagnosis with nanoparticle or biocompatible polymer and phospholipids via self-assembly.

In ***Chapter 6*** the incorporation of hydrophobated AuNPs into nano-disc composed of lipids mixtures were attempted via environment-friendly self-assembly templates. The size of particle and morphology were confirmed by SAXS, light scattering and (HR)-TEM.

Lastly, in ***Chapter 7,*** the self-linked DPPC liposomes with tri-blockcopolymer of PPO-PEO-PPO (Pluronic®) was attempted. The various parameters of defect, charge, curvature of liposomes and ratio of polymer to lipids were examined via dynamic light scattering.

1.6. References

1. Östmark, H.; Wallin, S.; Ang, H. G., Vapor Pressure of Explosives: A Critical Review. *Propellants, Explosives, Pyrotechnics* **2012,** *37* (1), 12-23.
2. Toal, S. J.; Trogler, W. C., Polymer sensors for nitroaromatic explosives detection. *Journal of Materials Chemistry* **2006,** *16* (28), 2871-2883.
3. Goodpaster, J. V.; McGuffin, V. L., Fluorescence quenching as an indirect detection method for nitrated explosives. *Analytical chemistry* **2001,** *73* (9), 2004-2011.
4. Nelson, P., Index to EPA test methods, April 2003 revision. US Environmental Protection Agency, Region 1, Boston. **2003**.
5. Goodpaster, J. V.; McGuffin, V. L., Separation of nitramine and nitroaromatic explosives by capillary liquid chromatography. *Journal of liquid chromatography & related technologies* **2001,** *24* (13), 1965-1978.
6. Kannan, G. K.; Nimal, A. T.; Mittal, U.; Yadava, R. D. S.; Kapoor, J. C., Adsorption studies of carbowax coated surface acoustic wave (SAW) sensor for 2,4-dinitro toluene (DNT) vapour detection. *Sensors and Actuators B: Chemical* **2004,** *101* (3), 328-334.

7. Kannan, O.; Bhalla, R.; Kapoor, J.; Nimal, A.; Mittal, U.; Yadava, R., Detection of landmine signature using SAW-based polymer-coated chemical sensor. *Defence Science Journal* **2004,** *54* (3), 309-315.

8. Yang, X.; Du, X.-X.; Shi, J.; Swanson, B., Molecular recognition and self-assembled polymer films for vapor phase detection of explosives. *Talanta* **2001,** *54* (3), 439-445.

9. Chang, C.-P.; Chao, C.-Y.; Huang, J. H.; Li, A.-K.; Hsu, C.-S.; Lin, M.-S.; Hsieh, B. R.; Su, A.-C., Fluorescent conjugated polymer films as TNT chemosensors. *Synthetic Metals* **2004,** *144* (3), 297-301.

10. Swager, T. M.; Zheng, J., Poly (arylene ethynylene) s in chemosensing and biosensing. In *Poly (arylene etynylene) s*, Springer: **2005**, pp 151-179.

11. Yang, J.-S.; Swager, T. M., Porous Shape Persistent Fluorescent Polymer Films: An Approach to TNT Sensory Materials. *Journal of the American Chemical Society* **1998,** *120* (21), 5321-5322.

12. Yang, J.-S.; Swager, T. M., Fluorescent porous polymer films as TNT chemosensors: electronic and structural effects. *Journal of the American Chemical Society* **1998,** *120* (46), 11864-11873.

13. Shriver-Lake, L. C.; Charles, P. T.; Kusterbeck, A. W., Non-aerosol detection of explosives with a continuous flow immunosensor. *Analytical and bioanalytical chemistry* **2003,** *377* (3), 550-555.

14. Altstein, M.; Bronshtein, A.; Glattstein, B.; Zeichner, A.; Tamiri, T.; Almog, J., Immunochemical approaches for purification and detection of TNT traces by antibodies entrapped in a sol-gel matrix. *Analytical chemistry* **2001,** *73* (11), 2461-2467.

15. Anderson, G. P.; Moreira, S. C.; Charles, P. T.; Medintz, I. L.; Goldman, E. R.; Zeinali, M.; Taitt, C. R., TNT detection using multiplexed liquid array displacement immunoassays. *Analytical chemistry* **2006,** *78* (7), 2279-2285.

16. Sylvia, J. M.; Janni, J. A.; Klein, J.; Spencer, K. M., Surface-enhanced Raman detection of 2, 4-dinitrotoluene impurity vapor as a marker to locate landmines. *Analytical chemistry* **2000,** *72* (23), 5834-5840.

17. Swager, T. M., The Molecular Wire Approach to Sensory Signal Amplification. *Accounts of Chemical Research* **1998,** *31* (5), 201-207.

18. Wang, Y.; La, A.; Ding, Y.; Liu, Y.; Lei, Y., Novel Signal-Amplifying Fluorescent Nanofibers for Naked-Eye-Based Ultrasensitive Detection of Buried Explosives and Explosive Vapors. *Advanced Functional Materials* **2012,** *22* (17), 3547-3555.

19. Birks, J. B., *Photophysics of Aromatic Molecules*. Wiley: London, **1970**.

20. Santos-Figueroa, L. E.; Moragues, M. E.; Climent, E.; Agostini, A.; Martinez-Manez, R.; Sancenon, F., Chromogenic and fluorogenic chemosensors and reagents for anions. A comprehensive review of the years 2010-2011. *Chemical Society Reviews* **2013,** *42* (8), 3489-3613.

21. Xu, Z.; Singh, N. J.; Lim, J.; Pan, J.; Kim, H. N.; Park, S.; Kim, K. S.; Yoon, J., Unique Sandwich Stacking of Pyrene-Adenine-Pyrene for Selective and Ratiometric Fluorescent Sensing of ATP at Physiological pH. *Journal of the American Chemical Society* **2009,** *131* (42), 15528-15533.

22. Veale, E. B.; Gunnlaugsson, T., Fluorescent sensors for ions based on organic structures. *Annual Reports Section "B" (Organic Chemistry)* **2010,** *106* (0), 376-406.

23. Kim, H. N.; Ren, W. X.; Kim, J. S.; Yoon, J., Fluorescent and colorimetric sensors for detection of lead, cadmium, and mercury ions. *Chemical Society Reviews* **2012,** *41* (8), 3210-3244.

24. Hong, Y.; Lam, J. W.; Tang, B. Z., Aggregation-induced emission: phenomenon, mechanism and applications. *Chemical communications* **2009,** (29), 4332-53.

25. Bittermann, H.; Siegemund, D.; Malinovskii, V. L.; Häner, R., Dialkynylpyrenes: Strongly Fluorescent, Environment-Sensitive DNA

Building Blocks. *Journal of the American Chemical Society* **2008,** *130* (46), 15285-15287.

26. Uno, S.; Dohno, C.; Bittermann, H.; Malinovskii, V. L.; Haner, R.; Nakatani, K., A Light-Driven Supramolecular Optical Switch. *Angew Chem Int Edit* **2009,** *48* (40), 7362-7365.

27. Grell, M.; Bradley, D. D. C.; Long, X.; Chamberlain, T.; Inbasekaran, M.; Woo, E. P.; Soliman, M., Chain geometry, solution aggregation and enhanced dichroism in the liquid-crystalline conjugated polymer poly(9,9-dioctylfluorene). *Acta Polym* **1998,** *49* (8), 439-444.

28. Belletête, M.; Bouchard, J.; Leclerc, M.; Durocher, G., Photophysics and Solvent-Induced Aggregation of 2,7-Carbazole-Based Conjugated Polymers. *Macromolecules* **2005,** *38* (3), 880-887.

29. Fujimoto, K.; Shimizu, H.; Inouye, M., Unambiguous Detection of Target DNAs by Excimer−Monomer Switching Molecular Beacons. *The Journal of Organic Chemistry* **2004,** *69* (10), 3271-3275.

30. Conlon, P.; Yang, C. Y. J.; Wu, Y. R.; Chen, Y.; Martinez, K.; Kim, Y. M.; Stevens, N.; Marti, A. A.; Jockusch, S.; Turro, N. J.; Tan, W. H., Pyrene excimer signaling molecular beacons for probing nucleic acids. *Journal of the American Chemical Society* **2008,** *130* (1), 336-342.

31. Nakajima, A., Solvent Effect on the Vibrational Structures of the Fluorescence and Absorption Spectra of Pyrene. *Bulletin of the Chemical Society of Japan* **1971,** *44* (12), 3272-3277.

32. Kalyanasundaram, K.; Thomas, J. K., Environmental effects on vibronic band intensities in pyrene monomer fluorescence and their application in studies of micellar systems. *Journal of the American Chemical Society* **1977,** *99* (7), 2039-2044.

33. Glushko, V.; Thaler, M. S. R.; Karp, C. D., Pyrene fluorescence fine structure as a polarity probe of hydrophobic regions: Behavior in model solvents. *Archives of Biochemistry and Biophysics* **1981,** *210* (1), 33-42.

34. Langkilde, F. W.; Thulstrup, E. W.; Michl, J., The effect of solvent environment on molecular electronic transition moment directions:

Symmetry lowering in pyrene. *The Journal of Chemical Physics* **1983,** *78* (6), 3372-3381.

35. McDonald, J.; Echols, W.; Price, T.; Fox, R., Photophysical Processes in Polymers. VI. Spectroscopic Properties of 1-Vinylpyrene and Poly (1-Vinylpyrene). *The Journal of Chemical Physics* **2003,** *57* (4), 1746-1752.

36. Birks, J. B.; Christophorou, L. G., Excimer fluorescence spectra of pyrene derivatives. *Spectrochimica Acta* **1963,** *19* (2), 401-410.

37. Birks, J. B., Excimers. *Reports on Progress in Physics* **1975,** *38* (8), 903.

38. Winnik, F. M., Photophysics of preassociated pyrenes in aqueous polymer solutions and in other organized media. *Chemical Reviews* **1993,** *93* (2), 587-614.

39. Trkulja, I.; Biner, S. M.; Langenegger, S. M.; Haner, R., A molecular probe for the detection of homopurine sequences. *Chembiochem* **2007,** *8* (1), 25-27.

40. Seo, Y. J.; Hwang, G. T.; Kim, B. H., Quencher-free molecular beacon systems with two pyrene units in the stem region. *Tetrahedron Lett* **2006,** *47* (24), 4037-4039.

41. Wilson, J. N.; Teo, Y. N.; Kool, E. T., Efficient quenching of oligomeric fluorophores on a DNA backbone. *Journal of the American Chemical Society* **2007,** *129* (50), 15426-+.

42. Chu, N. Y. C.; Kawaoka, K.; Kearns, D. R., Investigation of Energy-Transfer Mechanisms in Pyrene Crystals. *The Journal of Chemical Physics* **1971,** *55* (7), 3059-3067.

43. Gilbert, A.; Baggott, J. E., *Essentials of molecular photochemistry*. CRC Press: **1991**.

44. Turro, N. J.; Ramamurthy, V.; Scaiano, J. C., *Modern molecular photochemistry of organic molecules*. University Science Books: **2010**.

45. Duhamel, J.; Winnik, M.; Baros, F.; André, J.; Martinho, J., Diffusion Effects on Pyrene Excimer Kinetics: Determination of the

Excimer Formation Rate Coefficient Time Dependence^ 1. *J. Phys. Chem.* **1992,** *96,* 9805-9805.

46. Duhamel, J.; Yekta, A.; Winnik, M. A., Excimer lifetime recovery: application to microheterogeneous systems. *The Journal of Physical Chemistry* **1993,** *97* (11), 2759-2763.

47. Birks, J.; Alwattar, A.; Lumb, M., Influence of environment on the radiative and radiationless transition rates of the pyrene excimer. *Chemical Physics Letters* **1971,** *11* (1), 89-92.

48. Mathew, A. K.; Siu, H.; Duhamel, J., A blob model to study chain folding by fluorescence. *Macromolecules* **1999,** *32* (21), 7100-7108.

49. Mathew, A. K.; Duhamel, J.; Gao, J., Maleic Anhydride Modified Oligo(isobutylene): Effect of Hydrogen Bonding on Its Associative Strength in Hexane Characterized by Fluorescence Spectroscopy. *Macromolecules* **2001,** *34* (5), 1454-1469.

50. Siu, H. C.-K. Characterization of the Self-Assembly of Pyrene-Labelled Macromolecules in Water. University of Waterloo, **2010**.

51. Valeur, B., *Molecular fluorescence: principles and applications*. Wiley-VCH: **2002**.

52. Marcus, R. A., On the Theory of Oxidation-Reduction Reactions Involving Electron Transfer. I. *The Journal of Chemical Physics* **1956,** *24* (5), 966-978.

53. Marcus, R. A., Electrostatic Free Energy and Other Properties of States Having Nonequilibrium Polarization. I. *The Journal of Chemical Physics* **1956,** *24* (5), 979-989.

54. Lakowicz, J. R., *Principles of Fluorescence Spectroscopy: CD-ROM*. Springer: **2006**.

55. Stryer, L.; Haugland, R. P., Energy transfer: a spectroscopic ruler. *Proceedings of the National Academy of Sciences of the United States of America* **1967,** *58* (2), 719.

56. Thomas, D. D.; Carlsen, W. F.; Stryer, L., Fluorescence energy transfer in the rapid-diffusion limit. *Proceedings of the National Academy of Sciences* **1978,** *75* (12), 5746-5750.

57. Katz, E.; Willner, I., Integrated nanoparticle–biomolecule hybrid systems: synthesis, properties, and applications. *Angewandte Chemie International Edition* **2004,** *43* (45), 6042-6108.

58. Nam, J.-M.; Stoeva, S. I.; Mirkin, C. A., Bio-bar-code-based DNA detection with PCR-like sensitivity. *Journal of the American Chemical Society* **2004,** *126* (19), 5932-5933.

59. Paciotti, G. F.; Myer, L.; Weinreich, D.; Goia, D.; Pavel, N.; McLaughlin, R. E.; Tamarkin, L., Colloidal gold: a novel nanoparticle vector for tumor directed drug delivery. *Drug delivery* **2004,** *11* (3), 169-183.

60. Eghtedari, M. A.; Copland, J. A.; Popov, V. L.; Kotov, N. A.; Motamedi, M.; Oraevsky, A. A. In *Bioconjugated gold nanoparticles as a contrast agent for detection of small tumors*, Biomedical Optics 2003, International Society for Optics and Photonics: **2003**; pp 76-85.

61. Chen, J.; Saeki, F.; Wiley, B. J.; Cang, H.; Cobb, M. J.; Li, Z.-Y.; Au, L.; Zhang, H.; Kimmey, M. B.; Li, X., Gold nanocages: bioconjugation and their potential use as optical imaging contrast agents. *Nano letters* **2005,** *5* (3), 473-477.

62. Kattumuri, V., *Gold nanoparticles for biomedical applications: synthesis, characterization, in vitro and in vivo studies*. ProQuest: **2006**.

63. Fukumori, Y.; Ichikawa, H., Nanoparticles for cancer therapy and diagnosis. *Advanced powder technology* **2006,** *17* (1), 1-28.

64. Maeda, H.; Seymour, L. W.; Miyamoto, Y., Conjugates of anticancer agents and polymers: advantages of macromolecular therapeutics in vivo. *Bioconjugate chemistry* **1992,** *3* (5), 351-362.

65. Qi, X.-R.; Maitani, Y.; Nagai, T.; Wei, S.-L., Comparative pharmacokinetics and antitumor efficacy of doxorubicin encapsulated in

soybean-derived sterols and poly (ethylene glycol) liposomes in mice. *International journal of pharmaceutics* **1997,** *146* (1), 31-39.

66. Paciotti, G. F.; Kingston, D. G. I.; Tamarkin, L., Colloidal gold nanoparticles: a novel nanoparticle platform for developing multifunctional tumor-targeted drug delivery vectors. *Drug Development Research* **2006,** *67* (1), 47-54.

Chapter 2

Instrumental Methods of Functional and Structural Characterization

2.1. Fluorescence

2.1.1. Theory

Photoluminescence includes fluorescence and phosphorescence. Electrons of molecules can exist in a number of vibrational energy levels of ground state (S_0) or the singlet state (S_1, S_2 and S_n). These electrons can be excited to a higher energy level such as S_1, S_2, or S_n, upon the absorption (~10^{-15} s) of an incident beam of a specific wavelength, λ_1. This 'excited state' electron decays back to the lower energy 'ground-state' through radiative and non-radiative pathways. This process can be illustrated by an electronic level of Jablonski diagram (Fig. 2.1.1). Upon excitation, the electrons of a molecule within a given electronic state (S_n), relax rapidly, within 10^{-14} to 10^{-12} s, to the lowest vibrational level of the excited electronic state (S_1). Such non-radiative process is called "vibrational relaxation." Another type of a non-radiative process is "internal conversion", where electrons are excited to energy states higher than S_1 followed by a rapid non-radiative decay process to the lowest energy singlet excited state (S_1) with a time

scale of 10^{-12} s. Such relaxation happens in the singlet state in which the spin of the excited electron is paired with the ground state electron. A radiative emission takes place from the lowest excited singlet states to the ground state within several orders of nanoseconds and is known as *fluorescence*. Because of the aforementioned non-radiative pathways, the radiation of a longer wavelength, λ_2 than λ_1 can be emitted as an electron decays to its ground-state. This phenomenon was first observed by Stokes in 1852 and named as a Stokes shift.[1-2] Non-radiative relaxation can also occur between excited states of different spin multiplicity, known as "intersystem crossing". It is known that intersystem crossing occurs in the presence of heavy-atom molecules probably and resulted in transition to the triplet state (T_1) due to "spin-orbit coupling".[2] The T_1 possesses a

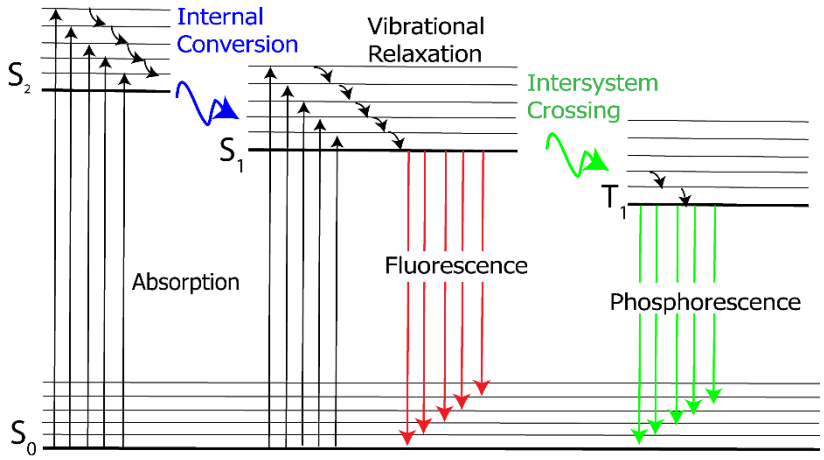

Fig.2.1.1. Jablonski diagram

“forbidden" spin transition in which the excited electron is no longer paired with the ground state electron. However, this is a rare event in electronic decay since a transition from S_1 to T_1 is usually forbidden and occurs slower (~10^{-8} s) than internal conversions. If photons are emitted from this triplet state to ground state, the process is termed as phosphorescence. Phosphorescence emission rate is very slow and lifetime is usually in the range of milliseconds to seconds.

2.1.2. Instrumentation

Fluorescence measurements can be classified into two types of measurements, steady state and time-resolved. Steady-state measurements are performed with a continuous illumination and detection with photon. The schematic of a steady state fluorescence spectroscopy is illustrated in Scheme 2.1.[1] The light source is usually Xenon arc lamp capable of supplying wide range of UV wavelengths from 250 nm to near-infrared wavelengths of 800 nm. Both excitation and emission wavelength were selected with a monochromator containing a diffraction grating. Then, photomultiplier tube in the detector converts the intensity of the fluorescence signal into a corresponding electrical current and eventually data file. The emission spectra are acquired as a function of emission wavelength at a fixed excitation wavelength, while the excitation spectra are collected in an inverse manner. It is assumed that the steady state reaches immediately reached after exposure by the continuous beam of the Xenon lamp. The steady-state fluorescence provides the information of averaged

time-resolved spectra which provide the insight to the local environment of molecules.

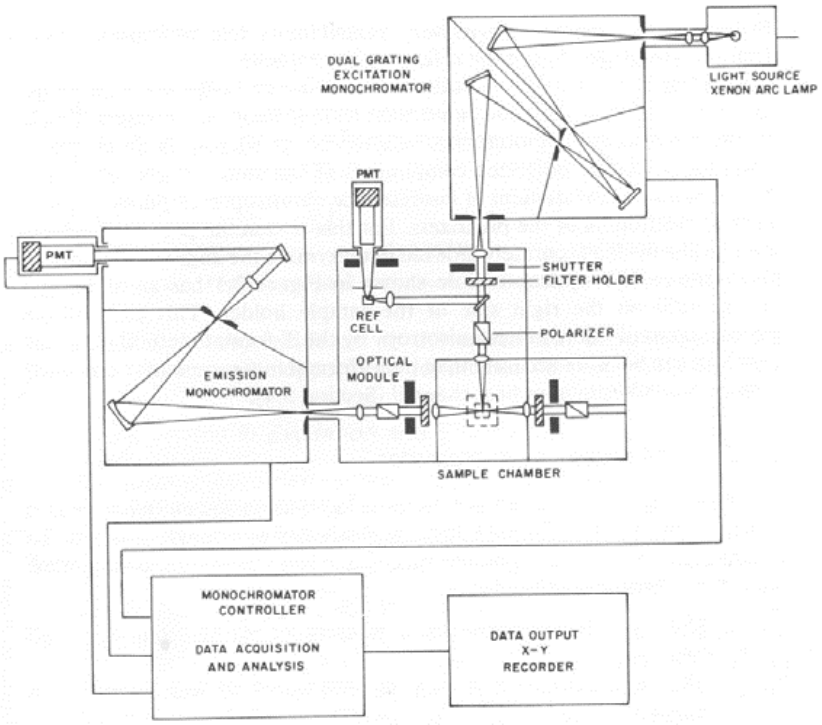

Scheme 2.1. Schematic of Steady-State fluorescence spectroscopy

Time-Resolved fluorescence measurements use a single photon counting technique. The light source of the single photon counter emits nanosecond pulses at a certain wavelength and frequency, where the pulse width is typically shorter than the decay time. After a short pulse of light excites the sample repetitively, the subsequent emission is recorded by a detector. A constant fraction discriminator (CFD) responds to only the first photon detected— independent of its amplitude—from the detector.[1] This first photon from sample emission is the stop signal for the Time-to-Amplitude

Converter (TAC). The excitation pulses trigger the initial signals. The Multi-Channel Analyzer (MCA) records repetitive start-stop signals of the single-photon events from the TAC, to generate a histogram of photon counts as a function of time channel units. The lifetime can be extracted from this histogram. This experiment provides more information about molecules to determine the environment that the sample molecules inhabit and intrinsic characters of size and shape of molecules, and the distances between different parts of the molecules.

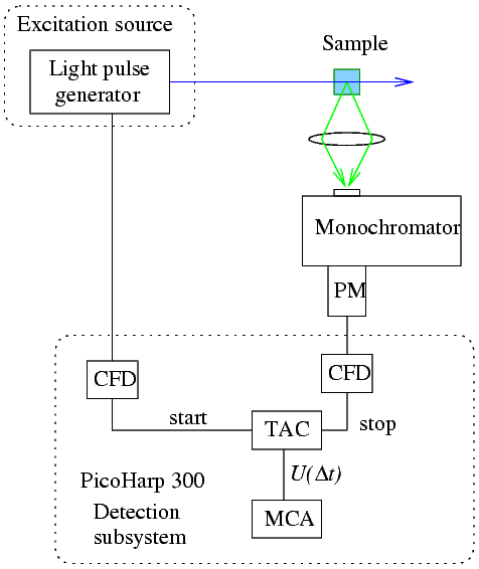

Scheme 2.2. Schematic of Time-resolved fluorescence spectroscopy

2.2. Scattering

Scattering is a general physical process where some forms of radiation, such as light, sound, or moving particles, are forced to deviate from a straight trajectory.[3] The energy sources can be light, X-ray or neutrons. The

different sources interact with matter in a different way. X-ray, being an electromagnetic radiation, interacts with the electron cloud of the atoms. Hence, X-ray scattering amplitude for an atom is proportional to electron density of the atoms. Neutrons interact with the nuclei of the atoms and the scattering amplitude is related to neutron scattering length which does not follow obvious trend in the period table, thus having the advantage in varying contrast through the replacement by isotopes without significantly changing the chemical properties. For example, the neutron scattering lengths for hydrogen and deuterium are widely different (scattering lengths of hydrogen and deuterium are b_H = -2.739 x 10^{-13} cm b_D = 6.671 x 10^{-13} cm, respectively). Moreover, unlike X-ray, neutron can penetrate through most of the materials (even heavy metals), greatly simplifying the design of sample environments such as high temperature, high pressure, rheometer etc. To understand wave properties in detail, it is desired to understand the de Broglie equation which defines the relationship between wavelength, λ, and particular properties associated with a particle such as its mass, m, and velocity, υ, along with Planck's constant, h.

$$\lambda = h / m\upsilon \qquad (2.2.1)$$

The wave can interact with matter in two ways – i.e. constructive and destructive. For constructive interference to occur, i.e. a finite amplitude of the recombined wave fronts – it is necessary to satisfy Bragg's law for the diffraction as shown in Fig. 2.2.1.

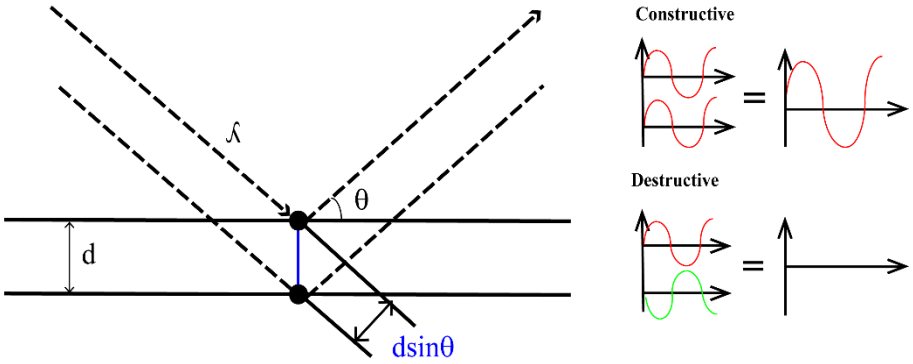

Fig.2.2.1. Bragg's law

$$n\lambda = 2d\sin(\theta), \text{ where n is any integer} \qquad (2.2.2)$$

Fig. 2.2.2 shows a general scattering schematic with an incident beam with wavelength λ illuminating a sample. As the incident beam interacts with the sample, the scattered beam radiates with the same wavelength as the incident beam. The difference in optical paths between the light scattered by different parts of sample makes the scattered beam incoherent and out of phase.[4] The unit vector of the incident and scattered beam can be described by the incident wave vector and scattered vector, $\overrightarrow{u_i}$ and $\overrightarrow{u_s}$ respectively. Then, determination of the phase difference, δ, between two scattered points in a sample with the distance of $\overrightarrow{R_j}$ can be achieved by Eqn 2.2.2. For scattering angle θ, the scattering vector is defined by Eqn. 2.2.4.

$$\delta = \overline{AC} - \overline{OB} = (\overrightarrow{u_i} - \overrightarrow{u_s}) \cdot \overrightarrow{R_j} \qquad (2.2.3)$$

$$\overrightarrow{q_i} \equiv \frac{2\pi n}{\lambda}\overrightarrow{u_i}\,, \quad \overrightarrow{q_s} \equiv \frac{2\pi n}{\lambda}\overrightarrow{u_s} \tag{2.2.4}$$

$$\vec{q} = \overrightarrow{q_i} - \overrightarrow{q_s} = |\vec{q}| = 2\,|\vec{q}_i| \sin\frac{\theta}{2} = \frac{4\pi n}{\lambda}\sin\frac{\theta}{2} \tag{2.2.5}$$

, where λ is the wavelength of the incident beam and q is the scattering vector. Then, the real (d) and reciprocal (q) spaces can be related as Eqn. 2.2.6.[5]

$$d = \frac{2\pi}{q} \tag{2.2.6.}$$

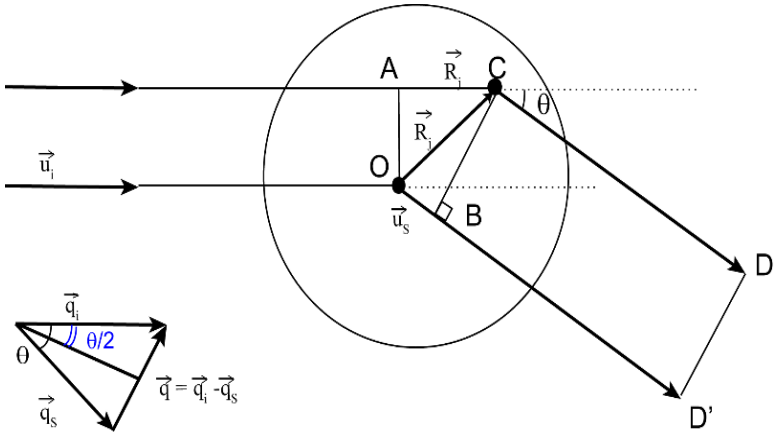

Fig.2.2.2. Determination of the phase difference between two parts of a sample.

The scattering amplitude, F(q) can therefore be derived from the Fourier transform of the density distribution function, $\rho(\vec{r})$ of the system of interest as follows.

$$F(\vec{q}) = \mathcal{F}[\rho(\vec{r})] = \int_V \rho(\vec{r}) e^{-iq\cdot\vec{r}} d\,r \qquad (2.2.7)$$

where $\mathcal{F}$ denotes the Fourier transform operator and $\rho(\vec{r})$ is the scattering length density. The experimentally measured scattered intensity $I(\vec{q})$ is proportional to the product of the amplitude and its complex conjugate $F(\vec{q})^*$.

$$I(\vec{q}) \propto F(\vec{q}) \cdot F(\vec{q})^* = |F(\vec{q})|^2 \qquad (2.2.8)$$

More precisely, the scattered intensity measured in the number of photons scattered into the volume element $d\Omega$ per second relative to the incoming flux.

$$I(\vec{q}) = r_e^2 \cdot |F(\vec{q})|^2 \Delta\Omega \frac{I_0}{A_0} \qquad (2.2.9)$$

where I_0 [number of photons/s] is the intensity of the incident beam, A_0 is its cross-sectional area and $r_e = e^2/(4\pi\varepsilon_0 mc^2) = 2.82 \times 10^{-15}$ m is the *Thomson scattering length* of electron. The inverse operation is called inverse Fourier transform and it gives the electron density distribution:

$$\mathcal{F}^{-1}[F(q)] = \frac{1}{2\pi} \rho(r) \qquad (2.2.10)$$

Since I(q) is not a measurable quantity, the inverse Fourier transform of I(q) can be derived :

$$\mathcal{F}^{-1}\lceil |F(q)|^2 \rceil = \mathcal{F}^{-1}\lceil F(q) \cdot F(q)^* \rceil = \frac{1}{4\pi} \rho(r) \otimes \rho(-r) \qquad (2.2.11)$$

where $\otimes$ denotes the convolution operator. This equation is defined as an *autocorrelation function of the density* or the *Patterson function*:

$$P(r) = \rho(r) \otimes \rho(-r) = \int_V \rho(R)\rho\,(R + r)dr \qquad (2.2.12)$$

The Patterson function provides the length scale over which the density distribution varies, weighted in accordance to their frequency of occurrence. It gives the position of each particle relative to the others, indicating the weight of a particular inter-particle distance. The overall sheme of scattering is shown in Fig. 2.2.2.[5-6]

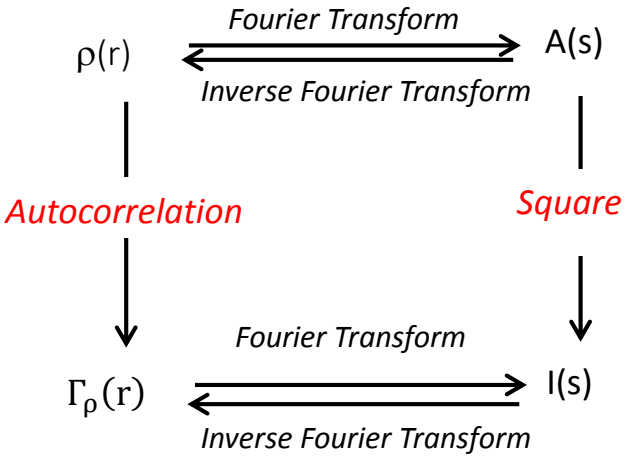

Fig.2.2.3. General Scheme of Scattering

It should be noted that the scattering pattern of objects depends on a three-dimensional structure of the scattering objects and the correlated distances between them. As a result, different scattering patterns represents different morphology of particles, termed as Form Factor, P(q).

$$
\begin{aligned}
I(q) &= A(q) \cdot A^{*}(q) \\
&= \left(\rho_p - \rho_o\right)^2 \left[\int_V f(r)\, e^{-iq\cdot r} dr\right]^2 \\
&= \Delta\rho^2 V^2\, P(q)
\end{aligned}
\qquad (2.2.13)
$$

2.2.1. Small Angle Scattering

Small-angle X-ray/Neutron scattering (SAXS/SANS) is a suitable tool to study structures and interactions of species. Based on the inverse relationship between d-spacing and $\vec{q}$, larger structures give rise to scattering events at smaller angles. In specific, Small Angle X-ray Scattering (SAXS) can be utilized to study samples in the range of 1 to 100 nm. The scattering is statistically averaged information from the specimen. Further, scattering data in Fourier (also called reciprocal) space can be either converted to extract real space information or be fitted to models describing structures in the reciprocal space. At very low angles ($q \cdot R_g << 1$) the scattering pattern can be described with the Guinier region, which corresponds to the molecular mass and the size of the particle (radius of gyration, R_g). Equation 2.2.14 indicates the Guinier Equation, where I(0) is the intensity at zero angle and proportional to the total molecular mass in the beam. The radius of gyration (R_g) is the square root of the average squared distance from the center of mass of the particle weighted by the scattering length density.

$$
I(q) = I(0) \exp\left[-\left(\frac{{R_g}^2}{3}\right)\right] \qquad (2.2.14)
$$

2.3. Transmission electron microscope (TEM)

Electron microscopy is a complementary method to the scattering to probe length scales of molecules. Nevertheless, microscopy gives only the local information of the matter. It provides information of matter in real space compared to scattering methods which measure in the reciprocal space.

Transmission electron microscope (TEM) is a method that allows visualization of structure and analysis of specimens within the micro (μm)-nano range (nm). This method applies a focused beam of high energy electrons ($\lambda << 1$) instead of photons. The λ can be varied by the energy of the electron beam based on the de Broglie's Equation as shown in Eqn. 2.2.1. When a high-energy electron beam hits a specimen, a variety of signals can be generated as shown in Fig. 2.2.1.

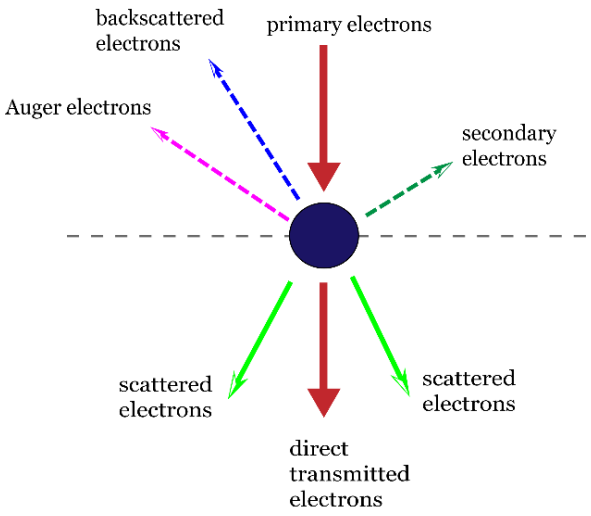

Fig.2.3.1. Interactions between beam and specimen

$$\lambda_{>100kV} = \frac{h}{\sqrt{2m_0eV\left(1+\frac{eV}{m_0c^2}\right)}}, \quad \lambda_{<100kV} \approx \frac{h}{\sqrt{2m_0eV}} \qquad (2.3.1)$$

$$, where\ m_0 : electron\ mass, h: Plank\ constant, c: speed\ of\ light$$

After illuminating a sample with this accelerated electron beam generated by an electric gun at high voltage transmitted in a high vacuum, the electrons that pass through the sample are collected onto a fluorescent screen or through a camera. Optically, the column consists of a condenser, objective, intermediate and projector lens. The condensers lenses are for controlling the geometry of electron beam size on the specimen. The objective lens forms the image or diffraction patterns through bright field and dark field. A specimen is inserted in the magnetic field of the objective lens. The intermediate and projector lenses are used to magnify the image of the objective lens.[7] In general, there are three common uses of TEM: imaging, diffraction and spectroscopy. The resolution (δ_d) and depth of field (d_{obj}) of TEM are defined with the Raleigh equation (Eqn 2.3.2), where λ is wavelength of beam, α is aperture semi-angle. Due to the high energy electrons (λ<<1), the resolution of x,y and z-direction in the sample can be reached to the atomic scale which allows the versatility of the specimens from metallic to biological (amorphous) materials.[8-11]

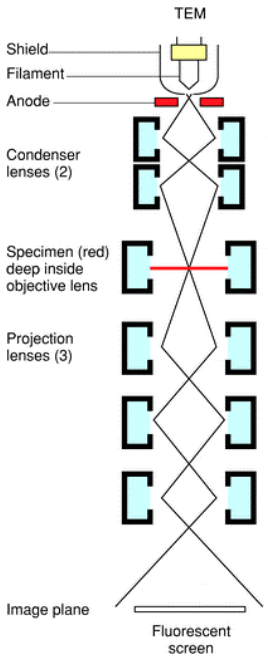

Scheme.2.3. Scheme of TEM

$$\delta_d \approx \frac{0.61\,\lambda}{\alpha}, \quad d_{obj} = \frac{\delta_d}{\alpha} = \frac{0.61\,\lambda}{\alpha^2} \tag{2.3.2}$$

Image contrast of TEM is attributed to different interactions between incident beam and specimen including diffraction, mass-thickness and phase contrast. In the bright field in imaging, the images will be dark where electrons do not penetrate through. Therefore, thicker parts within the specimen will deplete the transmitted beam more resulting in a dark spot in the image. Also, the dark field using a diffraction is used to determine the crystal structure, symmetry, and orientation of materials. If heavy atoms are present in the specimen, then it absorbs and scatters more electrons versus lighter atoms. Phase contrast involves an interference of the beam resulting in the formation of lattice fringes in the image and is related to the structural

periodicity of the sample. Overall, to get a suitable intensity of transmitted electrons, the sample thickness should be on the order of 10 nm to 100 nm. By applying spectroscopic techniques, microanalysis is possible (i.e., chemical composition and some bonding differences).[7, 12] Nevertheless, if the specimens do not have enough contrast, then it may need other pretreatment processes such as negatively staining or cryo-fixation for biological samples.

2.4. Reference

1. Lakowicz, J. R., *Principles of Fluorescence Spectroscopy: CD-ROM*. Springer: **2006**.
2. Valeur, B., *Molecular fluorescence: principles and applications*. Wiley-VCH: **2002**.
3. Bohren, C. F.; Huffman, D. R., *Absorption and scattering of light by small particles*. John Wiley & Sons: **2008**.
4. Rubinstein, M.; Colby, R. H., *Polymer physics*. OUP Oxford: **2003**.
5. Higgins, J. S.; Benoît, H., *Polymers and neutron scattering*. Clarendon Press Oxford: **1994**.
6. Roe, R.-J.; Roe, R., *Methods of X-ray and neutron scattering in polymer science*. Oxford University Press New York: **2000**; Vol. 739.
7. Brandon, D.; Kaplan, W. D., *Microstructural characterization of materials*. John Wiley & Sons: **2008**.
8. Wang, C.-M.; Li, X.; Wang, Z.; Xu, W.; Liu, J.; Gao, F.; Kovarik, L.; Zhang, J.-G.; Howe, J.; Burton, D. J.; Liu, Z.; Xiao, X.; Thevuthasan, S.; Baer, D. R., In Situ TEM Investigation of Congruent Phase Transition and Structural Evolution of Nanostructured Silicon/Carbon Anode for Lithium Ion Batteries. *Nano Letters* **2012,** *12* (3), 1624-1632.

9. Wang, S.; Lu, Z.; Wang, D.; Li, C.; Chen, C.; Yin, Y., Porous monodisperse V2O5 microspheres as cathode materials for lithium-ion batteries. *Journal of Materials Chemistry* **2011,** *21* (17), 6365-6369.
10. Waninge, R.; Kalda, E.; Paulsson, M.; Nylander, T.; Bergenstahl, B., Cryo-TEM of isolated milk fat globule membrane structures in cream. *Physical Chemistry Chemical Physics* **2004,** *6* (7), 1518-1523.
11. Goldberger, J.; He, R.; Zhang, Y.; Lee, S.; Yan, H.; Choi, H.-J.; Yang, P., Single-crystal gallium nitride nanotubes. *Nature* **2003,** *422* (6932), 599-602.
12. Muller, D. A., Structure and bonding at the atomic scale by scanning transmission electron microscopy. *Nature materials* **2009,** *8* (4), 263-270.

Chapter 3

Controllable Formation of Pyrene ($C_{16}H_{10}$) Excimers in Polystyrene/ $TBAPF_6$ Films through Solvent Vapor and Temperature Annealing

3.1. Introduction

Fluorescence molecules have been ubiquitously applied as sensing materials for explosives [1-2], optical switch [3-4], biological probes for DNA or RNA [5-7], polarized light emitters [8-15], monitors for micelles formations [16-19] and other aspects [20-26]. One of the most common fluorophores is pyrene (Py), which has two ranges of fluorescence emissions: 370 ~ 400 nm (monomer emission, I_{mon}) and 420 ~ 600 nm (excimer emission, I_{exc}) depending on their intermolecular distance (d) between the Py molecules, from which the terms of monomer ($d > 1$ nm) and excimer (0.4 nm $< d < 1$ nm) are defined.[27-28] Excimer is a homopolar excited dimeric complex, due to the interaction between its first excited singlet state and unexcited molecules of the same species.[29] The formation of Py excimers depends on the orientation and proximity between two molecules, resulting in different spectra in the ground and excited states.[6, 30-32] In solution state, the formation of Py excimers is governed by a diffusion controlled process.[27, 29-30] As a result, a

high concentration of Py promotes the formation of Py excimers prior to the self-quenching.[33] Nevertheless, the formation of Py excimers in the solid state may be induced by a different mechanism due to a reasonably low diffusivity [34-36] and is not yet well understood. Unlike the other polyaromatic hydrocarbon (PAH) fluorophores, Py shows a relatively longer singlet lifetime (~ 450 ns), resulting in the enhanced excimer fluorescence.[30]

In regard to the fluorescence spectrum of Py monomer, five emission peaks from 370 to 400 nm are normally observed [37] and the solvent polarity around Py can be determined from the ratio of I_1/I_3 (I_1 ~ 373 nm, I_3 ~ 384 nm) [37-39] – the higher the I_1/I_3 value, the more polar solvent environment. It is generally believed that the solvent dependence of the Py is attributed to the symmetry distortion of the Py structure induced by dispersion or van der Waals forces [40]. As a result, the solvent environment significantly affects the Py monomer fluorescence spectrum. However it is not clear whether the molecular environment around Py also has a strong influence over the excimer fluorescence or not.

Recently, Wang et al. [2] have reported intriguing results that the electrospun films composed of pyrene (Py)/ polystyrene (PS)/ tetrabutylammonium hexafluorophosphate ($TBAPF_6$) are capable of detecting nitro-aromatic, nitroamine and nitroether explosives, e.g., TNT (Trinitrotoluene), Tetryl (2,4,6-Trinitrophenylmethylnitramine), RDX (hexahydro-1,3,5-trinitro-1,3,5triazine), PETN (pentaerythritol tetranitrate)

and HMX (tetrahexamine tetranitramine) at a vapor pressure as low as 10 ppb, 74 ppt, 5 ppt, 7 ppt and 0.1 ppt, respectively, generated from 1 ng explosive solid residues via the fluorescence quenching technique. It is also found that the electrospun Py/PS/$TBAPF_6$ film illustrates the highest normalized I_{exc}/I_{mon} value compared to those prepared by other methods, e.g., dip-coating, spray coating, spin-casting.[2] Moreover, the fluorescence of electrospun films quenches the fastest among those made by the aforementioned methods in the presence of explosive molecules, presumably due to the fast diffusion in the high-porosity nano-fibrous structure. Since the maximum I_{exc} is in the range of 440 ~ 490 nm (blue color), the detection of explosive materials can be performed by naked-eyes with a portable UV lamp, greatly facilitating the operation for detection. Therefore, the attempt to increase I_{exc} becomes an important task in order to yield higher sensitivity for the sensors based on the technique. However, this requires a fundamental understanding of the formation of Py excimers in solid films. The front most question to be answered is "what are the key factors that affect the excimer fluorescence most?" A systematic study on three parameters – temperature, evaporation rate and solvent vapor pressure – that exhibit great potential to influence the formation of Py excimers in the solid thin films is presented here. Since these parameters are often inter-dependent, the experimental approach is carefully designed to differentiate the effect of each parameter on the excimer fluorescence under a various film processing methods. It is found that the I_{exc} of the Py/PS/$TBAPF_6$ thin

films can be significantly enhanced under high vapor pressure annealing even for the post-produced films.

3.2. Experimental

Materials and Characterization

All the chemical components of $TBAPF_6$, PS (M_W = 350,000g/mol and Mn = 170,000g/mol), Py and the solvent, tetrahydrofuran (THF, > 99.9%) are all from Sigma Aldrich and used as purchased.

In order to compare the fluorescence of the films produced by different procedures, all the samples were prepared at the same composition of $TBAPF_6$/PS/Py (45.4: 36.3: 18.3 by weight), which was chosen to yield uniform nanoscale fibrous structure through the electrospinning process [2]. The solute mixture is then dissolved in THF to yield a solution with a total concentration of 0.1102 g/mL.

Scheme 3.1 shows a schematic of various preparation procedures applied in this study:

(1) Electrospinning: An electric field of a voltage of 25 kV was employed in the electrospinning instrument, CZE-1000R (Spellman High Voltage Electronics Co., NY, USA). The feeding rate of the Py/PS/$TBAPF_6$ THF solution was set to be 0.3 mL/hr through a syringe pump (KD-200, KD Scientific Inc., Holliston, MA, USA) under ambient conditions with a distance of 10cm.

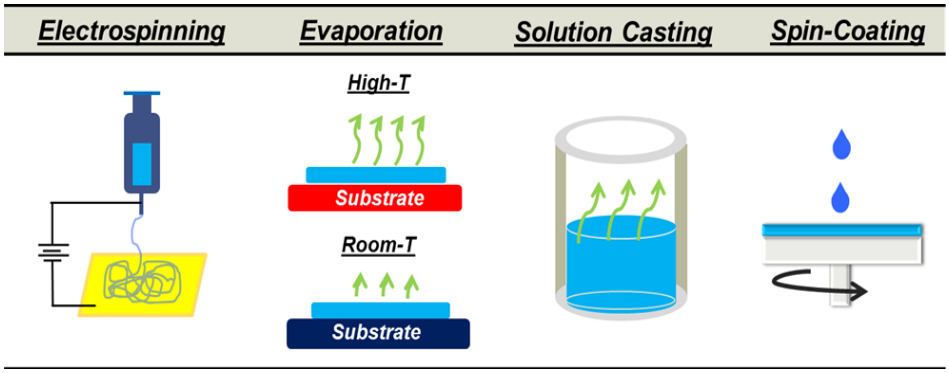

Scheme 3.1. A variety of methods used in this study to produce the films made from the same THF solution of Py/PS/TBAPF$_6$, including electrospinning, high-T (or low-T) evaporation, spin-coating and solution casting.

(2)Spin Coating: the same solution was used to produce the polymer films on a glass slide by a spin coater (Laurell Technologies WS-400E-6NPP-LITE) with a spin rate of 1,000 rpm.

(3) High-*T*/Room-*T* Evaporations: The polymer films are made by solvent evaporation. The glass substrates were first preheated to the desired temperature (high *T* or room *T*) and equilibrate for ~ 1 hour. Then, a 100 μL of the solution was placed on the pre-heated substrate and spread by a sharp edge scraper, forming a film of an even thickness. To prevent overheating and ensure sufficient dryness of the film, different periods of time are required at various temperatures generally within 10 minutes.

(4) Solution Casting: The drying mechanism is similar to the room-*T* evaporation film, except for a greater thickness. The solution of Py/PS/TBAPF$_6$ was placed in a vial and left in a fume hood till the solvent

evaporates for 24 hours. After eliminating major amount of THF, the vial was then placed under vacuum for 24 hours. The main difference between solution-casting and room-*T* evaporation is the thickness – solution-casting always yields thicker films.

Characterization

The Py/PS/TBAPF$_6$ films are studied by the following techniques to reveal their fluorescence response, structures and solvent residue.

(1) Fluorescence: The fluorescence of the prepared films was measured by a steady-state fluorescence spectroflourometer (Flourolog, Jobin Yvon Horiba). The films were excited at a wavelength of 350 nm. The emission spectra were monitored in the range of 360 – 600 nm through a 1-mm slit and normalized by the maximum intensity of the corresponding spectrum.

(2) X-Ray Diffraction (XRD): The XRD pattern of the film was obtained through a regular θ-2θ conFig.uration by a Bruker D8 Advance X-Ray Diffractometer with a 2.2 kW Cu-anode sealed tube. The XRD data were analyzed after background subtraction and expressed in an arbitrary unit.

(3) ^{1}H-Nuclear Magnetic Resonance (NMR): ^{1}H-NMR spectra were used for the determination of residual solvent (THF) by the resonance frequency of 500 MHz for ^{1}H (Bruker DMX-500 high resolution digital NMR spectrometer). Chemical shifts were calibrated with respect to that of the internal sample of tetramethylsilane (TMS) and deuterated cholorform ($CDCl_3$) was used as a solvent.

(4) SEM (Scanning Electron Microscopy): The morphology of films was measured by the JEOL 6335F Field Emission SEM (SM-6335F), a cold cathode field emission scanning electron microscope, which provides a resolution of 1.5nm at 15kV and 5.0nm at 1kV.

3.3. Results and Discussion

As mentioned previously, drastic differences in Py excimer fluorescence of the Py/PS/$TBAPF_6$ films are found when the films undergoes different preparation procedures as shown in Fig. 3.1. It has shown that electrospun film results has a high I_{exc}/I_{mon} ratio (= 1.22 in Table 3.1) in comparison of those from other procedures, e.g., spin-coating, solution casting, room-*T* evaporation. In order to understand the formation of Py excimers in the polymer films, our first attempt is to investigate the correlation between the nanostructure of films and their fluorescence under different procedures. It is known that Py forms a crystalline structure, whose lattice parameters and orientation can be characterized by XRD. Fig. 3.2 contains the XRD patterns of electrospun and solution casting films. The fact that $TBAPF_6$ salt also forms crystal in the polymer films (inset of Fig. 3 2) yields complicated XRD patterns containing features from both Py and $TBAPF_6$.

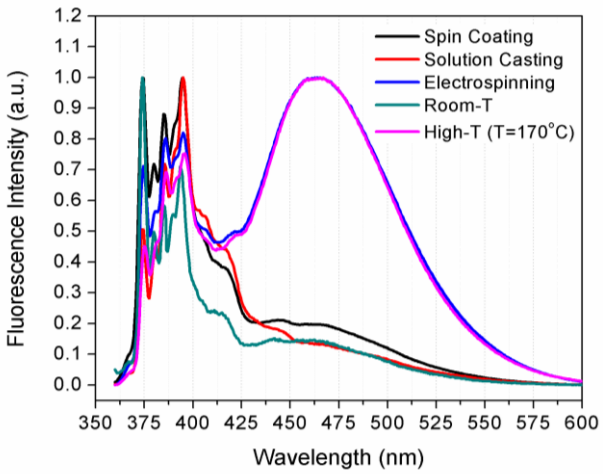

Fig. 3.1. Fluorescence emission spectra (excitation wavelength of 350 nm) prepared by various methods (i.e., spin coating, solution casting, electrospinning, and high-*T*/room-*T* evaporation, respectively). Except for electrospun and high-*T* films, the rest samples indicate low I_{exc}.

Nevertheless, the Bragg peaks of the electrospun film are highly smeared, suggesting smaller sizes of crystals. Electrospinning process commonly yields a nano-fibrous structure with a rapid solvent evaporation rate, strong electric field and shear stress, rendering non-equilibrium, stretching state of polymers.[41-43] Inspired by the XRD result, we attempted to reduce the size of Py crystals by rapid solvent evaporation at 170 ^{o}C for 2 mins, which is higher than the boiling temperature, T_b of THF (66^{o}C), glass transition temperature, T_g of PS (100 ~ 110 ^{o}C) and Py melting transition temperature, T_m (148 ^{o}C). The resultant sharp Bragg peaks (Fig. 3.2) as those observed in the solution casting film indicate that our approach to reduce the Py crystal size is not efficient; however, unexpectedly, the I_{exc}/I_{mon} of high-*T* evaporation film (= 1.33 in Table 3.1) exhibits a comparable, if not higher,

value than that of the electrospun film (=1.22). Nevertheless, there is no similarity in the XRD patterns between the two, thus implying weak correlation between crystal size (or orientation) and excimer fluorescence.

Table 3.1. The fluorescence intensity ratio of I_{exc} (at 466 ± 1 nm)/I_{mon} (at ~ 395nm) peaks and ratio of I_1/I_3 (at I_1 ~ 373nm, I_3 ~ 384nm) of different films (made by electrospinning, room-*T* and high-*T* evaporation, and spin coating).

	I_{exc}/I_{mon}	I_1/I_3
Electrospinning	1.220	0.887
Room-T Evaporation	0.203	1.712
High-T Evaporation	1.329	0.652
Spin Coating	0.197	1.136
Solution Casting	0.133	0.703

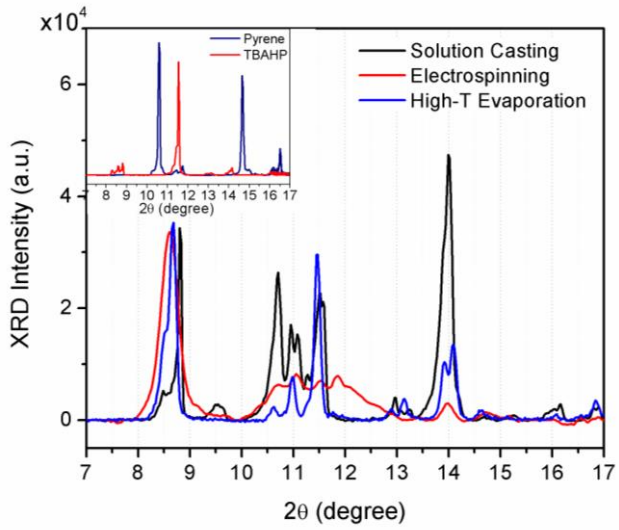

Fig. 3.2. The XRD spectra of Py/PS/TBAPF$_6$ made by different methods (solution casting, electrospun and high-*T* films) after background subtraction. The inset is the XRD patterns from Py (blue) and TBAPF$_6$ (red).

SEM images were also taken to investigate the effects of nanoscaled morphology on the I_{exc}. While the high-T and electrospun films show similar high I_{exc}/I_{mon} values (Table 3.1), they exhibit drastically different morphologies as shown in Fig.ure 3.3, where the electrospun film is composed of nanofibers and the high-T film contains micrometer-size pores populated on the surface. The porosity of the electrospun film is apparently higher than that of the high-T one. It is evident that the comparable I_{exc} of

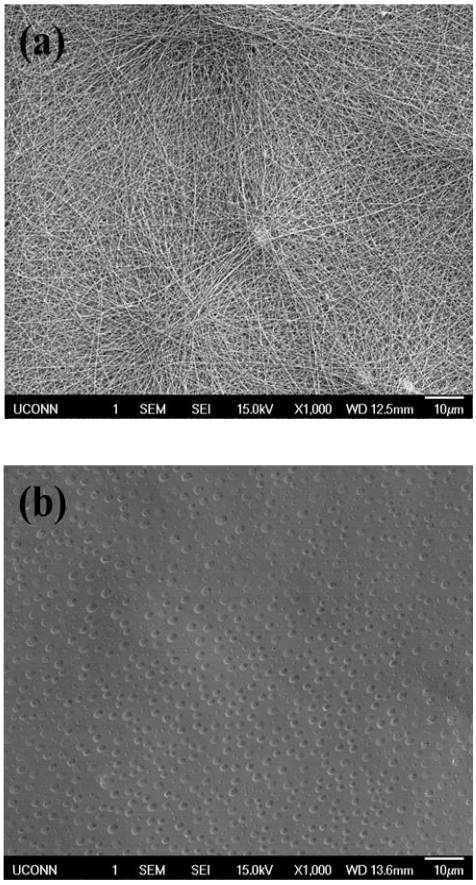

Fig. 3.3. The SEM images of (a) Electrospun (b) High-*T* evaporation Py/PS/TBAPF$_6$ films

the two films (electrospun and high-T evaporation) is not originated from the morphology (i.e., structure and porosity). However, the faster quenching rate observed in the electrospun film by 2,4-DNT as shown in Fig. 3.S1 indicates that morphology may play an important role in the quenching efficiency. Investigation of the quenching mechanism is beyond the scope of the current study, since this report mainly focuses on determining the key parameters which control I_{exc}. It is known that the molecular environment of fluorophores can also affect their monomer fluorescence. For example, the higher I_1/I_3 value represents Py being in a more polar environment. However, to the best of our knowledge, the correlation between the formation of Py excimers and I_1/I_3 has not been studied. Table 3.1 illustrates the I_1/I_3 and I_{exc}/I_{mon} of the films prepared by different procedures. High I_{exc}/I_{mon} samples (1.22 and 1.33 for electrospun and high-*T* films, respectively) have lower I_1/I_3 values (0.89 and 0.65, respectively), but the inverse may not stand true (e.g., I_1/I_3 = 0.70 and I_{exc}/I_{mon} =0.13 for the solution casting film). This statement seems valid in the later study. Therefore, we can presume that the formation of the Py excimers is preferable at the condition of less polar environment around the Py molecules.

3.3.1 Evaporation Rate and Temperature Effect

The fact that a higher I_{exc}/I_{mon} is observed in the case of high-*T* evaporation film indicates that electric field and shear stress may not be the determining factors for the formation of Py excimers. A significant difference is found between the I_{exc}/I_{mon} of the high-*T* and room-*T* evaporation films (Table 3.1), suggesting that other possible factors may dictate the excimer fluorescence. To confirm the observed temperature dependence, the Py fluorescence emission spectra are measured as a function of *T* as shown in Fig. 3.4(a), where I_{exc}/I_{mon} increases with increased *T* at the sample stage [Fig. 3.4(b)] while the values of I_1/I_3 are practically invariant (i.e., temperature-independent) around 0.55 ± 0.10, consistent with the above-mentioned values. In spite of an evident temperature dependence of the I_{exc}/I_{mon}, it should be noted that temperature may affect many other underlying properties of the solvent, e.g., evaporation rate and solvent vapor pressure. We will discuss over each possible factors in the following section.

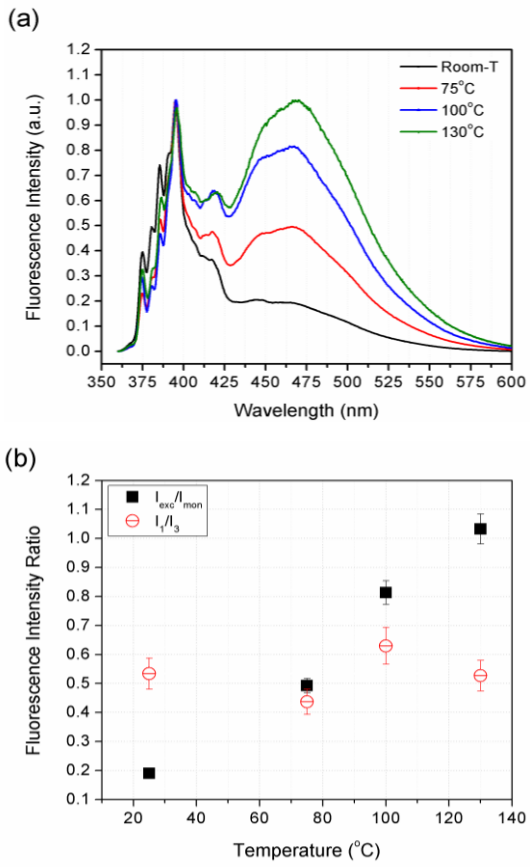

Fig. 3.4 (a) Fluorescence emission spectra of Py/PS/$TBAPF_6$ films at different temperature (room-*T*, 75°C, 100°C, 130°C, respectively), where I_{exc} increases with increased *T*. (b) The I_{exc}/I_{mon} (solid squares) and I_1/I_3 (open circles) as a function of temperature. The I_{exc}/I_{mon} increases with increased T with nearly invariant I_1/I_3 values.

Evaporation Rate: One of the parameters initially considered as a possible important parameter is the evaporation rate, which is dictated by several factors such as concentrations, inter-molecular interactions, temperature and external pressure[41]. The fact that the fast-evaporation spin coating process yields a low I_{exc}/I_{mon} value implies that evaporation rate may not be a crucial factor. In order to provide further understanding, the fluorescence of a polymer film prepared at room temperature yet under vacuum to

maximize the solvent evaporation rate is examined. Fig. 3.5 shows a comparison of fluorescence from the films prepared at room temperature under regular evaporation and vacuum, respectively. Both illustrate low I_{exc}/I_{mon} values and the difference is marginal, confirming the evaporation rate *does not* play an important role in the formation of excimers.

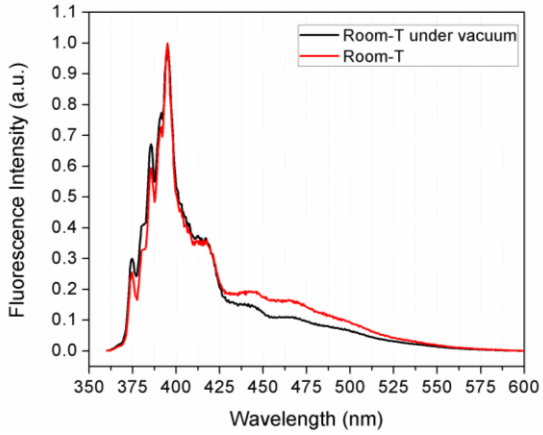

Fig. 3.5 The fluorescence emission spectra of two room-*T* Py/PS/$TBAPF_6$ films which are prepared under atmosphere pressure and vacuum (overnight), respectively.

Temperature: Other than the fast evaporation rate, the high temperature seemingly suggests that the enhanced fluorescence of Py excimers (Fig. 3.4) may be attributed to the higher thermal energy. To investigate the temperature effect, we further annealed the high-*T* (170 ^{o}C) film, which had exhibited high excimer fluorescence, at 170 ^{o}C for an hour. Unexpectedly, the I_{exc} almost completely disappeared as shown in Fig. 3.6, indicating that most of the Py excimers dissociated from each other at 170^{o}C, which is above both the T_m of Py and T_g of PS, the metastable Py excimers transform

into a lower energy state due to the relaxations of PS and melting of Py, resulting in the low I_{exc}.

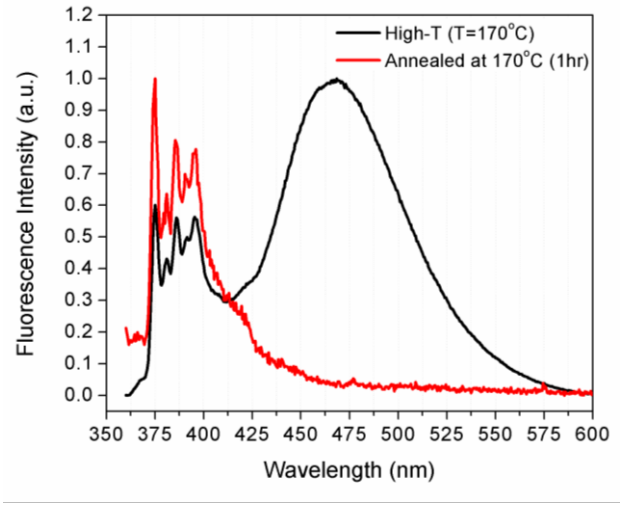

Fig. 3.6. The fluorescence emission spectra of a fresh prepared high-T (170 °C) Py/PS/$TBAPF_6$ film and after being annealed at 170 °C for 1hr. The initial prominent I_{exc} completely disappears after the annealing process.

Therefore, instead of promoting the formation of Py excimers, high temperature effectively results in dissociation of the Py excimers in solid state. Then, what is the true determining parameter that promotes the formation of the Py excimer in the Py/PS/$TBAPF_6$ thin films? The current data suggest that Py excimer fluorescence is presumably related to the solvent condition which is strongly affected by temperature and preparation procedure. Another solvent property closely related to temperature is vapor pressure. Therefore, our third attempt is to investigate the relationship between the Py excimer formation and THF vapor pressure.

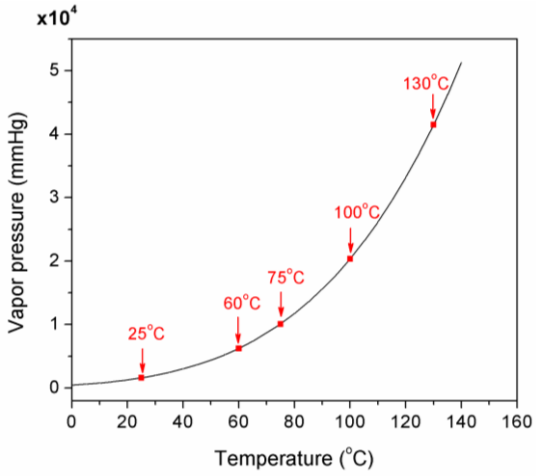

Fig 3.7. Estimated THF vapor pressure (mmHg) as a function of temperature, calculated by $\ln(P_{THF}) = A * \ln(T) + B/T + C + D * T^2$, where the units for P_{THF} and T are in kPa and K, respectively. The coefficients of A, B, C and D are 9.609, -6.340 x 10^3, 78.36 and 8.183 x 10^{-6}, respectively.[43] The arrows indicate all the experimental temperatures.

3.3.2. Vapor Pressure Effect

The vapor pressure of THF can be estimated as a generalized function of temperature [42] and exhibits a non-linear increase with increased *T* in Fig. 3.7. Here, two new approaches are taken to understand the vapor pressure effect.

External Solvent Vapor Annealing; A room-*T* film was first prepared and its fluorescence was examined. As expected, a low I_{exc}/I_{mon} value (0.18 ~ 0.19) was observed (Fig. 3.8). The film was then annealed with 50 μL and 1.0 mL of THF, respectively, at 95 °C in a sealed container (250 mL) as shown in Scheme 3.2. The vapor pressure of THF, P_{THF} in both cases can be estimated using non-ideal equation of state: $P_{THF}V = Z_{THF}N_{THF}RT$, where

V, Z_{THF}, N_{THF} and R are the volume of the container, compressibility factor of THF, mole number of THF and gas constant.

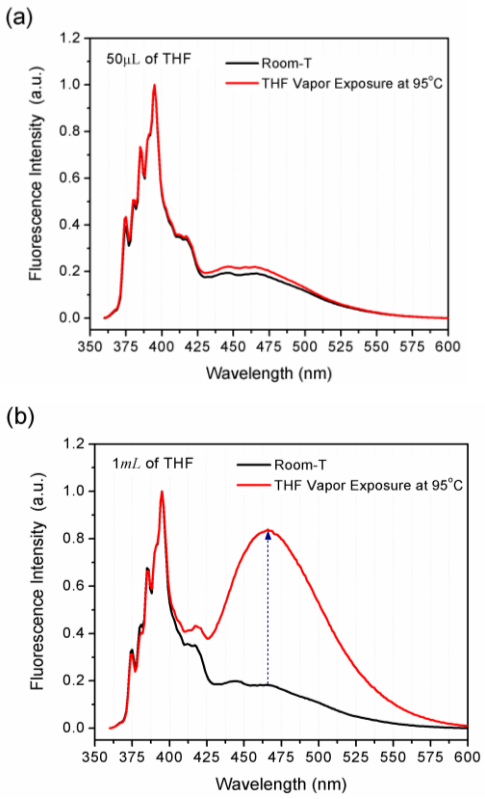

Fig 3.8 The fluorescence emission spectra of room-*T* film (black) and after being annealed with (a) 50μl and (b) 1 mL of THF vapor pressure in the closed system at 95°C (red)

The value of Z_{THF} can be estimated with a reasonable accuracy by Eq(1), where P_c ,T_c, and ω are the critical pressure (= 51.2 atm) , temperature (= 540.2 K) and acentric factor (= 0.217) of THF [43]. Since N_{THF} can be calculated by the volumes (50 μl and 1.0 mL, respectively) and density of the THF (0.8892 g/cm^3), the P_{THF} can be obtained: 57 mmHg and 1126

mmHg in the cases of 50 μl and 1.0 mL, respectively. It is also assumed that the containers were well sealed and thus that P_{THF} can be larger than 760 mmHg.[44]

$$Z_{THF} = 1 + \left(0.083 - \frac{0.0422}{T_r^{1.6}}\right)\frac{P_r}{T_r} + \omega\left(0.139 - \frac{0.172}{T_r^{3.2}}\right)\frac{P_r}{T_r} \quad (3.3.1)$$

where $T_r = \frac{T}{T_c}$, $P_r = \frac{P_{THF}}{P_c}$ and ω is the acentric factor. After 20 minutes of vapor annealing at 95 °C, the fluorescence of films was then examined again to compare with the pre-annealed samples.

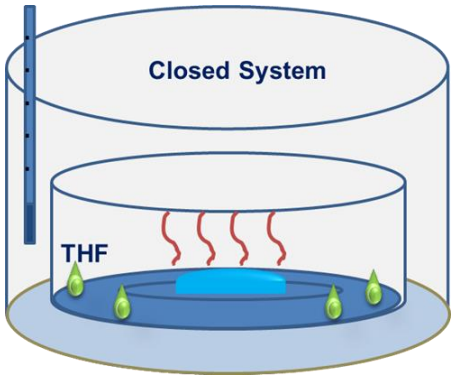

Scheme 3.2. The experimental design to control THF vapor pressure in an isothermal closed system. The vapor pressure is adjusted by the temperature and the volume of THF enclosed in the system.

Fig. 3.8 shows important and interesting results of the films under two different THF vapor pressures. There is a marginal change of fluorescence spectrum in the case of low P_{THF} (i.e., 57 mmHg) compared with that of pre-annealed sample [Fig. 3.8(a)], while a significant increase of I_{exc} is found [Fig. 3.8(b)] when the film is annealed under 1125 mmHg of THF. This finding addresses two important issues: (1) the high I_{exc}/I_{mon} is

presumably induced by the high solvent vapor pressure instead of temperature (for both being at 95 ^{o}C) and (2) the I_{exc}/I_{mon} of a solid sample can be greatly enhanced by a simple post-process high solvent vapor pressure annealing. The pressure effect on the pyrene excimer *in solution* has been studied previously [44-45] and it has been confirmed that the mechanism of Py excimer is mainly governed by the diffusional process. As a result, the high pressure in the solution state inhibits the formation of the excimers. In this study, we focus on the excimer fluorescence in the

Table 3.2. The fluorescence intensity ratio of I_{exc} (at 466 nm)/I_{mon} (at 395nm) peaks and ratio of I_1/I_3 (at I_1~ 373nm, I_3~ 384nm) of different films [exposed by high vapor pressure (1 mL) and low vapor pressure (50 μL), respectively].

Vapor Exposure	50μl of THF Vapor		1ml of THF Vapor	
	I_1/I_3	I_{exc}/I_{mon}	I_1/I_3	I_{exc}/I_{mon}
Before	0.546	0.191	0.491	0.183
After	0.591	0.220	0.473	0.834

solid-state Py/PS/$TBAPF_6$ film, being exposed to the high solvent vapor pressure, which presumably not only enhances the mobility of Py in the presence of PS/$TBAPF_6$ but also provides the environment for the formation of Py excimer. It should be noted that the feature of the Py monomer fluorescence (I_1/I_3) does not alter (Table 3.2), indicating that the local polarity around Py may not alter after the solvent vapor annealing.

Residual Solvent Effect: It is not clear whether the enhancement of I_{exc}/I_{mon} after high solvent vapor pressure annealing is attributed to the coexistence of THF and Py (i.e., film containing T|HF residual) or reorganization of Py alone. To differentiate the two scenarios, we monitor the fluorescence and ^{1}H-NMR spectra of a thin film undergoing a sequence of following processes: (a) initially producing room-*T* film, (b) removing the residual solvent at 60^{o}C under vacuum for overnight, and (c) annealing the sample at 100^{o}C for 5 minutes. During the whole process, there is no external THF vapor involved. ^{1}H-NMR data of the initial room-*T* evaporation film [Fig. 9(a)] indicates THF residue after solvent evaporation, where THF peak ($\delta \sim$ 3.74ppm, -OCH_2) is found and the I_{exc} is comparably low [Fig. 3.9 (b)]. This is consistent with the aforementioned result, which indicates that lower THF vapor pressure leads to the lower I_{exc}. When THF is almost completely removed from the film under vacuum at 60 ^{o}C for overnight, verified by ^{1}H-NMR in Fig. 3.10(a), the resultant I_{exc} increases double. The rationale for this observation is that the vaporization of the trapped THF residue enhances the local vapor pressure, resulting in a higher I_{exc}. It should be noted that, since the temperature (60 ^{o}C) is around the T_b of THF yet far below the T_g of PS, a good portion of metastable Py excimers is expected to form under this locally high P_{THF} (~ 625 mmHg at 60 ^{o}C). Fig. 3.9(b) also confirms that the high I_{exc} is not attributed to the coexistence of THF and Py in the final stage since THF peak disappears is the indicative of the

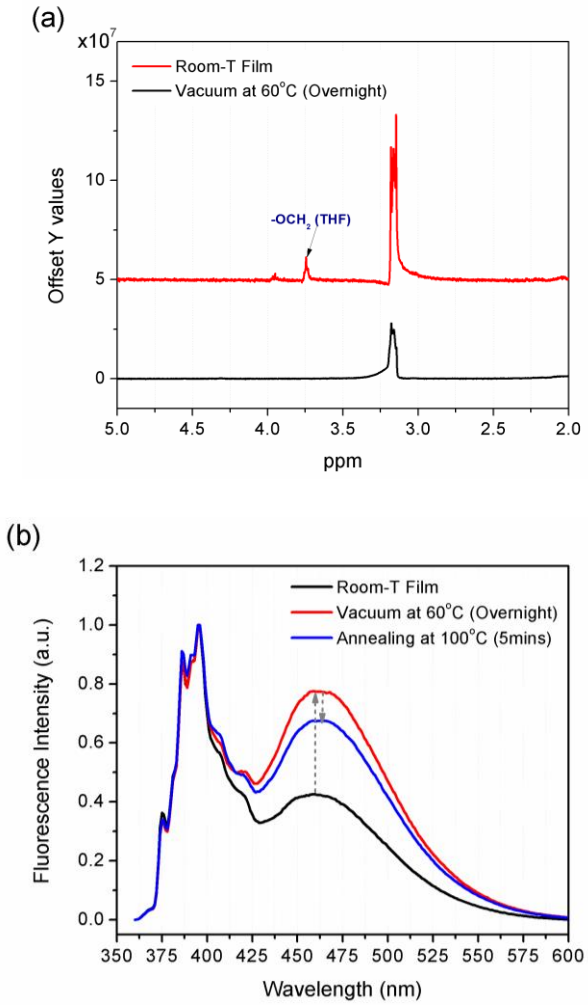

Fig 3.9 (a) ^{1}H-NMR spectra of the film prepared by room-*T* evaporation (red), then annealed at 60 ^{o}C under vacuum (black), (b) The fluorescence emission spectra of room-*T* film(black), then 60 ^{o}C under vacuum (red) and annealed at 100 ^{o}C for 5 mins (blue). The dotted arrows represent the time sequence of the process.

removal of THF. Further increase of the annealing temperature to 100 ^{o}C (~ T_g of PS) in absence of residue THF for 5 minutes decreases I_{exc} again. This phenomenon is anticipated based on the aforementioned reason – the effect

of increased mobility of the PS chains. This study further confirms that high THF vapor pressure is one of the key parameters to form Py excimer in the solid state. Consistent results have also been found in several reports on fluorescent polymers where the reduction of I_{exc} was observed as annealed at $T > T_g$ mainly because of the increased polymer chain mobility. [46-52]. Although the fluorophore (Py) is not chemically conjugated with the PS in this study, its interaction with the host PS may resemble those of flouroscent polymers where high-*T* annealing may reduce the Py fluorescence.

The observed phenomenon indicates that enhanced mobility of Py molecules alone does not facilitate the formation of Py excimers. The presence of high THF vapor pressure provides both mobility and solvent-rich environment for Py molecules to organize themselves into excimers. Our data reveal that Py/PS/$TBAPF_6$ in THF is in a non-polar environment (judging from its lower I_1/I_3, data not shown). Moreover, THF contains the electronegative atom, oxygen, which induces the dipole moment within the molecule. This local dipole-dipole interaction of solvent molecules is found possibly to distort the symmetry of the Py molecules.[39-40] Whether the enhancement of I_{exc} is combined effects of high mobility and distortion of symmetry induced by solvent dipole-dipole moment remains an open question to answer.

The current result presents a pioneering study on the formation of Py excimers in a solid state, indicating that high solvent vapor pressure annealing can greatly enhance the fluorescence of Py excimers. It should be

mentioned that, though this study identifies solvent vapor pressure being the most influential factor on the formation of Py excimers out of the three studied parameters, the main contributing factors for high Py excimer fluorescence in the case of electrospun films (prepared at room *T*) remain unclear. We speculate that the electrospun fibers may adopt the morphology of polymer annular wall with the residue THF solvent entrapped at the center as described in the literature [53]. The internal stress built up during the film drying process may locally elevate the THF vapor pressure, which can therefore enhance the Py excimer fluorescence. A more detailed study is needed to fully understand the issue.

3.4. Conclusion

We have demonstrated that the formation of Py excimers in PS/$TBAPF_6$ thin films depends greatly on the film manufacturing processes. Three parameters – temperature, evaporation rate and solvent vapor pressure – which were speculated to have the potential to control the formation of Py excimers, are decoupled and investigated independently. The result indicates that high solvent vapor pressure is the determining factor of enhancing the pyrene excimer fluorescence, while high temperature (around or greater than T_g of the polymer) has an opposite effect in absence of solvent – reducing the Py excimer fluorescence. Evaporation rate has a marginal influence over the formation of Py excimers. This study seeks for the fundamental understanding of the variation in excimer fluorescence

from the Py/PS/$TBAPF_6$ films made by different procedures. The principle can be presumably applied to general fluorescence sensing materials containing Py or Py-derivatives as fluorophores, providing the insight to improving their sensitivity. Future attempts in understanding the different mechanisms between electrospun and high-*T* evaporation films and the effects of PS and $TBAPF_6$ salt on the excimer fluorescence will be investigated to advance our knowledge of the function-structure relationship of fluorophores in the solid state in order to design more efficient sensing materials.

3.5. Supplementary Information

Time-dependent photoluminescence is conducted on two thin-film samples (electrospun and high-T evaporation) to compare their fluorescence quenching efficiency in presence of 2,4, DNT. The measurements were taken using a Varian Cary Eclipse fluorescence spectrophotometer (Agilent Technologies). Saturated 2,4-DNT vapor was initially reached in a sealed methacrylate cuvette coexisting with solid 2,4-DNT solid. Small cotton was placed on top of the solids to avoid direct contact with the testing film, which was then inserted in the cell at a 45^o angle. The emission spectrum was recorded in the wavelength region of 360–600 nm (with an excitation wavelength of 340 nm) immediately after the film was placed in the cell at a time interval of 36s. Fig S1 shows a faster quenching rate of the electrospun film than that of the high-T evaporation one, although they have

the similar initial I_{exc}. The difference can be presumably explained by the highly porous structure in the electrospun film (Fig 3), increasing the accessibility of the DNT molecules to pyrene. A new strategy to design high-T evaporation films with a high surface-to-volume ratio in a controllable manner is in progress in order to identify the reasons for the fast quenching mechanism.

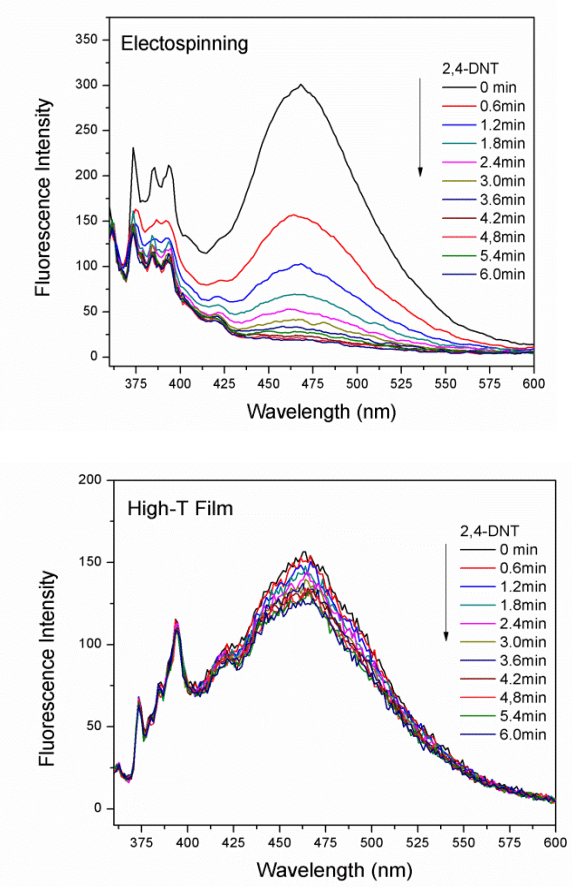

Fig. 3.S1. The time-dependent fluorescence intensity of electrospun film and high-T Film upon exposure to equilibrium 2,4-DNT vapor (the exposure time from top to bottom are 0, 0.6, 1.2, 1.8, 2.4, 3, 3.6, 4.2, 4.8, and 6 min, respectively).

3.6. References

1. Hong, Y.; Lam, J. W.; Tang, B. Z., Aggregation-induced emission: phenomenon, mechanism and applications. *Chemical communications* **2009,** (29), 4332-53.

2. Wang, Y.; La, A.; Ding, Y.; Liu, Y.; Lei, Y., Novel Signal-Amplifying Fluorescent Nanofibers for Naked-Eye-Based Ultrasensitive Detection of Buried Explosives and Explosive Vapors. *Advanced Functional Materials* **2012**, In Press.

3. Bittermann, H.; Siegemund, D.; Malinovskii, V. L.; Häner, R., Dialkynylpyrenes: Strongly Fluorescent, Environment-Sensitive DNA Building Blocks. *Journal of the American Chemical Society* **2008,** *130* (46), 15285-15287.

4. Uno, S.; Dohno, C.; Bittermann, H.; Malinovskii, V. L.; Haner, R.; Nakatani, K., A Light-Driven Supramolecular Optical Switch. *Angew Chem Int Edit* **2009,** *48* (40), 7362-7365.

5. Fujimoto, K.; Shimizu, H.; Inouye, M., Unambiguous Detection of Target DNAs by Excimer−Monomer Switching Molecular Beacons. *The Journal of Organic Chemistry* **2004,** *69* (10), 3271-3275.

6. Trkulja, I.; Biner, S. M.; Langenegger, S. M.; Haner, R., A molecular probe for the detection of homopurine sequences. *Chembiochem* **2007,** *8* (1), 25-27.

7. Conlon, P.; Yang, C. Y. J.; Wu, Y. R.; Chen, Y.; Martinez, K.; Kim, Y. M.; Stevens, N.; Marti, A. A.; Jockusch, S.; Turro, N. J.; Tan, W. H., Pyrene excimer signaling molecular beacons for probing nucleic acids. *Journal of the American Chemical Society* **2008,** *130* (1), 336-342.

8. Thomas, S. W.; Joly, G. D.; Swager, T. M., Chemical sensors based on amplifying fluorescent conjugated polymers. *Chemical Reviews* **2007,** *107* (4), 1339-1386.

9. Belletête, M.; Bouchard, J.; Leclerc, M.; Durocher, G., Photophysics and Solvent-Induced Aggregation of 2,7-Carbazole-Based Conjugated Polymers. *Macromolecules* **2005,** *38* (3), 880-887.

10. Menon, A.; Galvin, M.; Walz, K. A.; Rothberg, L., Structural basis for the spectroscopy and photophysics of solution-aggregated conjugated polymers. *Synthetic Metals* **2004,** *141* (1–2), 197-202.

11. Chen, C.-T., Evolution of Red Organic Light-Emitting Diodes: Materials and Devices. *Chemistry of Materials* **2004,** *16* (23), 4389-4400.

12. Grell, M.; Bradley, D. D. C.; Ungar, G.; Hill, J.; Whitehead, K. S., Interplay of Physical Structure and Photophysics for a Liquid Crystalline Polyfluorene. *Macromolecules* **1999,** *32* (18), 5810-5817.

13. Jakubiak, R.; Collison, C. J.; Wan, W. C.; Rothberg, L. J.; Hsieh, B. R., Aggregation quenching of luminescence in electroluminescent conjugated polymers. *J Phys Chem A* **1999,** *103* (14), 2394-2398.

14. Grell, M.; Bradley, D. D. C.; Long, X.; Chamberlain, T.; Inbasekaran, M.; Woo, E. P.; Soliman, M., Chain geometry, solution aggregation and enhanced dichroism in the liquid-crystalline conjugated polymer poly(9,9-dioctylfluorene). *Acta Polym* **1998,** *49* (8), 439-444.

15. Lemmer, U.; Heun, S.; Mahrt, R. F.; Scherf, U.; Hopmeier, M.; Siegner, U.; Gobel, E. O.; Mullen, K.; Bassler, H., Aggregate Fluorescence in Conjugated Polymers. *Chemical Physics Letters* **1995,** *240* (4), 373-378.

16. Geddes, C. D. L., J. R., *Advanced Concepts in Fluorescence Sensing*. Springer, Norwell: **2005**.

17. Tan, W. H.; Wang, K. M.; Drake, T. J., Molecular beacons. *Curr Opin Chem Biol* **2004,** *8* (5), 547-553.

18. Sapsford, K. E.; Berti, L.; Medintz, I. L., Materials for fluorescence resonance energy transfer analysis: Beyond traditional donor-acceptor combinations. *Angew Chem Int Edit* **2006,** *45* (28), 4562-4588.

19. Borisov, S. M.; Wolfbeis, O. S., Optical biosensors. *Chemical Reviews* **2008,** *108* (2), 423-461.

20. Sagara, Y.; Mutai, T.; Yoshikawa, I.; Araki, K., Material design for piezochromic luminescence: Hydrogen-bond-directed assemblies of a pyrene derivative. *Journal of the American Chemical Society* **2007,** *129* (6), 1520-1521.

21. Sagara, Y.; Kato, T., Stimuli-responsive luminescent liquid crystals: Change of photoluminescent colors triggered by a shear-induced phase transition. *Angew Chem Int Edit* **2008,** *47* (28), 5175-5178.

22. Sagara, Y.; Kato, T., Mechanically induced luminescence changes in molecular assemblies. *Nat Chem* **2009,** *1* (8), 605-610.

23. Sagara, Y.; Yamane, S.; Mutai, T.; Araki, K.; Kato, T., A Stimuli-Responsive, Photoluminescent, Anthracene-Based Liquid Crystal: Emission Color Determined by Thermal and Mechanical Processes. *Advanced Functional Materials* **2009,** *19* (12), 1869-1875.

24. Oh, H.; Kim, J.; Kim, E., Holographic Recording on Photopolymers Containing Pyrene for Enhanced Fluorescence Intensity. *Macromolecules* **2008,** *41* (19), 7160-7165.

25. Ivan, M. G.; Scaiano, J. C., Lithography Based on Memory Effects Resulting from Photoinduced Self-Assembly of Pyrene Dimers in Thin Polymer Films. *Chemistry of Materials* **2009,** *21* (17), 3933-3940.

26. Fujiwara, H.; Hayashi, T.; Fukumura, H.; Masuhara, H., Each dopant can absorb more than ten photons: Transient absorbance measurement at excitation laser wavelength in polymer ablation. *Applied Physics Letters* **1994,** *64* (18), 2451-2453.

27. Birks, J. B., Excimers. *Reports on Progress in Physics* **1975,** *38* (8), 903.

28. Winnik, M. A., End-to-end cyclization of polymer chains. *Accounts of Chemical Research* **1985,** *18* (3), 73-79.

29. Birks, J. B., *Photophysics of Aromatic Molecules*. Wiley: London, **1970**.

30. Winnik, F. M., Photophysics of preassociated pyrenes in aqueous polymer solutions and in other organized media. *Chemical Reviews* **1993,** *93* (2), 587-614.

31. Seo, Y. J.; Hwang, G. T.; Kim, B. H., Quencher-free molecular beacon systems with two pyrene units in the stem region. *Tetrahedron Lett* **2006,** *47* (24), 4037-4039.

32. Wilson, J. N.; Teo, Y. N.; Kool, E. T., Efficient quenching of oligomeric fluorophores on a DNA backbone. *Journal of the American Chemical Society* **2007,** *129* (50), 15426-+.

33. Birks, J. B.; Christophorou, L. G., Excimer fluorescence spectra of pyrene derivatives. *Spectrochimica Acta* **1963,** *19* (2), 401-410.

34. Seko, T.; Ogura, K.; Kawakami, Y.; Sugino, H.; Toyotama, H.; Tanaka, J., Excimer emission of anthracene, perylene, coronene and pyrene microcrystals dispersed in water. *Chemical Physics Letters* **1998,** *291* (3–4), 438-444.

35. Romashko, T. P.; Khakhel, O. A., Spectral criterion of the state of thermodynamic equilibrium of molecular excimers. *Journal of Applied Spectroscopy* **2003,** *70* (4), 509-512.

36. Nautiyal, A.; Bisht, P. B., Steady state and time-resolved studies of pyrene in solution and in single microcrystals. *Journal of Luminescence* **2010,** *130* (10), 1829-1833.

37. Glushko, V.; Thaler, M. S. R.; Karp, C. D., Pyrene fluorescence fine structure as a polarity probe of hydrophobic regions: Behavior in model solvents. *Archives of Biochemistry and Biophysics* **1981,** *210* (1), 33-42.

38. Ndou, T. T.; von Wandruszka, R., Pyrene fluorescence in premicellar solutions: The effects of solvents and temperature. *Journal of Luminescence* **1990,** *46* (1), 33-38.

39. Chen, S. H.; Mcguffin, V. L., Temperature Effect on Pyrene as a Polarity Probe for Supercritical-Fluid and Liquid Solutions. *Appl Spectrosc* **1994,** *48* (5), 596-603.

40. Langkilde, F. W.; Thulstrup, E. W.; Michl, J., The effect of solvent environment on molecular electronic transition moment directions: Symmetry lowering in pyrene. *The Journal of Chemical Physics* **1983,** *78* (6), 3372-3381.

41. Silberberg, M. A., *Chemistry*. McGraw-Hill New York, **2006**.

42. Perry, R. H., Green, D.W. , *Perry's Chemical Engineers' Handbook*. McGraw-Hill: **2007**

43. KDB Equation. http://www.cheric.org/research/kdb/hcprop/showcoef.php?cmpid=1035&prop=PVP.

44. Johnson, P. C.; Offen, H. W., Effect of Pressure on Pyrene Excimer Fluorescence in Toluene. *The Journal of Chemical Physics* **1972,** *56* (4), 1638-1642.

45. Macdonald, A. G.; Wahle, K. W. J.; Cossins, A. R.; Behan, M. K., Temperature, pressure and cholesterol effects on bilayer fluidity; a comparison of pyrene excimer/monomer ratios with the steady-state fluorescence polarization of diphenylhexatriene in liposomes and microsomes. *Biochimica et Biophysica Acta (BBA) - Biomembranes* **1988,** *938* (2), 231-242.

46. Lefkowitz, S. M.; Leugers, M. A., Annealing effects on the intrinsic fluorescence of PBO/amorphous nylon blends. *Polymer* **1994,** *35* (5), 1090-1091.

47. Osaheni, J. A.; Jenekhe, S. A., New red light-emitting conjugated rigid-rod polymer: poly(benzobisthiazole-1,4-phenylenebisvinylene). *Macromolecules* **1993,** *26* (17), 4726-4728.

48. Fu, Y.; Lakowicz, J. R., Spectroscopy: A closer look at polymer annealing. *Nature* **2011,** *472* (7342), 178-179.

49. Smilowitz, L.; Hays, A.; Heeger, A. J.; Wang, G.; Bowers, J. E., Time-resolved photoluminescence from poly[2-methoxy, 5-(2[script ']-ethyl-hexyloxy)-p-phenylene-vinylene]: Solutions, gels, films, and blends. *The Journal of Chemical Physics* **1993,** *98* (8), 6504-6509.

50. Huttner, S.; Sommer, M.; Chiche, A.; Krausch, G.; Steiner, U.; Thelakkat, M., Controlled solvent vapour annealing for polymer electronics. *Soft Matter* **2009,** *5* (21), 4206-4211.

51. Gregg, B. A., Evolution of photophysical and photovoltaic properties of perylene bis(phenethylimide) films upon solvent vapor annealing. *J. Phys. Chem.* **1996,** *100* (2), 852-859.

52. Conboy, J. C.; Olson, E. J. C.; Adams, D. M.; Kerimo, J.; Zaban, A.; Gregg, B. A.; Barbara, P. F., Impact of Solvent Vapor Annealing on the Morphology and Photophysics of Molecular Semiconductor Thin Films. *The Journal of Physical Chemistry B* **1998,** *102* (23), 4516-4525.

53. Arinstein, A.; Zussman, E., Postprocesses in tubular electrospun nanofibers. *Physical Review E* **2007,** *76* (5), 056303.

Chapter 4

Unique Effects of the Chain Lengths and Anions of Tetraalkylammonium Salts on Pyrene Excimer Quenching

4.1. Introduction

Pyrene (Py) is a polycyclic aromatic hydrocarbon molecule made of four fused benzene rings without heteroatoms.[1] One remarkable feature of such polycyclic aromatic hydrocarbons is their significant fluorescence due to its electron-rich structures. This fluorescence can be effectively quenched by certain electron deficient molecules, providing a useful platform to detect these specific molecules.[2] In this regard, Py and its derivatives in solution and solid state have been successfully applied to many fields such as sensors for ions[2-6], explosives[7-10], optical switches[11-12], monitors for micelles formations[13-15], and biological probes for DNA and RNA.[16-18] In spite of its many applications, the origin of solid-state Py excimer fluorescence has not been systemically studied (except the case of π–π stacking[19]) as most research efforts have been made on synthesis of various Py derivatives.[4, 13, 15-16, 19-21]

Two types of emission from the excited states of Py molecules are commonly observed: the ultra-violet (UV) emission (370 to 400 nm) from unassociated excited monomers (M_1^*) and a blue emission (440 ~ 490 nm) from Py excimers (E^*). The latter forms due to the interaction between a ground-state monomer (M_1) and an excited monomer (M_1^*).[1, 22] The intermolecular distance (d) between Py, can dictate the types of fluorescence: ~ 1 nm for monomer and 0.4 nm < d < 1 nm for excimer.[1, 20, 23-25] In the solution state, the formation of Py excimer is mostly attributed to molecular diffusion process.[1, 20, 22] Therefore, a high Py concentration enhances the formation of Py excimers until self-quenching occurs.[26] Another factor that promotes the formation of Py excimer is the long lifetime of Py monomer, τ_M (~ 450 ns) and high monomer quantum efficiency (Φ_M=0.6 in cyclohexane).[1, 20, 27] However, in the solid state, the formation and quenching mechanisms of excimer are likely different from the solution state due to its relatively low molecular diffusivity.[28-30]

It has been reported that Py excimer in a simple ternary electrospun mixtures containing tetrabutylammonium hexafluorophosphate ($TBAPF_6$) and polystyrene (PS) can be effectively quenched in presence of a trace amount (at a ppb level) of nitro-explosives (e.g., nitro-aromatic, nitro-glycerin, or nitro-amine compounds) over a short period of time (in 6 minutes).[7] A recent report showed that the Py excimer fluorescence in a PS/Py/$TBAPF_6$ film can also be greatly enhanced by high solvent vapor pressure induced by temperature, indicating that the solvent molecules

(tetrahydrofuran, THF, in this case) promote certain configurations of Py to form excimers.[31] Since both PS and $TBAPF_6$ can, in principle, affect the Py excimer fluorescence, it is difficult to differentiate the contribution of individual components to the Py fluorescence in the ternary system. In the past, Py fluorescence was found quenched by impurity, concentration, formation of exciplex, energy transfer, and so forth.[22] Moreover, salts and ions are also found to be able to quench the fluorescence of Py derivatives[32-33], and/or Py-exciplex[34] in solutions[35] and gels[36].[35, 37-39]

This paper presents a systematic study on the effects of the chemical structure of anions and the chain lengths of a series of tetraalkylammonium salts on the Py excimer quenching in a binary system (namely, Py and salt) in both solution and solid states. The obtained knowledge is applicable for designing high-sensitivity sensors which can be manufactured in large quantities. The important parameters that control the fluorescence emission of the Py excimer are therefore determined. The fluorescence decay rate provides an insight to the excimer quenching mechanism (most likely dynamic quenching). The polarity around and mobility of Py molecules are also correlated with the excimer fluorescence. However, insignificant change in the nano-structures characterized by X-ray diffraction (XRD) and scanning electron microscopy (SEM) of different Py/salt systems suggests that such quenching behavior may not be closely related to the formation of a new crystalline structure or topological variations. Several important findings are summarized as follows: (1) TBA^+ has a drastic quenching effect

on the Py excimer, (2) in the case of $TBAPF_6$, the quenching effect is dictated by the solution temperature during the evaporation process, (3) the mobility of Py is crucial in recovering excimer fluorescence even under a high solvent vapor pressure, (4) increased hydrophobicity around Py results in enhanced Py excimer and (5) the process mainly involves dynamic instead of static quenching.

4.2. Experiment

Materials and Procedures

-Materials

All the chemical components of salts listed in Table 1, pyrene (Mw 202.25g/mol), and acetone (purity > 99.9%) were purchased from Sigma Aldrich and used as received.

Table 4.1. List of a series of tetraalkylammonium salts in this study

Name	Molecular weight (g/mol)	Name	Molecular weight (g/mol)
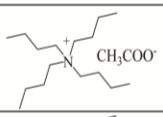 TBA Acetate	301.52	 $TMAPF_6$	219.11
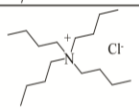 TBACl	277.92	 $TEAPF_6$	275.22
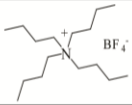 $TBABF_4$	329.27	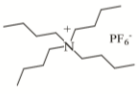 $TBAPF_6$	387.43
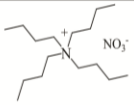 $TBANO_3$	304.47	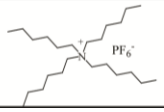 $THAPF_6$	499.64

Sample Preparation

Solutions: Py in acetone solution was prepared at different concentrations (10^{-4}, 10^{-3}, 10^{-2}, 5×10^{-2}, 10^{-1}, and 2×10^{-1} M, respectively). In order to investigate the effect of salts on the Py fluorescence emission, the Py/salt binary mixtures were prepared in the acetone at a fixed weight ratio of salt-to-Py (71.2:28.8 by weight). All concentrations of different salts in the solutions are under the critical micellation concentrations (CMC) confirmed by DLS (Dynamic Light Scattering).

Films: Film samples were prepared for the following studies: (1) differentiating the quenching effects of PS and $TBAPF_6$ on the Py excimer, and (2) investigating the key parameters of studied tetraalkylammonium salts affecting the emission of Py excimer. For the first purpose, ternary $TBAPF_6$/PS/Py samples were made at various compositions of $TBAPF_6$ (from 13 to 63 wt. %), where the concentration of Py remains constant (i.e., 18.3 wt. %). A binary film composed of Py/PS (1:2 by weight) was also made to compare with the ternary $TBAPF_6$/PS/Py film of the same Py/PS ratio. In order to study the controlling parameters of the salts, binary systems containing both Py and a series of tetraalkylammonium salts were prepared at a fixed salt-to-Py weight ratio of (71.2: 28.8) and a constant Py concentration (0.02 g/mL) in acetone. All the films were made by solvent evaporation at either high-*T* (100^{o}C) or room-*T*. The glass substrates were first preheated to the desired temperature and allowed to equilibrate for ~ 1

hour. Then, a 100 μL of the Py/salt solution was placed on the pre-heated substrate for 2 mins and let it cool at room-*T* till fully dried.

Characterization

The fluorescence emission, ^{13}C-Nuclear Magnetic Resonance (NMR), and lifetime of fluorophores in Py/salt films were characterized in this study.

(1) Fluorescence and UV-Abs: The fluorescence spectra were measured by a steady-state fluorescence spectrometer (Flourolog, Jobin Yvon Horiba). The excitation wavelength of 334 nm for the Py/salt was chosen based on the maximum UV absorption, except that a wavelength of 350 nm was used for the films containing PS. The emission spectra were monitored through a 1-mm slit over the wavelength range of 350 – 600 nm and normalized by the maximum intensity in the corresponding spectrum. In this study, the fluorescence ratio of excimer-to-monomer, I_{exc}/I_{mon}, is used as an index to evaluate the content of Py excimer. The absorption spectra were recorded on a UV-vis spectrophotometer (Cary 50, Agilent Technologies).

(2) ^{13}C- NMR: The solid-state ^{13}C cross-polarization magic-angle spinning (CPMAS) NMR spectra were acquired using a Bruker DMX 300 NMR spectrometer operating at a field strength of 7.05 T, a resonance frequency of 300 MHz for ^{1}H and 75.4 MHz for ^{13}C. Chemical shifts were obtained based on an external reference sample, solid glycine (carbonyl at 176.5 ppm). ^{13}C-NMR measurements were taken in the absence or presence of the salts.

(3) Fluorescence Lifetime Measurement: The samples were excited with a pulse diode laser (PicoQuant) at 405 nm with a repetition rate of 2.5 MHz. The emission of the samples was focused onto an avalanche photodiode (PicoQuant) using a 450 nm long-pass spectral filter to examine excimer alone. The fluorescence decay was recorded using a time-dependent single photon counting module (Picoharp300, PicoQuant). The data were then normalized by the maximum intensity in the corresponding decay curves and was subtracted by the initial background intensity.

(4) SEM: The morphology of films was measured by the JEOL 6335F Field Emission SEM (SM-6335F), a cold cathode field emission scanning electron microscope, which provides a resolution of 1.5nm at 15kV and 5.0nm at 1kV.

(5) XRD: The XRD pattern of the film was obtained through a regular θ-2θ configuration by a Bruker D8 Advance X-Ray Diffractometer with a 2.2 kW Cu-anode sealed tube. The XRD data were analyzed after background subtraction and expressed in an arbitrary unit.

4.3. Results and Discussion

Fig.4. 1(A) shows the fluorescence spectra (excited at 350 nm) of two polymer thin films prepared by solvent evaporation at room temperature: Py/PS/$TBAPF_6$ and Py/PS, respectively. In spite of the same weight Py/PS ratio, the excimer emission peak (465 nm) is prominent in the PS/Py film but nearly nonexistent in the presence of $TBAPF_6$, indicating that $TBAPF_6$

effectively quenches the Py excimer. A follow-up study was conducted on a ternary system (PS/Py/$TBAPF_6$) where the composition of $TBAPF_6$ varies from 13 wt. % to 63 wt. % (with a constant Py concentration of 18 wt. %) as shown in Fig.4. 1(B). The result indicates nearly complete quenching of the Py excimer in the films as the $TBAPF_6$ concentrations ≥ 45 wt. %. To further explore the interaction of the salt and Py as well as its influence on the fluorescence of Py excimer, films composed of Py and other tetraalkylammonium salts with a variety of anions and cations in place of $TBAPF_6$ were studied in both solution and solid states.

4.3.1. Salt Effects on the Formation of Py excimer in Solution State

It has been known that I_{exc}/I_{mon} *in solution state* is governed by the molecular mobility (i.e., diffusion) and the concentration of Py molecules.[22, 40-41] In this study, the polarity around Py determined by its monomer emission is also investigated to correlate with I_{exc}/I_{mon}. The five vibronic fine structures of the pyrene monomer give rise to five fluorescence peaks from 370 to 400 nm (namely from I_1 to I_5), depending on the polarity of its environment. The higher the I_1/I_3 value, the more polar is the solvent environment.[42-44] Although the formation of Py excimers (I_{exc}/I_{mon}) and the polarity of the Py environment (I_1/I_3) have been previously reported together,[38, 45] they have not been closely examined and correlated because the studied Py concentrations were low thus resulting in insignificant excimer emission. Fig.4. 2(A) shows that the emission of Py excimer in

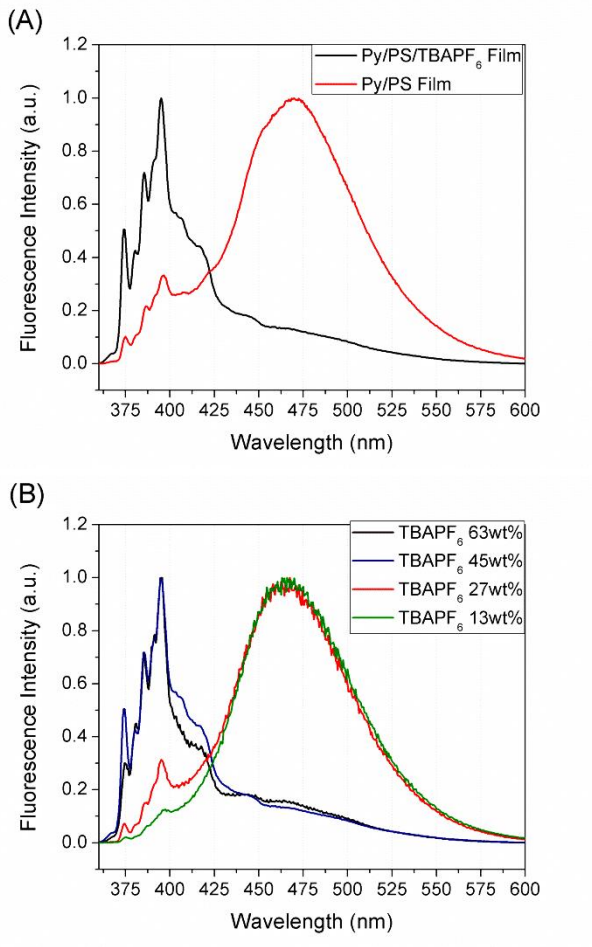

Fig.4.1. Fluorescence spectra (excited at 350 nm) of (A) Py/PS/$TBAPF_6$ film (black) and Py/PS film (red) prepared by room-T evaporation. (B) Py/PS/$TBAPF_6$ films prepared at room T with different salt compositions, 63wt % (black), 45wt% (blue), 27wt% (red), and 13wt% (green), respectively.

acetone is enhanced drastically (high I_{exc}/I_{mon}) above 0.05 M of the Py concentration, where the polarity of Py also starts to decrease (low I_1/I_3), representing that the hydrophobic environment around Py is strongly related to the formation of excimer in the solution. In regards to Py concentration, Fig 2(B) indicates that the excimer intensity decreases significantly as the Py concentration is lower than 0.05 M. A similar approach was taken to evaluate the effect of various tetraalkylammonium salts on the fluorescence of Py excimer, including a series of salts associated with the same cation (i.e., TBA^+ chain) but different anions as well as another series of salts which have the same anion (i.e., PF_6^-) but different chain lengths of tetraalkylammonium. The I_{exc}/I_{mon} increases and the I_1/I_3 decreases with increased Py concentration regardless of the types of salts listed in Table 4S.1, revealing no significant dependence of the chemical structures of the salts on the formation of Py excimer in solution state.

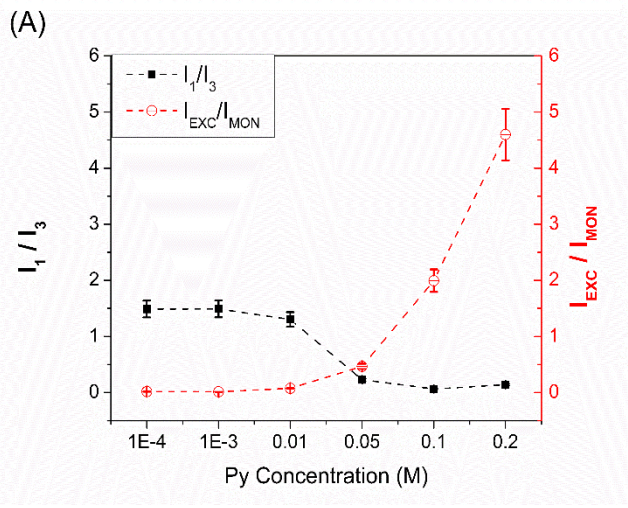

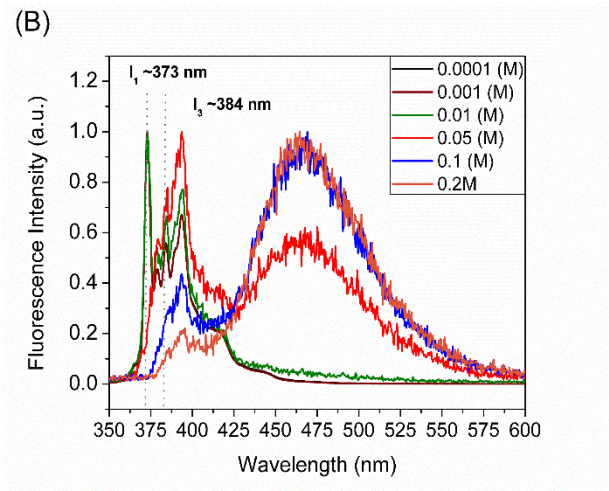

Fig.4. 2. (A) The ratios of I_{exc}/I_{mon} (open circles, red) and I_1/I_3 (solid squares, black) as a function of Py concentration. The I_{exc}/I_{mon} increases and I_1/I_3 decreases with increased Py concentration. The error ranges of these values are within 10%. (B) The fluorescence emission spectra (excited at 343 nm) of Py in acetone solution at different concentrations (M). (10^{-4}, 10^{-3}, 10^{-2}, 5×10^{-2}, 10^{-1}, and 2×10^{-1}, respectively)

4.3.2. Py Excimer Fluorescence in Presence of Salts in Solid State

– Effect of salt structures and film preparation methods

In solid state, the effect of salts on the formation of Py excimer can be significantly different from that in solution. The fluorescence spectra of Py/salt thin films made from the solutions by solvent evaporation at two different temperatures are investigated. Fig.4. 3 (A) and (B) illustrate the fluorescence spectra of the Py/salt thin films. In contrast to the solution state, the excimer quenching in the films is strongly affected by the chemical structures of the salts. When comparing different anions in the case of TBA^+ cation [Fig.4. 3(A)], most of the films show low Py excimer fluorescence except for that of Py/TBA acetate. However, when we compare the effect of different cations [Fig.4. 3(B)], an unexpected phenomenon is observed that the excimer fluorescence is inhibited only by $TBAPF_6$, a salt with a specific chain length of 4 carbons, while both Py/$TEAPF_6$ and Py/$THAPF_6$ films show a strong excimer peak. Since $TMAPF_6$ (tetramethylammonium PF_6) is not soluble in acetone, the Py/$TMAPF_6$ film was made by evaporation of a Py/$TMAPF_6$/dimethylformamide (DMF) solution, where both Py and $TMAPF_6$ are soluble. The emission spectrum also shows high excimer fluorescence. The result indicates that only $TBAPF_6$ has a quenching effect on Py excimer as prepared at room T.

Fig.4. 3 (C) and (D) are the fluorescence spectra of thin films (Py in various salts) prepared at high-*T* (100 ^oC) evaporation. This preparation method is chosen because enhanced excimer was found in the ternary film

composed of PS/Py/$TBAPF_6$ under the same process.[31] Here, a significant difference in I_{exc}/I_{mon} is also found between the high-*T* and room-*T* evaporation films in the binary Py/$TBAPF_6$ system. However, the other Py/salt systems do not show strong temperature dependence in excimer fluorescence. *Apparently, $TBAPF_6$ behaves differently from the other salts in this study.*

Previously, it has also been reported that the excimer fluorescence of the ternary film (PS/Py/$TBAPF_6$) increases significantly after annealing a film of low excimer emission under a high solvent vapor pressure.[31] The enhancement of excimer fluorescence was explained by high solvent vapor pressure inducing the formation of Py excimers. The same approach is

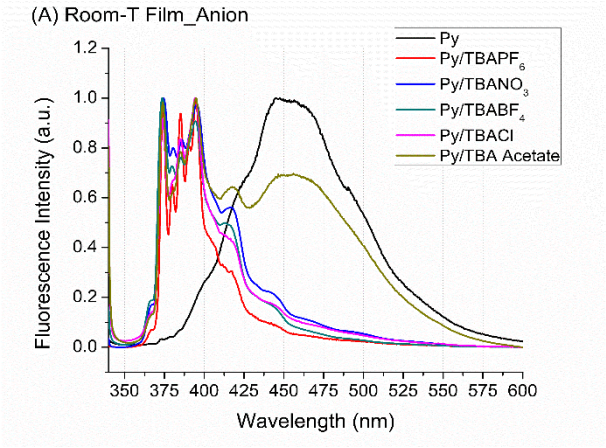
(A) Room-T Film_Anion
Py
Py/TBAPF6
Py/TBANO3
Py/TBABF4
Py/TBACl
Py/TBA Acetate
Fluorescence Intensity (a.u.)
Wavelength (nm)

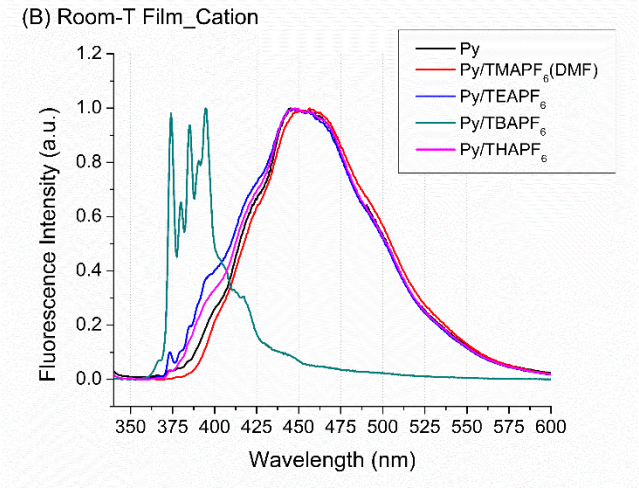
(B) Room-T Film_Cation
Py
Py/TMAPF6(DMF)
Py/TEAPF6
Py/TBAPF6
Py/THAPF6
Fluorescence Intensity (a.u.)
Wavelength (nm)

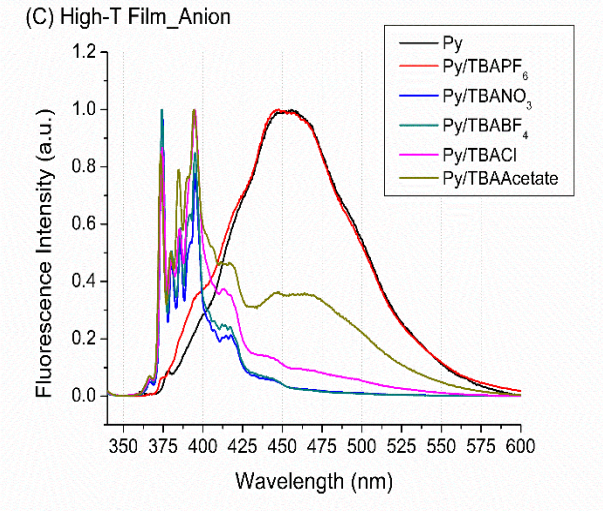
(C) High-T Film_Anion
Py
Py/TBAPF6
Py/TBANO3
Py/TBABF4
Py/TBACl
Py/TBAAcetate
Fluorescence Intensity (a.u.)
Wavelength (nm)

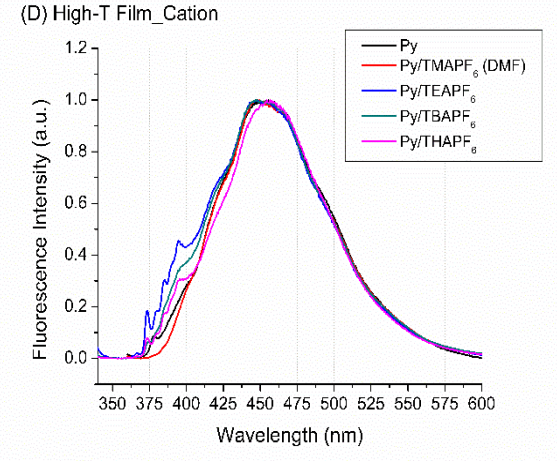

Fig.4. 3. Fluorescence spectra (excited at 334 nm) of the films composed of Py and a variety of salts (A) and (B) contain the measurements of room-*T* prepared films, while (C) and (D) contain the measurements of high-*T* prepared films. (A) and (C) illustrate the fluorescence spectra of the films composed of Py/TBA+ (different anions): Py (black), Py/$TBAPF_6$ (red), Py/$TBANO_3$ (blue), Py/$TBABF_4$ (green), Py/TBACl (pink), and Py/ TBA acetate (light green), respectively; (B) and (D) illustrate the fluorescence spectra of the films composed of Py/PF_6^- (different cations): Py (black), Py/$TMAPF_6$ (red), Py/$TEAPF_6$ (blue), Py/$TBAPF_6$ (green), and Py/$THAPF_6$ (pink), respectively.

applied to the binary system, in the case of Py/$TBAPF_6$. However, high vapor pressure annealing under either acetone or THF does not change the Py excimer fluorescence (Fig.4. S3 in supporting information). The result suggests that PS serves an essential role as a plasticizer in presence of high solvent vapor pressure, providing the required mobility for the Py or salt molecules to reorganize themselves in a molecular configuration of the Py excimer. It should be noted that the solvation power of vapor phase is not equivalent to that in the solution state. We further annealed the high excimer

fluorescence Py/$TBAPF_6$ film (at 100 ^oC for 1h), which was made by solvent evaporation at high *T*, to investigate the effect of high thermal energy on quenching (Fig.4. S4 in supporting information). Unlike the ternary system where a nearly complete excimer quenching took place,[24] no significant change of Py excimer fluorescence intensity was observed in the binary system, indicating that the previous excimer fluorescence quenching in the Py/PS/$TBAPF_6$ film after 1-hour high-*T* annealing[24] was attributed to the enhanced mobility of Py and $TBAPF_6$ as associated with the highly mobile PS chains induced by high temperature (above the glass transition temperature of PS). However, in the Py/$TBAPF_6$ system, there is no mechanism for mobility enhancement in absence of PS chains.

–Hydrophobicity (I_1/I_3) and Excimer (I_{exc}/I_{mon})

Like the result in the solution state (Fig.4.2), the correlation of the hydrophobicity of Py surrounding with the Py excimer fluorescence is also studied in comparison of different salts in the solid state as shown in Fig.4. 4. Fig.4. 4 (A) illustrates the I_1/I_3 of several Py thin films containing TBA^+ salts with different anions prepared at different temperatures. Except for the $TBAPF_6$/Py film prepared at high *T*, all the other samples result in a more polar environment than Py itself judged by higher values of I_1/I_3 (> 1). Fig.4. 4 (B) shows the I_{exc}/I_{mon} for the same series of TBA^+ salts indicate low I_{exc}/I_{mon} (< 1) in most of the cases with the exceptions being the Py films and $TBAPF_6$/Py film made at high *T*. The correlation of the Py excimer emission with its hydrophobic environment is consistent with that observed

in the solution state (Fig.4. 2). Fig.4. 4(C) illustrates the I_1/I_3 of films made of Py and PF_6^- anion with various chain lengths of tetra-alkylammonium cations. The result also shows a general feature of hydrophobic environment for Py (i.e., $I_1/I_3 < 1$) in the PF_6^- films except for the Py/$TBAPF_6$ film prepared at room temperature. The same correlation of hydrophobicity with the formation of Py excimer is found in this series as shown in Fig.4. 4 (D), where the Py/$TBAPF_6$ film made at room temperature shows almost no excimer fluorescence.

Several findings deduced from the results are worth noting. First, both solution and solid state results seem to suggest that the polar environment of Py molecules may strongly correlate with the excimer fluorescence – the more hydrophobic, the higher the excimer fluorescence. It should be noted that in the previous ternary system (i.e., PS/Py/$TBAPF_6$ films) the hydrophobicity of Py environment is a required but not sufficient condition for high excimer fluorescence.[31] Examples of low I_1/I_3 but low I_{exc}/I_{mon} were occasionally found in the solution casting film made of PS/Py/$TBAPF_6$. Second, the result of Fig.4. 4 (A) ~ (D) suggests that the Py excimer quenching is mainly attributed to the TBA^+ cation instead of anion (PF_6^-, BF_4^-, Cl^-, $Acetate^-$, and NO_3^-) based on the high I_{exc}/I_{mon} observed in Py films containing tetraalkylammonium cations with other chain lengths (such as TMA^+, TEA^+ and THA^+).

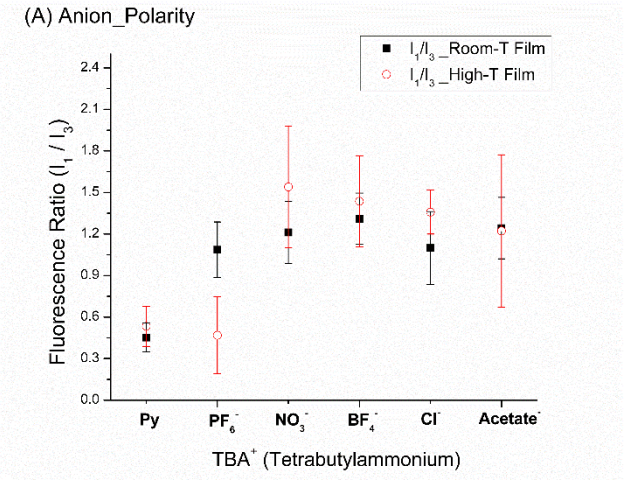
(A) Anion_Polarity
I1/I3 _Room-T Film
I1/I3 _High-T Film
Fluorescence Ratio (I1 / I3)
2.4
2.1
1.8
1.5
1.2
0.9
0.6
0.3
0.0
Py
PF6-
NO3-
BF4-
Cl-
Acetate-
TBA+ (Tetrabutylammonium)

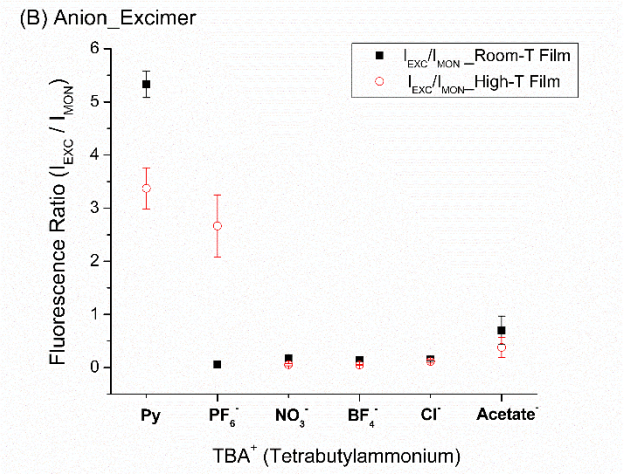
(B) Anion_Excimer
IEXC/IMON _Room-T Film
IEXC/IMON_High-T Film
Fluorescence Ratio (IEXC / IMON)
6
5
4
3
2
1
0
Py
PF6-
NO3-
BF4-
Cl-
Acetate-
TBA+ (Tetrabutylammonium)

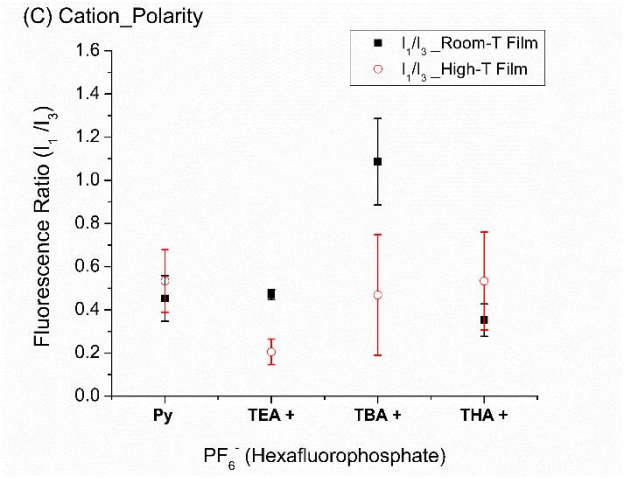
(C) Cation_Polarity
I1/I3 _Room-T Film
I1/I3 _High-T Film
Fluorescence Ratio (I1 /I3)
1.6
1.4
1.2
1.0
0.8
0.6
0.4
0.2
0.0
Py
TEA +
TBA +
THA +
PF6- (Hexafluorophosphate)

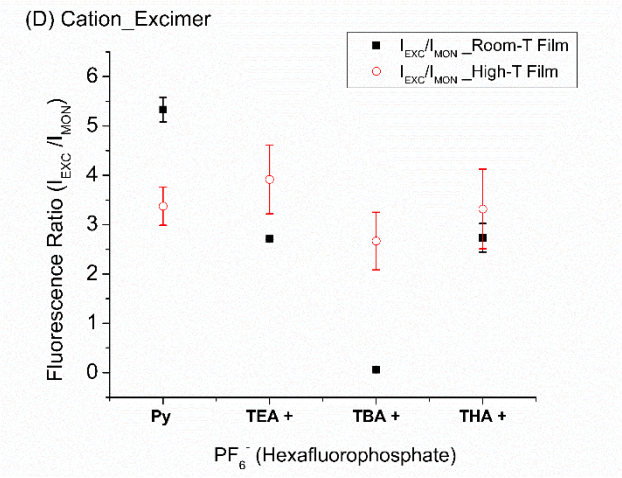

Fig.4. 4. Fluorescence intensity ratio of (A) I_1/I_3 (B) I_{exc}/I_{mon} of Py/TBA+ salt films prepared via Room-*T* (solid squares, black) and High-*T* (open circles, red) evaporation; (C) I_1/I_3 (D) I_{exc}/I_{mon} of Py/PF_6^- salt films prepared via Room-*T* (solid squares, black) and High-*T* (open circles, red) evaporation.

The unique quenching behavior induced by TBA^+ salts is possibly due to the perturbation of the molecular configuration of Py excimer[35, 38, 46] or the alternative non-radiative pathways. The detail of these scenarios will be discussed later. In regards to anions, PF_6^- does play a role in retaining high excimer fluorescence at high solvent vapor pressure (induced by high *T*) when the molecules are mobile enough, i.e., from solution to solid state. Other anions do not show such effect. Note that no clear correlation between I_{exc} and topology was observed in previous study in a three-component (Py/PS/$TBAPF_6$) system[31]. Here in order to examine the effect of the topology on hydrophobicity (I_1/I_3) of the Py surroundings, SEM was also conducted (Fig.4. S5). The result shows no significant difference in the

Py/$TBAPF_6$ films prepared at high and room *T* although they show very different I_{exc}/I_{mon} and I_1/I_3 values (Fig.4.3). Moreover, no significant difference in SEM data was observed in presence of different salts. This suggests that there is minimal relationship, if any, between topology and formation of Py excimer in the film.

– Interactions between Pyrene and Salts

The fact that a strong correlation is revealed between the polarity around Py and the formation of Py excimer prompts us to study the effect of $TBAPF_6$ on the Py local molecular environment. Fig.4. 5(A) shows the ^{13}C-NMR spectra of three thin films: a pure Py film and two Py/$TBAPF_6$ films prepared at a high and a room temperature which yield high and low I_{exc}/I_{mon}, respectively. It has been reported that Py has 5 peaks *in solution* in the

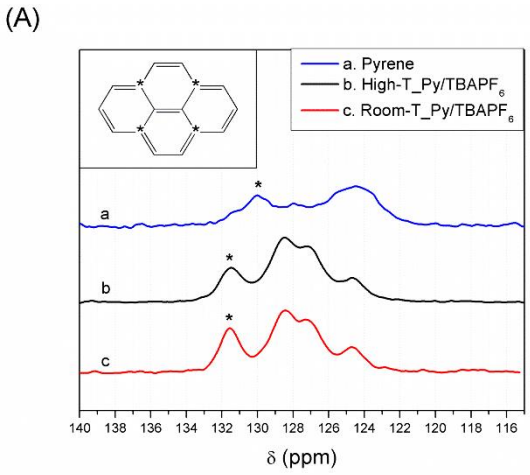

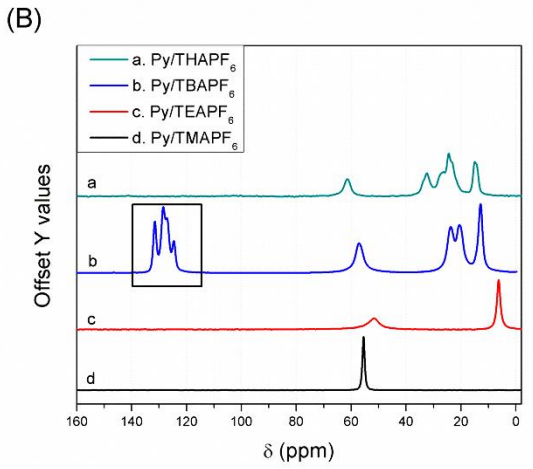

Fig.4. 5. ^{13}C-NMR spectra of (A) pure Py film (blue), Py/TBAPF$_6$ film prepared by high-*T* evaporation (black) and room-*T* evaporation (red), which is the blowup of the box in (B). The inset shows a pyrene molecule where the asterisks represent the carbons for the corresponding NMR shifts around 130 ~ 132 ppm. (B) Complete NMR spectra of Py/TMAPF$_6$ (black), Py/ TEAPF$_6$ (red), Py/TBAPF$_6$ (blue), and Py/THAPF$_6$ (green) films prepared by room-T evaporation.

spectra between 125 ~ 131 ppm (124.58 ppm, 124.81 ppm, 125.70 ppm, 127.25 ppm, 131.04 ppm, respectively[47]), while only three of them are resolvable in our case [Fig.4. 5(A)], possibly due to the lack of mobility in the solid state. Individual Py peaks are affected somewhat by TBAPF$_6$ to increase relative intensities of Py peaks. Another important finding in this study is that the peak at 130 ppm [marked as * in Fig.4. 5(A)] shifts to 131.6 ppm. This result is consistent with previous research[35] in that the interaction between polyaromatic hydrocarbon and quaternary alkylammonium group causes a NMR peak shift of several proton and C atoms. This is because the decrease in the symmetry of aromatic moiety possibly attributed to the

positively charged ammonium group polarizing the π-electrons of Py moiety.[35, 38-39] Fig.4. 5(B) shows the ^{13}C-NMR spectra of Py/PF_6 salts films, interestingly, the Py peaks around 125~ 132 ppm are only shown in Py/$TBAPF_6$ unlike other Py/salt films (i.e. Py/$TMAPF_6$, Py/$TEAPF_6$, Py/$THAPF_6$), indicating that Py interacts with $BAPF_6$ very differently from other salts. The ^{13}C-NMR peaks below 60 ppm in the Fig.4. 5(B) are contributed by tetraalkylammonium cations.

Then, the diminished Py peak in the ^{13}C-NMR (from 120 to 134 ppm) may be related to the reduced amount of Py monomers in the cases of Py/$TMAPF_6$, Py/$TEAPF_6$ and Py/$THAPF_6$. In this regard, it is speculated that the marginal differences between the ^{13}C-NMR spectra of the two Py/$TBAPF_6$ films prepared via room-*T* and high-*T* evaporation [Fig.4. 5(A)] is possibly due to the same local environment of Py monomer left with a specific molecular interaction regardless of existence of excimer. Besides NMR, XRD was also performed on the sample in order to investigate the correlations between crystalline structures of Py/salts films and the formation of Py excimer under different procedures. It should be noted that both Py and the associated salt contain crystalline structures yielding diffraction peaks. There is no significant change of crystalline structures observed in high-*T* and room-*T* prepared Py/$TBAPF_6$ films (Fig S6), while a significant difference in the I_{exc}/I_{mon} was observed (Fig.4.3), implicative of weak correlation between the crystal structures of Py/salts and excimer fluorescence.

-Lifetime of Py Excimer in Presence of $TBAPF_6$

Although the hydrophobicity of the environment where Py resides and the unique effect of $TBAPF_6$ on the Py excimer fluorescence are observed, the mechanism of Py excimer quenching requires further investigation. As mentioned previously, two possible mechanisms may take place: static quenching, where the quenchers (i.e., salt) and the fluorophores (i.e., Py) form non-fluorescent complexes; and dynamic quenching, where the fluorophores can still be excited to the same excited state but undergo an non-radiation pathways to relax from the excited to the ground state. As a result, the measured lifetime of the fluorophore (e.g., Py excimer in this case) will be the same for static quenching. However, in the case of dynamic quenching, shorter lifetime is expected since there are more non-radiative decay paths. The fluorescence decay was therefore measured to investigate the origin of Py excimer quenching mechanism by the TBA^+ salts.

The fluorescence lifetime of an excited fluorophore is inversely proportional to the sum of rate constants from all relaxation processes as expressed in Eq (1) [22].

$$\tau = \frac{1}{k} = \frac{1}{(k_f + k_{nr})} \quad (1)$$

where k, k_f, and k_{nr} are the sum of rate constants of all relaxation processes, rate of fluorescence, and the sum of rates of non-radiative processes (e.g., internal conversion and vibration relaxation, inter-molecular energy transfer, and inter-system crossing, etc.).

The fluorescence intensity decay can be described by the following equation:

$$\frac{I(t)}{I_{max}} = \sum_i A_i\, e^{-k_i t} = \sum_i A_i\, e^{-\frac{t}{\tau_i}} \qquad (2)$$

where $A_{i,}$ τ_i represent the fractions and lifetime of each relaxation process, respectively.

In this experiment, we focus on the lifetime of fluorescence with wavelengths above 450 nm from Py excimer. Fig.4. 6 (A) shows the excimer fluorescence decays of the Py and Py/$TBAPF_6$ in the solution state and the two decay curves practically collapse on top of each other, indicating that $TBAPF_6$ has no effect on Py excimer fluorescence in solution state, consistent with the steady-state fluorescence result shown in Table 2. In addition, all the other solutions containing Py/TBA salts (various anions) also yield the same decay pattern as that of Py solution further confirming the above statement (Fig.4. S7 in supporting information). In comparison with solution, the fluorescence intensity of Py excimer in the Py thin film decays much slower as shown in Fig.4. 6 (B), suggesting that the fluorescence lifetime of the Py excimer is shorter in solution state than that in solid state. The faster decay of lifetime in solution may be due to the increased frequency of collisions of Py excimers with surrounding solvent molecules and/or solvent dipole perturbation. It has been reported that the excited-state molecule can interact with the surrounding solvent molecules whose polarity may significantly affect the de-excitation of Py returning to

the ground state.[48] These excited-state solute/solvent interactions (i.e. dipole-induced dipole interaction between Py and solvent) often result in characteristic emission spectra as well as in the lifetime of the excited molecules.[48]

In Fig.4.6 (C), the high-*T* prepared Py/$TBAPF_6$ film appears a very similar decay pattern as that of the Py film, indicative of a similar decay mechanism. Though both decay curves of Py and high-*T* prepared Py/$TBAPF_6$ films can be described with a single exponential decay reasonably well, better fits are obtained by a double exponential decay with a major population (> 96.4%) of short-lifetime τ_1 of ~ 12 ns and a minor population (< 4.6%) of slightly different long-lifetimes τ_2, 31.8 and 41.6 ns for Py and Py/$TBAPF_6$, respectively (Table S1 in supporting information). This observation lends itself to a possible explanation that the majority of

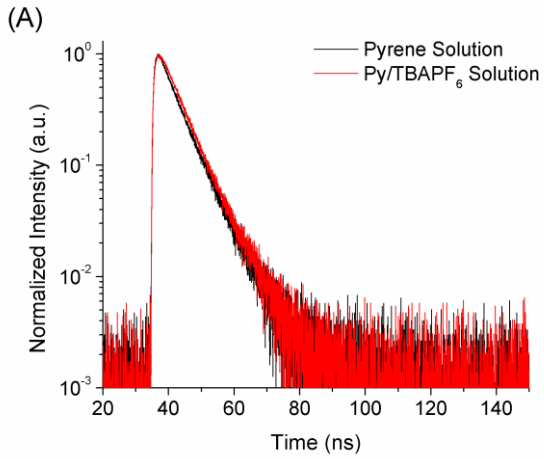

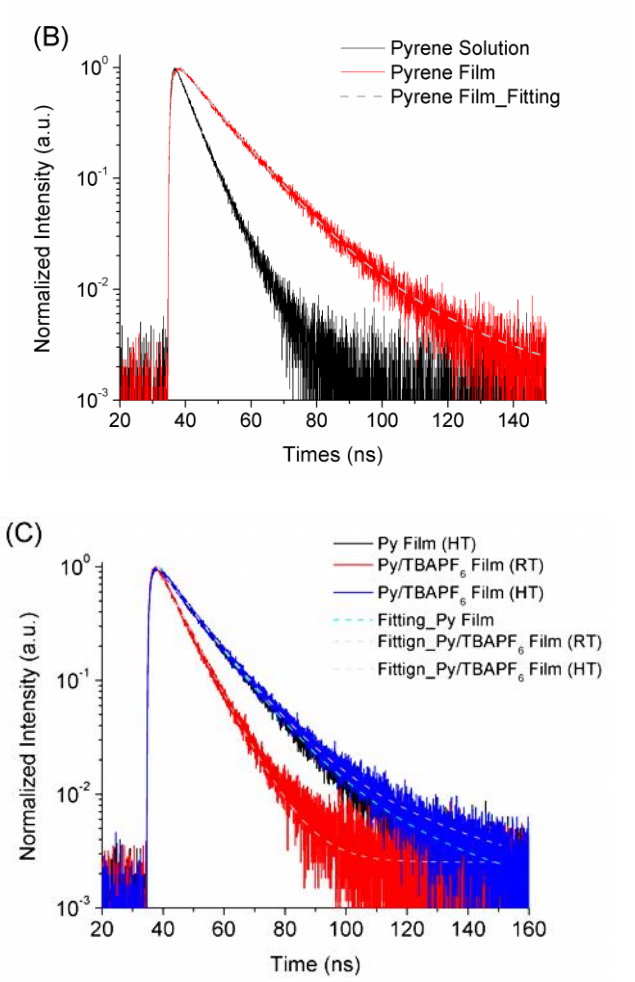

Fig.4. 6. Fluorescence lifetime measurements of (A) pure Py (black) and Py/$TBAPF_6$ (red) solutions, (B) pure Py solution (black) and film (red) and (C) Py film (black), room-*T* prepared Py/$TBAPF_6$ film(red), and high-*T* prepared Py/$TBAPF_6$ film (blue) The dotted lines are the best fits (see supporting information).

Py molecules in the high-*T* prepared Py/$TBAPF_6$ thin films follow a similar relaxation pathway compared with those in the Py film. It should be noted that the lifetime of Py thin film prepared at room-*T* shows the same decay rate as that of the high-*T* prepared film (data not shown) and that both films have the same excimer fluorescence (Fig.4. 3). In the case of a binary

system (i.e., Py/$TBAPF_6$), a drastic difference in the fluorescence is found between room-*T* and high-*T* prepared films. To further confirm the relationship between the excimer fluorescence intensity and its lifetime decay, the decay pattern of room-*T* prepared Py/$TBAPF_6$ film [Fig.4. 6(C) red curve] was also examined. The result can be fitted well by a single exponential decay with a much smaller τ_1 of 8.4 ns (Table S1 in supporting information). The shorter lifetime in room-*T* prepared Py/$TBAPF_6$ film compared with those of the Py and high-*T* Py/$TBAPF_6$ films (τ_1~ 12 ns) indicates a dynamic quenching process involving fast non-radiative pathways. An effort is also made to fit the decay through a linear combination of an independent single exponential decay and the double-exponential decay parameters obtained from the high-*T* prepared Py/$TBAPF_6$ data (Equations 4.S1 and 4.S2 in supporting information). However, the best fitting coefficient of the double-exponential decay is practically 0, providing the evidence that there is no contribution from the same decay mechanism found in the room-*T* prepared Py/$TBAPF_6$ film as that of the Py or high-*T* prepared Py/$TBAPF_6$ films (Table S1 in supporting information). Based on Eqs (1) and (2), the fast decay (i.e., smaller τ_1) in the room-*T* prepared Py/$TBAPF_6$ film is attributed to a larger k_{nr} than that of the high-*T* prepared Py/$TBAPF_6$ film if the intrinsic k_f remains constant.

- Further Insights to the Effect of $TBAPF_6$

Scheme 1 summarizes the observation of the formation of Py excimer in the presence of different chain lengths of quaternary ammonium salts and procedures.

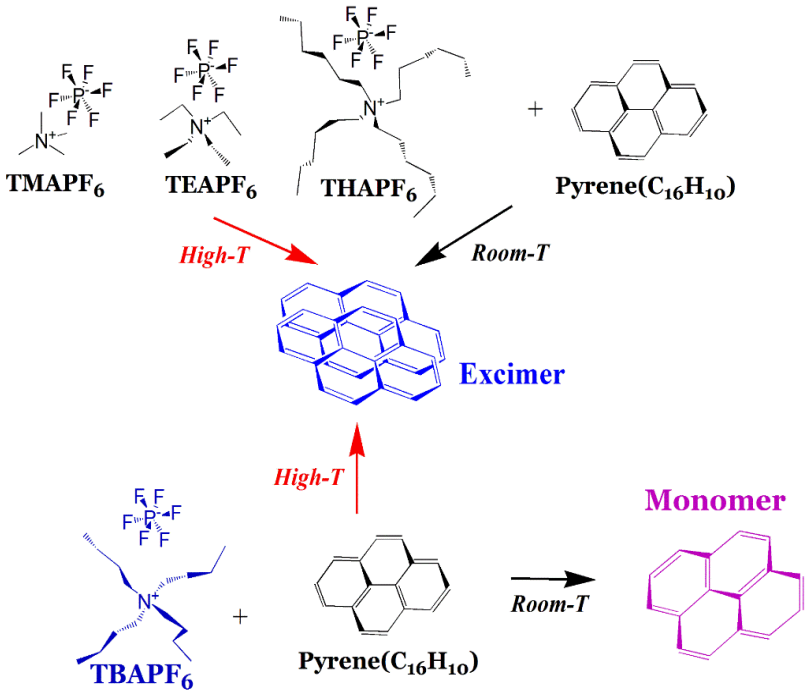

Scheme 4.1. The formation of Py excimer in the presence of different PF_6^- associated salts under a high-T or low-T thin-film preparation procedure.

The formation of Py excimer was only inhibited in the Py/$TBAPF_6$ thin film prepared at room T. Evidently the carbon chain length of the tetraalkylammonium is a key parameter of quenching. It has been reported that the proximity of Py molecules is an important factor in forming Py excimer (0.353~0.360 nm) with different configurations (i.e. slipped

parallel, graphite type, and crossed).[49] Note that the van der Waals size of tetraalkylammonium cation increases with increased carbon chain length: TMA^+ (0.270 nm) < TEA^+ (0.336 nm) < TBA^+ (0.413 nm) < THA^+ (0.442 nm).[50] When the cation size is smaller (e.g., TMA^+ and TEA^+), no apparent quenching effect on the excimer is revealed. As the cation size increases slightly larger than the intermolecular distance between Py molecules to form an excimer (in the case of TBA^+), the fluorescence quenching reaches its maximum. However, further increased size of the cation (e.g., THA^+) restores the fluorescence intensity. These facts suggest that *an optimal cation size may be required for the Py excimer quenching to perturb the molecular configuration of Py excimer*. The correlation between fluorescence and cation size offers a possible explanation, which may be further investigated by molecular dynamic simulations on the orientation and interactions of molecules on the orientation and interactions of molecules at a small length scale, e.g., Å. Moreover, the solvent can play an important role during the evaporation process when the Py excimer forms. It has been reported that ion association constant depends not only on the properties of the ions (ion radius and ion charge) but also on the nature of the solvent medium.[51] Based on Denison and Ramsey equation, the ion associations increase by the increase of temperature.[52] It is possible that an increased ion association between TBA^+ and PF_6^- during high-*T* evaporation (in presence of the solvent) provides a preferred configuration or environment to form Py excimers. The seemingly inconsistency of with

the invariance of ^{13}C-NMR spectra [Fig.4. 5(A)] and drastic difference in the excimer fluorescence and decay between high-*T* and room-*T* prepared samples can be reasoned by the speculation that the NMR peaks may arise from the Py monomer. In regards to the effect of anions on quenching mechanism, it has been known that PF_6^- has the largest size of 0.255 nm and the highest hydrophobicity among other anions in this study (i.e. Acetate, Cl^-, NO_3^-, BF_4^-).[53-55] Moreover, weak interaction between PF_6^- and solvent has also been reported.[51] The fact that PF_6^- is the only studied anion sensitive to the variation of temperature during evaporation process suggests that there might be a strong temperature dependence of either hydrophobicity or ionic interactions (with TBA^+ cation). To the best of our knowledge, this report presents the first observation of inhibited formation of Py excimer due to the different cation chain lengths of quaternary ammonium and the peculiar phenomenon of retaining excimer intensity (only in the case of $TBAPF_6$) of a high-*T* prepared film.

A previous report indicated that electrospun PS/Py/$TBAPF_6$ film was able to detect nitro-explosives with high selectivity and sensitivity through Py excimer quenching, providing a useful, low-cost platform for sensing[7]. Further investigation on the ternary system shows that the Py excimer can be also enhanced by an annealing process under high solvent (e.g., THF) vapor pressure[31]. Based on the results in the previous study and this work, several possible key physical parameters that might yield high sensitivity of the materials will be discussed as follows and they may be all required to

achieve the optimal performance. First, it is important to provide a flexible, aromatic matrix (e.g., PS) for Py molecules. The flexibility allows Py molecules to switch from excimer state to quenched state swiftly while it is not present in the current binary Py/$TBAPF_6$ films. The aromatic compound presumably induces certain alignment of Py so that the quenching might propagate throughout the material as reported previously[7]. Moreover, the configuration of Py may require being close to the transition from the excimer to quenched state, such that a small disturbance attributed by a trace amount of nitro-explosives may lead to the quenching of Py excimer as observed in the case of the electrospun (PS/Py) film containing $TBAPF_6$.[7] . Finally, high porosity (such as nanofibrous or nanoporous structure) can also be a determining factor for the probed molecules to access Py in a solid matrix, thus accelerating the excimer quenching process. The knowledge obtained in this study is readily applied to the molecular design of fluorescence sensors using Py or Py-derivatives.

4.4. Conclusion

The effect of different chemical structures of salts on the formation of Py excimer has been investigated in the solution state and solid state, respectively. In solution state, the Py concentration is mostly responsible for the formation and quenching of Py excimer with a marginal dependence of the salts since the process is mainly controlled by the diffusion of Py. On the contrary, the chemical structures of salts have a significant effect on the Py excimer quenching in solid state. The cation with butyl chain length

(TBA^+) results in significant quenching of the Py excimer, while methyl (TMA^+), ethyl (TEA^+), and hexyl (THA^+) chains have little or no effect on the Py excimer emission. The excimer fluorescence is found closely related to the polarity around the Py molecules, i.e., the higher I_1/I_3, the lower I_{exc}/I_{mon}. The result of the fluorescence lifetime measurement indicates that the low I_{exc}/I_{mon} in Py/$TBAPF_6$ films prepared at room *T* is mainly caused by non-radiative "dynamic quenching" processes. Moreover, the I_{exc}/I_{mon} of Py/$TBAPF_6$ film is greatly restored by high-*T* evaporation method, which however does not promote Py excimers with other anions in study. Such temperature dependence implies that the ion interaction or hydrophobicity between the PF_6^- anion and TBA^+ cation may change drastically upon variation of temperature during the drying process. Nevertheless, once the relative molecular orientation (or position) between Py and $TBAPF_6$ is "locked" in, thermal energy (up to 100 ^oC) indicates no effect on the fluorescence in solid state due to low molecular mobility (in contrast to the system containing PS). These peculiar effects of TBA^+ and PF_6^- on the Py excimer quenching are applicable for designing sensing materials using Py or Py-derivatives as fluorescence probes.

4.5. Supporting Information

Table 4.S1 illustrates the values of I_{exc}/I_{mon} and I_1/I_3 as a function of Py concentrations in acetone. The fact that I_{exc}/I_{mon} increases and I_1/I_3 decreases with increased Py concentration in all samples in Table 2 (similar to the

result shown in Fig. 2), indicates that the formation of the Py excimer has no significant dependence of salts. The critical Py concentration is found higher (~ 0.1 M) in the case of Py/THAPF$_6$ solution than the other solutions, possibly due to the increased size of salt, resulting in reduced mobility of Py.

Table 4.S1. The I_{exc}/I_{mon} and I_1/I_3 as a function of Py concentration in various Py/salt solutions.

Solution	Fluorescence Ratio	Pyrence Concentration (M)					
		0.0001	0.001	0.01	0.05	0.1	0.2
Py	I_1/I_3	1.49	1.49	1.30	0.23	0.06	0.14
	I_{exc}/I_{mon}	0.02	0.01	0.08	0.47	2.00	4.60
Py/TBA acetate	I_1/I_3	1.29	1.78	1.46	0.23	0.19	0.34
	I_{exc}/I_{mon}	0.25	0.02	0.07	0.62	1.92	4.99
Py/TBACl	I_1/I_3	1.37	1.55	1.21	0.17	0.08	0.28
	I_{exc}/I_{mon}	0.26	0.02	0.07	0.60	2.62	5.24
Py/TBANO$_3$	I_1/I_3	1.42	1.74	1.48	0.21	0.21	0.28
	I_{exc}/I_{mon}	0.25	0.02	0.06	0.63	2.26	4.61
Py/TBABF$_4$	I_1/I_3	1.46	1.74	1.50	0.16	0.22	0.31
	I_{exc}/I_{mon}	0.24	0.02	0.08	0.67	1.98	3.81
Py/TEAPF$_6$	I_1/I_3	1.65	1.77	1.45	0.21	0.12	0.37
	I_{exc}/I_{mon}	0.06	0.02	0.08	0.63	2.35	4.43
Py/TBAPF$_6$	I_1/I_3	1.69	1.77	1.47	0.26	0.13	0.15
	I_{exc}/I_{mon}	0.05	0.02	0.07	0.57	2.29	4.13
Py/THAPF$_6$	I_1/I_3	1.38	1.75	1.75	0.76	0.16	0.31
	I_{exc}/I_{mon}	0.27	0.04	0.02	0.29	0.88	2.87

The UV absorption spectra of Py and Py/salt solutions (in acetone) were measured using CARY 50 (UV-VIS spectrometer, Agilent). The scan rate is 600 nm/min, with 1 nm interval from 500 nm to 250 nm. The Py concentrations are 10^{-4}, 10^{-3}, 10^{-2}, 5×10^{-2}, 10^{-1}, and 2×10^{-1}M with a fixed weight ratio of salt-to-Py (71.2:28.8). Figure 4.S1 shows the UV-Abs spectra of all the samples. Due to the saturated Py concentration (as exceeding 0.05M) in the solution, broadened peak (or saturation from the enhanced concentration) was observed regardless of salts structure.

Fig. 4.S1. The UV absorption spectra of Py and Py/salt in acetone

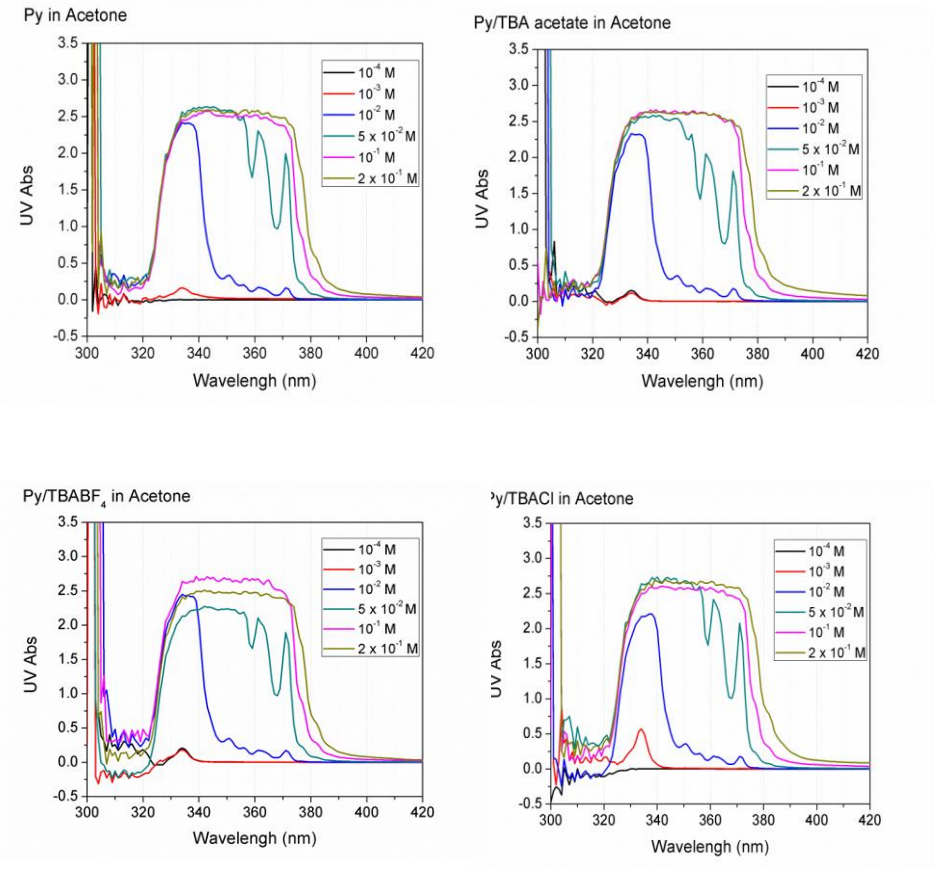

Also, red-shifted peak (above 0.05 M) may indicate that Py excimer is a type of J- aggregation.[56-58] The excitation wavelength for fluorescence experiment was also chosen based on the maximum absorption at low Py concentrations (~ 334 nm).

Fig. 4.S1. The UV absorption spectra of Py and Py/salt in acetone

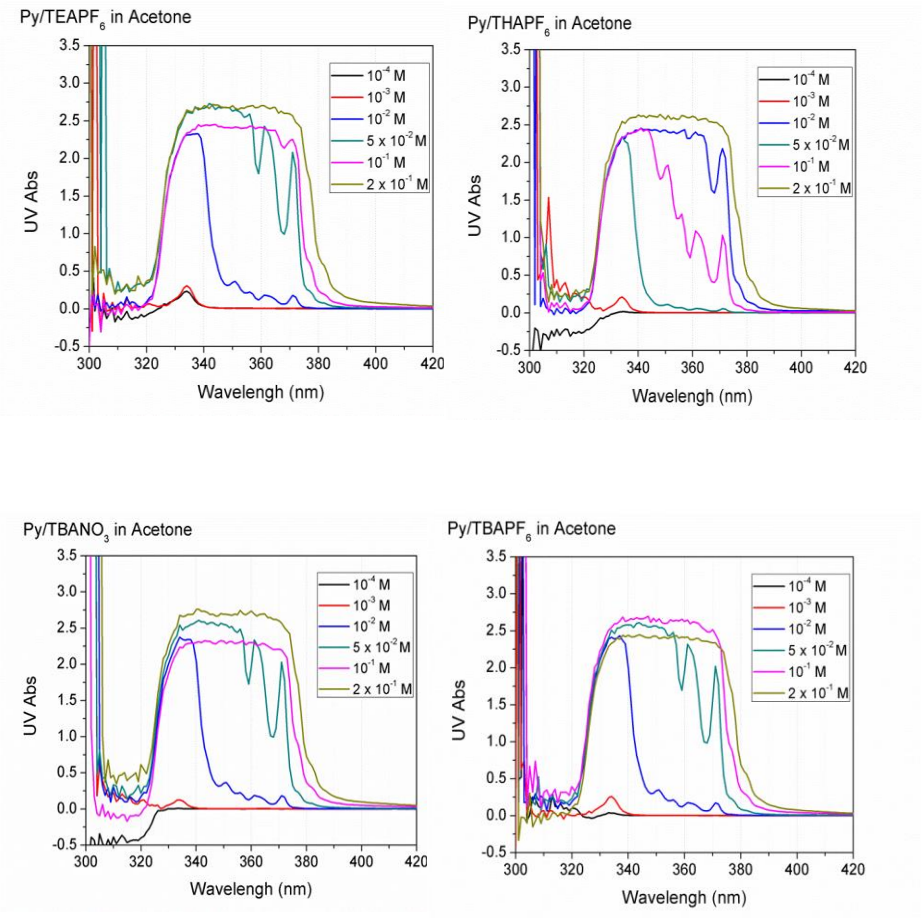

The I_{exc}/I_{mon} from the acetone solutions composed of Py and a series of salts as a function of salt concentration ranged from 0.25 to 1.5 M is shown in Fig.4.S2. All the fluorescence spectra were obtained at a constant Py concentration (0.01 M) as shown in Fig. S2. The result indicates a constant I_{exc}/I_{mon} value across almost all samples indicating that the formation of Py excimer is independent of salts and their concentrations in solution. The UV abs spectra of all the samples were also included in Fig.4.S2. Only marginal differences from each other were found.

Fig 4. S2. The I_{exc} / I_{mon} and UV-Abs spectra of Py/salt in solution at a constant Py concentration of 0.01 M.

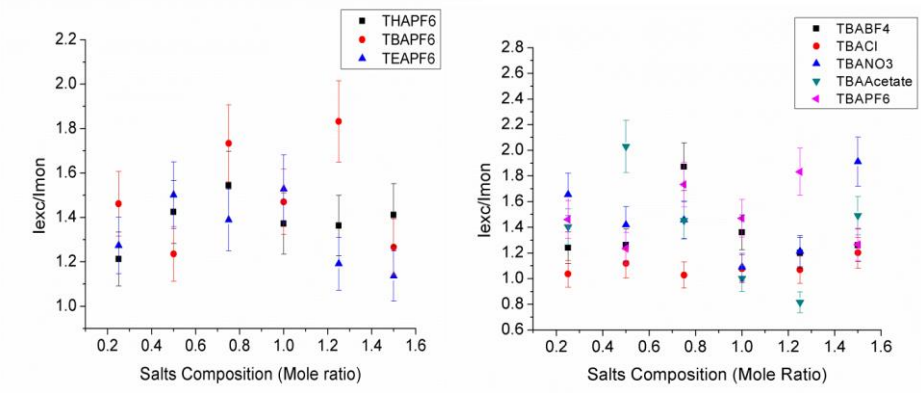

To understand the annealing effect of high solvent vapor pressure on the fluorescence of Py/salt film, a room-*T* prepared film (having low excimer emission) was annealed in a closed system containing 1 mL acetone and THF at 95 ^{o}C for 20 minutes. The solvents were not in contact with the film but evaporated into vapor to maintain high solvent vapor pressures. The vapor pressure of solvent, P_{solv} can be estimated using non-ideal equation of state: $P_{solv}V = Z_{solv}N_{solv}RT$, where V, Z_{solv}, N_{solv} and R are the volume of the container, compressibility factors, mole number of solvents and gas constant, respectively, Z_{solv} can be obtained using critical pressures and critical temperatures of the solvents. The calculated vapor pressures are 1251 mmHg and 1125 mmHg in the case of acetone and THF, respectively. Fig. 4.S3 shows the fluorescence emissions (in both cases of acetone and THF) of the annealed samples. In comparison to the pre-annealed samples, no difference was found indicating that annealing under high solvent vapor pressure did not restore the excimer emission. Note that the same procedure was able to restore the excimer fluorescence in the ternary mixture of PS/Py/$TBAPF_6$.

Fig 4.S3. The fluorescence emission spectra of Py/ $TBAPF_6$ film (black) prepared at room-*T* and after being annealed under (a) acetone and (b) THF vapor generated by 1 mL of the solvent in the closed system at 95 °C (red) for 20mins.

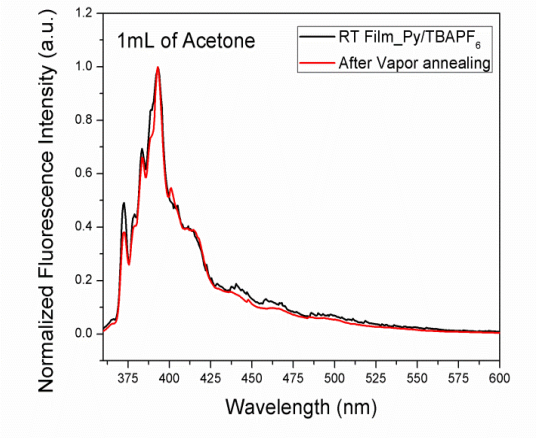

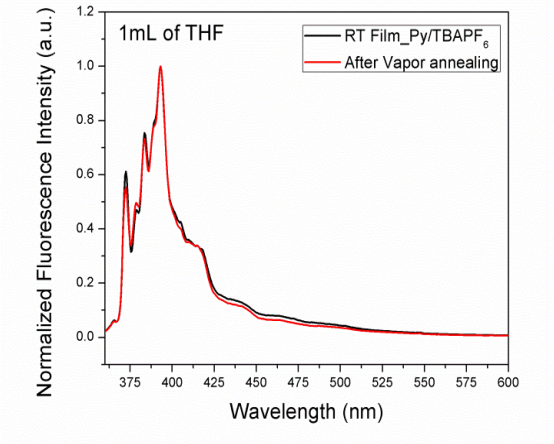

Previously it has been reported that the excimer fluorescencce of the high-*T* prepared ternary PS/Py/$TBAPF_6$ thin film (having high excimer emission) can be quenched after being annealed at 100 ^oC for 1 hour[31]. The change of Py excimer configuration is presumably attributed from the high mobility of Py as it is associated with PS matrix above the glass transition point. The same approach is taken to test the high-*T* (100 °C) prepared binary

Py/TBAPF$_6$ system, which also reveals a high excimer emission. Fig.4. S4 shows the fluorescence emission spectra of the high-*T* prepared thin film before and after being annealed at 100 °C for 1 h. No significant change in Py excimer fluorescence intensity was observed after high-*T* annealing, indicating no thermal effect on the Py excimers in the solid state. This result implies that the enhanced flexibility of Py provided PS (> T_G) is a key parameter to quench Py excimer.

Fig 4. S4. The fluorescence emission spectra of freshly prepared high-*T* (100 °C) Py/TBAPF$_6$ film and after being annealed at 100 °C for 1 h. No significant change in Py excimer fluorescence intensity was observed after high-*T* annealing, indicating that no thermal effect on the Py excimers in the solid state.

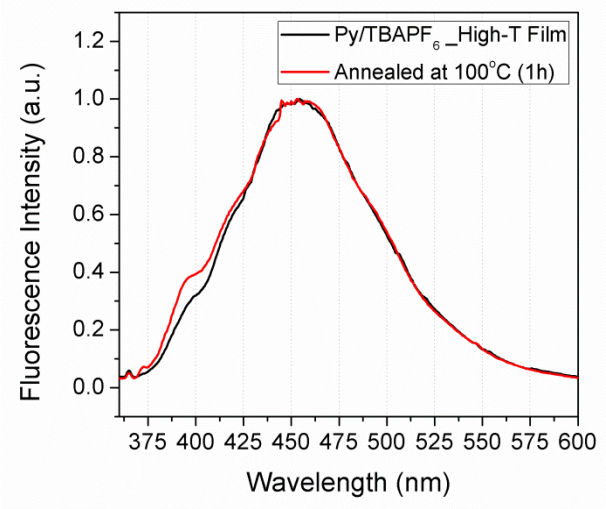

The topology of Py and Py/salt films was examined by SEM to correlate an aggregation of Py and it fluorescence response of I_{exc} in Fig.4S5. Note that a significant difference of I_{exc}/I_{mon} was observed in Py/$TBAPF_6$ films prepared by high-*T* and room-*T*, respectively in Fig 4..3. Also, salts structures provided a different polar environment to the Py as shown Fig. 4.3. (i.e., room-*T* prepared films of Py/ $TBABF_6$ and Py/$TBABF_4$ – hydrophilic; Py/$THAPF_6$ – hydrophobic) However, no clear difference was observed in the films made of Py and different salts as well as by different preparation methods, suggesting us that there is little or non-correlation between topology and formation of Py excimer in the film.

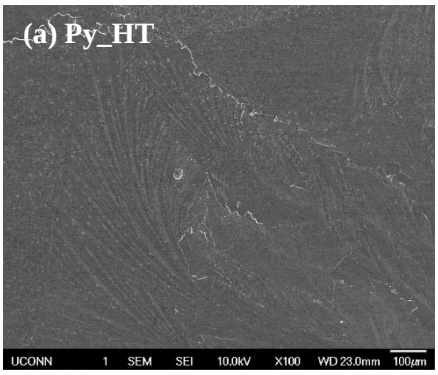

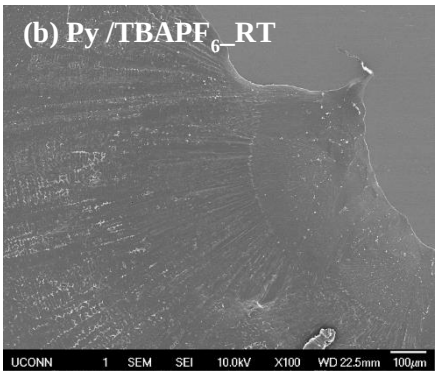

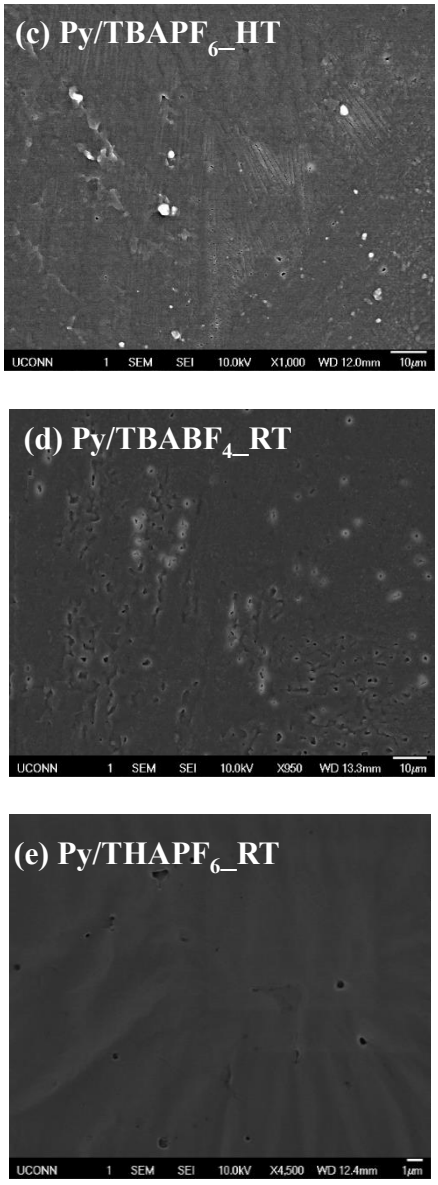

Fig 4. S5 The SEM images of films (a) *High-T* prepared Py (b) *Room-T* prepared Py/$TBAPF_6$ (c) *High-T* prepared Py/$TBAPF_6$ (d) *Room-T* prepared Py/$TBABF_4$ (e) *Room-T* prepared Py/$THAPF_6$

Fig.S6 shows the XRD results of $TBAPF_6$, high-T prepared Py/$TBAPF_6$, low-T prepared Py/$TBAPF_6$, Py films. The peak positions represent the lattice parameters. Nevertheless, no significant difference between the high-*T* and low- *T* prepared Py/$TBAPF_6$ films was found, while a significant different I_{exc}/I_{mon} was observed in the two cases, indicating a weak correlation between crystalline structures of Py/salts and Py excimer fluorescence.

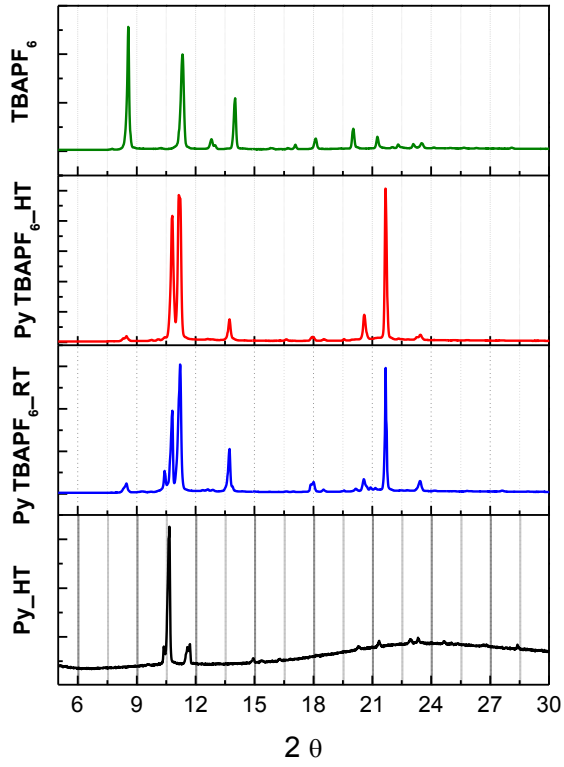

Fig 4.S6. The XRD spectra of different films (a) Py (black) (b) room-*T* prepared Py/ $TBAPF_6$ (blue) (c) high-*T* prepared Py/ $TBAPF_6$ (red) (d) $TBAPF_6$ (green).

The lifetime of excimer in Py/salt solutions was also studied to provide the insight to the effect of the salts in this study on the formation of Py excimer. Fig. S7 shows practically the same decay for all the cases, a confirmation of marginal effects of cation or anion structure on the Py excimer quenching mechanism.

Fig 4. S7. Fluorescence lifetime of solution (A) Py/TBA acetate (black), Py/$TEAPF_6$ (red), Py/$THAPF_6$ (blue) , Py/$TBABF_4$ (marine), Py/$TBANO_3$ (pink), Py (dark green), and Py/$TBAPF_6$ (dark blue).

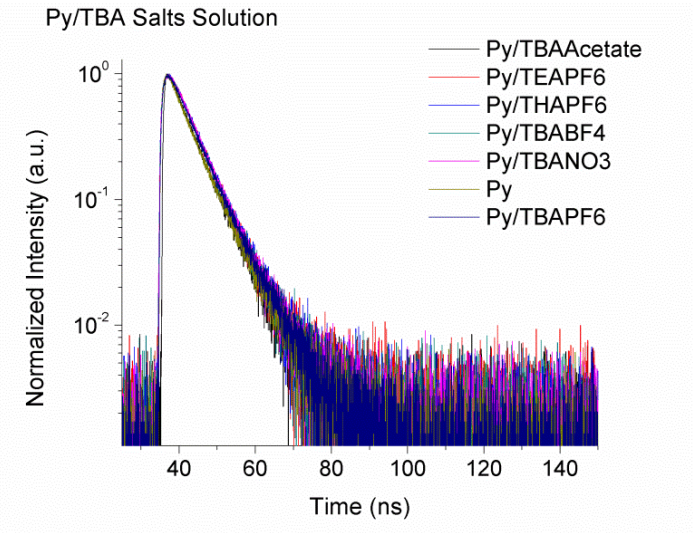

The double-exponential and combinational decay functions [as shown in Eqs. (S1) and (S2)] were used to best fit the data of excimer lifetime obtained from high-*T* prepared Py/$TBAPF_6$ (or pure Py) films and room-*T* prepared Py/$TBAPF_6$ film, respectively. In the double-exponential decay, two relaxation modes are assumed having the populations of A_1 and A_2, and the relaxation times of τ_1 and τ_2, respectively. The excitation laser pulse came in at time t_o. It should be noted that in the case of combinational decay function (used for the room-*T* prepared Py/$TBAPF_6$ film) A_1 and A_2 are kept unchanged and only a prefactor *B* is used to account for the population of the same decay mechanism presented by the high-*T* prepared Py/$TBAPF_6$ residue. The lifetime of the new single-exponential decay constant, τ'_1 and the prefactor, A_3 (presenting its population) as well as *B* and t_o are obtained through best fitting the experimental data of the room-*T* prepared Py/$TBAPF_6$ film using Eq (S2).

$$I_{HT}\ or\ I_{Py}\ (t) = A_1 e^{-\frac{t-t_0}{\tau_1}} + A_2 e^{-\frac{t-t_0}{\tau_2}} \quad \text{(S1)}$$

$$I_{RT}(t) = A_3 e^{-\frac{t-t_0}{\tau'_1}} + B(A_1 e^{-\frac{t-t_0}{\tau_1}} + A_2 e^{-\frac{t-t_0}{\tau_2}}) \quad \text{(S2)}$$

The best fitting parameters in the cases are summarized in Table 4 S2.

Table 4.S2. The best fitting parameters for double-exponential and combinational decay functions to describe the excimer lifetimes of Py, high-*T* prepared Py/$TBAPF_6$ and room-*T* prepared Py/$TBAPF_6$ films.

(1) Double-exponential decay function

	t_o (ns)	A_1	τ_1(ns)	A_2	τ_2 (ns)
Py film	38.4	0.964	11.9	0.046	31.8
HT, Py/$TBAPF_6$ film	38.0	0.987	12.3	0.036	41.6

(2) Combinational decay function

	t_o (ns)	A_3	τ'_1(ns)	B
RT, Py/$TBAPF_6$ film	37.9	1.00	8.4	0.00

References

1. Bohn, P. W. *Annu. Rev. Phys. Chem.* **1993,** *44*, 37-60.
2. Harrison, W. J.; Mateer, D. L.; Tiddy, G. J. T. *J. Phys. Chem.* **1996,** *100*, 2310-2321.
3. Würthner, F.; Thalacker, C.; Diele, S.; Tschierske, C. *Chem. Eur. J.* **2001,** *7*, 2245-2253.
4. Jang, H.-S.; Wang, Y.; Lei, Y.; Nieh, M.-P. *J. Phys. Chem. C* **2012,** *117*, 1428-1435.

4.6. References

1. Birks, J. B., Excimers. *Reports on Progress in Physics* **1975,** *38* (8), 903.

2. Santos-Figueroa, L. E.; Moragues, M. E.; Climent, E.; Agostini, A.; Martinez-Manez, R.; Sancenon, F., Chromogenic and fluorogenic chemosensors and reagents for anions. A comprehensive review of the years 2010-2011. *Chemical Society Reviews* **2013,** *42* (8), 3489-3613.

3. Xu, Z.; Singh, N. J.; Lim, J.; Pan, J.; Kim, H. N.; Park, S.; Kim, K. S.; Yoon, J., Unique Sandwich Stacking of Pyrene-Adenine-Pyrene for Selective and Ratiometric Fluorescent Sensing of ATP at Physiological pH. *Journal of the American Chemical Society* **2009,** *131* (42), 15528-15533.

4. Kim, S. K.; Bok, J. H.; Bartsch, R. A.; Lee, J. Y.; Kim, J. S., A Fluoride-Selective PCT Chemosensor Based on Formation of a Static Pyrene Excimer. *Organic Letters* **2005,** *7* (22), 4839-4842.

5. Kim, H. N.; Ren, W. X.; Kim, J. S.; Yoon, J., Fluorescent and colorimetric sensors for detection of lead, cadmium, and mercury ions. *Chemical Society Reviews* **2012,** *41* (8), 3210-3244.

6. Veale, E. B.; Gunnlaugsson, T., Fluorescent sensors for ions based on organic structures. *Annual Reports Section "B" (Organic Chemistry)* **2010,** *106* (0), 376-406.

7. Wang, Y.; La, A.; Ding, Y.; Liu, Y.; Lei, Y., Novel Signal-Amplifying Fluorescent Nanofibers for Naked-Eye-Based Ultrasensitive Detection of Buried Explosives and Explosive Vapors. *Advanced Functional Materials* **2012,** *22* (17), 3547-3555.

8. Hong, Y.; Lam, J. W.; Tang, B. Z., Aggregation-induced emission: phenomenon, mechanism and applications. *Chemical communications* **2009,** (29), 4332-53.

9. Salinas, Y.; Martinez-Manez, R.; Marcos, M. D.; Sancenon, F.; Costero, A. M.; Parra, M.; Gil, S., Optical chemosensors and reagents to detect explosives. *Chemical Society Reviews* **2012,** *41* (3), 1261-1296.

10. Focsaneanu, K. S.; Scaiano, J. C., Potential analytical applications of differential fluorescence quenching: pyrene monomer and excimer emissions as sensors for electron deficient molecules. *Photochemical & Photobiological Sciences* **2005,** *4* (10), 817-821.

11. Bittermann, H.; Siegemund, D.; Malinovskii, V. L.; Häner, R., Dialkynylpyrenes: Strongly Fluorescent, Environment-Sensitive DNA Building Blocks. *Journal of the American Chemical Society* **2008,** *130* (46), 15285-15287.

12. Uno, S.; Dohno, C.; Bittermann, H.; Malinovskii, V. L.; Haner, R.; Nakatani, K., A Light-Driven Supramolecular Optical Switch. *Angew Chem Int Edit* **2009,** *48* (40), 7362-7365.

13. Geddes, C. D. L., J. R., *Advanced Concepts in Fluorescence Sensing*. Springer, Norwell: **2005**.

14. Kalyanasundaram, K., Photophysics of molecules in micelle-forming surfactant solutions. *Chemical Society Reviews* **1978,** *7* (4), 453-472.

15. Tan, W. H.; Wang, K. M.; Drake, T. J., Molecular beacons. *Curr Opin Chem Biol* **2004,** *8* (5), 547-553.

16. Fujimoto, K.; Shimizu, H.; Inouye, M., Unambiguous Detection of Target DNAs by Excimer−Monomer Switching Molecular Beacons. *The Journal of Organic Chemistry* **2004,** *69* (10), 3271-3275.

17. Conlon, P.; Yang, C. Y. J.; Wu, Y. R.; Chen, Y.; Martinez, K.; Kim, Y. M.; Stevens, N.; Marti, A. A.; Jockusch, S.; Turro, N. J.; Tan, W. H., Pyrene excimer signaling molecular beacons for probing nucleic acids. *Journal of the American Chemical Society* **2008,** *130* (1), 336-342.

18. Ostergaard, M. E.; Hrdlicka, P. J., Pyrene-functionalized oligonucleotides and locked nucleic acids (LNAs): Tools for fundamental research, diagnostics, and nanotechnology. *Chemical Society Reviews* **2011,** *40* (12), 5771-5788.

19. Inouye, M.; Fujimoto, K.; Furusyo, M.; Nakazumi, H., Molecular Recognition Abilities of a New Class of Water-Soluble Cyclophanes

Capable of Encompassing a Neutral Cavity. *Journal of the American Chemical Society* **1999,** *121* (7), 1452-1458.

20. Winnik, F. M., Photophysics of preassociated pyrenes in aqueous polymer solutions and in other organized media. *Chemical Reviews* **1993,** *93* (2), 587-614.

21. Winnik, M. A., End-to-end cyclization of polymer chains. *Accounts of Chemical Research* **1985,** *18* (3), 73-79.

22. Birks, J. B., *Photophysics of Aromatic Molecules*. Wiley: London, **1970**.

23. Seo, Y. J.; Hwang, G. T.; Kim, B. H., Quencher-free molecular beacon systems with two pyrene units in the stem region. *Tetrahedron Lett* **2006,** *47* (24), 4037-4039.

24. Trkulja, I.; Biner, S. M.; Langenegger, S. M.; Haner, R., A molecular probe for the detection of homopurine sequences. *Chembiochem* **2007,** *8* (1), 25-27.

25. Wilson, J. N.; Teo, Y. N.; Kool, E. T., Efficient quenching of oligomeric fluorophores on a DNA backbone. *Journal of the American Chemical Society* **2007,** *129* (50), 15426-+.

26. Birks, J. B.; Christophorou, L. G., Excimer fluorescence spectra of pyrene derivatives. *Spectrochimica Acta* **1963,** *19* (2), 401-410.

27. Kalyanasundaram, K.; Thomas, J. K., Environmental effects on vibronic band intensities in pyrene monomer fluorescence and their application in studies of micellar systems. *Journal of the American Chemical Society* **1977,** *99* (7), 2039-2044.

28. Seko, T.; Ogura, K.; Kawakami, Y.; Sugino, H.; Toyotama, H.; Tanaka, J., Excimer emission of anthracene, perylene, coronene and pyrene microcrystals dispersed in water. *Chemical Physics Letters* **1998,** *291* (3–4), 438-444.

29. Romashko, T. P.; Khakhel, O. A., Spectral criterion of the state of thermodynamic equilibrium of molecular excimers. *Journal of Applied Spectroscopy* **2003,** *70* (4), 509-512.

30. Nautiyal, A.; Bisht, P. B., Steady state and time-resolved studies of pyrene in solution and in single microcrystals. *Journal of Luminescence* **2010,** *130* (10), 1829-1833.

31. Jang, H.-S.; Wang, Y.; Lei, Y.; Nieh, M.-P., Controllable Formation of Pyrene (C16H10) Excimers in Polystyrene/Tetrabutylammonium Hexafluorophosphate Films through Solvent Vapor and Temperature Annealing. *The Journal of Physical Chemistry C* **2012,** *117* (3), 1428-1435.

32. Yan, D.; Delori, A.; Lloyd, G. O.; Friščić, T.; Day, G. M.; Jones, W.; Lu, J.; Wei, M.; Evans, D. G.; Duan, X., A Cocrystal Strategy to Tune the Luminescent Properties of Stilbene-Type Organic Solid-State Materials. *Angewandte Chemie International Edition* **2011,** *50* (52), 12483-12486.

33. Yan, D.; Williams, G. R.; Zhao, M.; Li, C.; Fan, G.; Yang, H., Flexible Free-Standing Luminescent Two-Component Fiber Films with Tunable Hierarchical Structures Based on Hydrogen-Bonding Architecture. *Langmuir* **2013,** *29* (50), 15673-15681.

34. Hartley, R. J.; Faulkner, L. R., QUENCHING AND POSSIBLE COULOMBIC COMPLEXATION OF THE PYRENE-N,N-DIMETHYLANILINE EXCIPLEX BY TETRAALKYLAMMONIUM SALTS. *Journal of the American Chemical Society* **1985,** *107* (12), 3436-3442.

35. Viaene, K.; Verbeeck, A.; Gelade, E.; De Schryver, F. C., Study of the interaction between arenes and tetraalkylammonium compounds in homogeneous and micellar solutions. *Langmuir* **1986,** *2* (4), 456-460.

36. Bauer, R. K.; Borenstein, R.; De Mayo, P.; Okada, K.; Rafalska, M.; Ware, W. R.; Wu, K. C., Surface photochemistry: translational motion of organic molecules adsorbed on silica gel and its consequences. *Journal of the American Chemical Society* **1982,** *104* (17), 4635-4644.

37. Li, D.; Song, J.; Yin, P.; Simotwo, S.; Bassler, A. J.; Aung, Y.; Roberts, J. E.; Hardcastle, K. I.; Hill, C. L.; Liu, T., Inorganic–Organic Hybrid Vesicles with Counterion- and pH-Controlled Fluorescent Properties. *J. Am. Chem. Soc.* **2011,** *133* (35), 14010-14016.

38. Lianos, P.; Viriot, M. L.; Zana, R., Study of the solubilization of aromatic hydrocarbons by aqueous micellar solutions. *The Journal of Physical Chemistry* **1984,** *88* (6), 1098-1101.

39. Almgren, M.; Medhage, B.; Mukhtar, E., Fluorescence study of the weak interaction between pyrene and quaternary ammonium groups. *Journal of Photochemistry and Photobiology A: Chemistry* **1991,** *59* (3), 323-334.

40. Pansu, R. B.; Yoshihara, K.; Arai, T.; Tokumaru, K., Convolution analysis of the pyrene excimer formation in membranes. *The Journal of Physical Chemistry* **1993,** *97* (6), 1125-1133.

41. Lochmuller, C. H.; Hunnicutt, M. L., Solvent-induced conformational changes on chemically modified silica surfaces. *The Journal of Physical Chemistry* **1986,** *90* (18), 4318-4322.

42. Glushko, V.; Thaler, M. S. R.; Karp, C. D., Pyrene fluorescence fine structure as a polarity probe of hydrophobic regions: Behavior in model solvents. *Archives of Biochemistry and Biophysics* **1981,** *210* (1), 33-42.

43. Ndou, T. T.; von Wandruszka, R., Pyrene fluorescence in premicellar solutions: The effects of solvents and temperature. *Journal of Luminescence* **1990,** *46* (1), 33-38.

44. Chen, S. H.; Mcguffin, V. L., Temperature Effect on Pyrene as a Polarity Probe for Supercritical-Fluid and Liquid Solutions. *Appl Spectrosc* **1994,** *48* (5), 596-603.

45. Suib, S. L.; Kostapapas, A., Intermolecular pyrene excimer formation in zeolites. Decay parameters and ground-state association. *Journal of the American Chemical Society* **1984,** *106* (25), 7705-7710.

46. Nakajima, A., Solvent Effect on the Vibrational Structures of the Fluorescence and Absorption Spectra of Pyrene. *Bulletin of the Chemical Society of Japan* **1971,** *44* (12), 3272-3277.

47. (SDBS), S. D. f. O. C. http://sdbs.riodb.aist.go.jp/sdbs/cgi-bin/direct_frame_top.cgi.

48. Reichardt, C., *Solvents and Solvent Effects in Organic Chemistry*. Wiley: **2006**.

49. Podeszwa, R.; Szalewicz, K., Physical origins of interactions in dimers of polycyclic aromatic hydrocarbons. *Physical Chemistry Chemical Physics* **2008,** *10* (19), 2735-2746.

50. Marcus, Y., Tetraalkylammonium Ions in Aqueous and Non-aqueous Solutions. *J Solution Chem* **2008,** *37* (8), 1071-1098.

51. Tsierkezos, N. G.; Philippopoulos, A. I., Studies of ion solvation and ion association of n-tetrabutylammonium hexafluorophosphate and n-tetrabutylammonium tetraphenylborate in various solvents. *Fluid Phase Equilibria* **2009,** *277* (1), 20-28.

52. Denison, J. T.; Ramsey, J. B., The Free Energy, Enthalpy and Entropy of Dissociation of Some Perchlorates in Ethylene Chloride and Ethylidene Chloride. *Journal of the American Chemical Society* **1955,** *77* (9), 2615-2621.

53. Chen, S.; Pei, R., Ion-Induced Rectification of Nanoparticle Quantized Capacitance Charging in Aqueous Solutions. *Journal of the American Chemical Society* **2001,** *123* (43), 10607-10615.

54. Jenkins, H. D. B.; Thakur, K. P., Reappraisal of thermochemical radii for complex ions. *Journal of Chemical Education* **1979,** *56* (9), 576.

55. Matsushita, N.; Kitagawa, H.; Mitani, T., Counter-ion radius dependence of the mixed-valence state in MX chain platinum complexes. *Synthetic Metals* **1995,** *71* (1–3), 1933-1934.

56. Bohn, P. W., Aspects of Structure and Energy Transport in Artificial Molecular Assemblies. *Annual Review of Physical Chemistry* **1993,** *44* (1), 37-60.

57. Harrison, W. J.; Mateer, D. L.; Tiddy, G. J. T., Liquid-Crystalline J-Aggregates Formed by Aqueous Ionic Cyanine Dyes. *The Journal of Physical Chemistry* **1996,** *100* (6), 2310-2321.

58. Würthner, F.; Thalacker, C.; Diele, S.; Tschierske, C., Fluorescent J-type Aggregates and Thermotropic Columnar Mesophases of Perylene Bisimide Dyes. *Chemistry – A European Journal* **2001,** *7* (10), 2245-2253.

Chapter 5.

High Efficiency Pyrene/Polystyrene Thin Films for Nitroaromatic-Explosives Detection – The Effects of Polymer Molecular Weights, Architectures and Diffusion of Explosive Molecules

5.1. Introduction

Nitroaromatic compounds can be employed as explosives which provide a useful tool to remove obstacles in construction. However, these materials can also be used by terrorists to threaten the public safety. A fast and accurate method to detect explosives is therefore important to reduce the financial burden due to time loss, personnel training and expensive advanced analytic equipment or materials. These explosives are usually good electron acceptors because of the electron withdrawing nitro groups.[1-2] The common challenge for detecting solid explosives arises from their low vapor pressure (normally in the sub-ppm range). One of the most effective materials in sensing the nitroaromatics explosives is a fluorescent conjugated polymer, poly(phenylenethynylene) (PPE), which promotes the exciton migration along the polymer backbone resulting in fluorescence quenching over a long range by a single quencher-binding, known as "molecular wire" amplification.[3] This material was able to detect the trace

amount of 10–100 femtograms level of trinitrotoluene (TNT). The superior performance is attributed to efficient electron delocalization and exciton migration.[3-4] Recently, it has also been reported that the fluorescence of electrospun films composed of three common species, i.e., a fluorophore (pyrene, Py), a non-conductive polymer (polystyrene, PS), and a salt (Tetrabutylammonium Hexafluorophosphate, $TBAPF_6$) can be effectively quenched in presence of a trace amount (at a ppb level) of nitro-explosives (e.g., nitro-aromatic, nitro-glycerin, or nitro-amine compounds) over a short period of time (in 6 minutes).[5] This mechanism provides an ideal sensing platform for explosives. The fact that these materials are readily available and do not require complicated synthesis and manufacturing processes enables the efficient and economic explosive detection without compromising the sensitivity and selectivity. A recent report showed that the Py excimer fluorescence in a PS/Py/$TBAPF_6$ film are tunable by the solvent vapor pressure, which provides a mean to control the formation of Py excimers.[6] The effect of a variety of salts on the fluorescence has also been studied in Py/salt mixtures. A unique dependence of quenching effect was found in certain anion and specific cation with 4-carbon chain length (i.e., TBA^+).[7]

It has known that fluorescence quenching by analytes relies on not only the electronic interaction but also the structural variation of the sensing molecule (i.e., Py in this case) in the matrix and its interaction with the analyte. Therefore, the structure of the polymer matrix, where Py resides, is

expected to be important. It has been reported that PS provides the best environment in order to yield fast quenching of Py by 2,4-dinitrotouelene (2,4-DNT) compared with other polymers (e..g, polyethylene oxide, polyacrylonitrile, polyvinylpyrrolidone), presumably due to the phenyl group of PS[5]. However, whether the quenching of Py propagates along the backbone (similar to the "molecular wire"[3]) and whether the molecular weight of PS will affect the quenching remain unclear. It is anticipated that the quenching rate of Py would decrease for shorter PS chains if the quenching of Py is along the polymer backbone. In this paper, we will investigate the quenching efficiency in correlation with the variations of the molecular weight of PS and the film thickness to provide the insight to this issue.

Moreover, different polymer architectures are also investigated in order to probe new structure-property relationship such as the quenching dependence of Py (by 2,4 DNT) on the electron energy level. Graft PS polymers with branches have been synthesized in different structures (e.g., "centipede-like", and "4-arm star").[8] The quenching efficiencies of Py by 2,4-DNT as Py resides in such PS hosts are also evaluated in comparison with that in the linear PS matrix of a similar molecular weight.

This paper will present the dependences of chain length (i.e. molecular weight) and molecular architecture of PS on the quenching efficiency of Py excimer. Fundamental understanding of the quenching mechanism, diffusion of 2,4-DNT in solid thin films, and key parameters which control

the quenching rate will also be studied and discussed, in order to design better sensing materials for nitro-explosives.

5.2 Experimental

Materials: The PS of different MWs (i.e., 2.5K 35K, 192K, 350K, and 900K), Py (MW = 202.15g/mol), $TBAPF_6$ (Tetrabutylammonium hexafluorophosphate), 2,4-DNT (2,4-ditnitrotoluene), and Tetrahydrofuran (THF) were all purchased from the Sigma-Aldrich and used without further purification.

Synthesis of different PS architectures: The different architectures of PS (i.e., linear, centipede, and 4-arm star) as shown in Fig. 5. 1 was synthesized via anionic polymerization of styrene[9-11]. Benzene, hexanes, styrene, butadiene, $SiCl_4$, $(CH_3)SiCl_3$, $(CH_3)_2SiCl_2$ and methanol were obtained from Aldrich and purified by using established methods. Sec-BuLi was synthesized from sec-BuCl and Li. 4-dichloromethylsilylstyrene (DCMSS) was synthesized from 4-chloromethylstyrene, by transformation first into a Grignard reagent and subsequent addition to $(CH_3)SiCl_3$.[12-14] Linear PS was synthesized simply from polymerization of styrene from sec-BuLi in benzene. 4-arm star PS was synthesized by (1) preparing PSLi, end-capping it with a few units of butadiene to reduce steric burdens, (2) linking these macro-anions with $SiCl_4$ in slight stoichiometric want, and (3) fractionating in toluene/methanol. Centipede PS was synthesized by (1) preparing PSLi and end-capping with butadiene, (2) preparing a doubly PS-grafted styrenic

macromonomer, in-situ, by adding this macroanion to DCMSS incrementally up to the twofold-equivalence point, and (3) polymerizing fresh styrene from sec-BuLi in the presence of this macromonomer. The 4-arm star PS possess ~1200 styryl units per arm of the star, and the case of centipede PS has arms of ~270 styryl units which are spaced out in a similar length scale. The molecular weight (MW) values of different PS materials were measured by SEC-LS and all have the MW range of500kg/mol shown in Table 5. 1.

SAMPLE	SEC-RI		SEC-LS	Averaged Number of Branch / Chain
	PDI	MW (kg/mol)	MW (kg/mol)	
LINEAR	1.05	575	486	0
4-ARM STAR	1.03	–	483	-
(arm for star)	1.03	130	125	3.9 arms per star
CENTIPEDE	1.07	–	540	-
(arm for centipede)	1.03	29.7	28.1	4.5 branches per centipede

Table 5.1. Molecular Characteristics of PS Samples

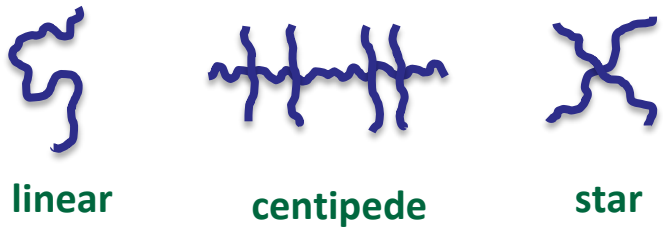

Figure 5.1. The different architectures of PS synthesized by anionic polymerization

Film preparation: The thickness of the PS/Py film made by spincoating has a very weak dependence on molecular weight of PS (due to the same solvent and similar viscosities among the samples) but strongly depends on solution concentration. Thus, two thicknesses (i.e., 110± 40 nm, 550 ± 60 nm) were prepared from different concentrations (1.67 wt. %, 4.77 wt. %, respectively) in tetrahydrofuran (THF) solutions via spincoating at 1000rpm for 60s (P6700, Specialty Coating Systems, Inc.). The weight ratio of Py to PS was fixed at 1: 2 throughout the experiment. The film thicknesses were measured by a surface profilometer (Veeco, Dektak 150).

Characterizations

• Steady-state fluorescence spectroscopy: The fluorescence of the prepared films was measured by a steady-state fluorescence spectrometer (Flourolog, Jobin Yvon Horiba). The films were excited by photons with a wavelength of 345 nm. The emission spectra were monitored in the range of 360−600

nm through a 1-mm slit and normalized by the maximum intensity of the corresponding spectrum.

• *Time-dependent fluorescence spectroscopy*: The quenching efficiency (Q.E.) of the films with respect to saturated vapor of 2, 4-DNT was measured in the wavelength range of 360 -600nm using Varian Cary Eclipse fluorescence and Jobin Yvon (Horiba) spectrophotometer after being excited by photons with a wavelength of 345nm. The saturated vapor of 2,4-DNT is prepared in the cuvette with cottons and the film was inserted not to touch the 2,4-DNT directly. The changing of the fluorescence intensities (I) were normalized to the initial intensity (I_0) measured right after the exposure to the quencher vapor and the quenching efficiency (Q.E.) is defined as $(I_0 - I)/I_0$ x100(%).

• *UV-Vis Abs spectroscopy:* The UV-Vis abs spectra were acquired by a UV-Vis CARY 4000 (Agilent Technologies) from 190 nm to 700 nm to determine the band gap of materials.

• *Rotating Disk Electrode (RDE) measurements:* For the working electrode, the 10µl of Py/PS solution was coated onto a glassy carbon electrode ($0.2475cm^2$), and dried in a vacuum oven. The electrochemical analysis was performed with an AUTOLAB model PGSTAT 302N potentiostat. A 0.1M tetra-n-butylammonium perchlorate solution (Bu_4NClO_4) in acetonitrile (C_2H_3N) and Saturated Calomel electrode (SCE) were used as the electrolyte and reference electrode, respectively, whereas a mesh attached Pt wire was used as a counter electrode. All the potentials will be referred

to the Silver-Silver Chloride (Ag/AgCl) potential, unless otherwise stated. The electrolyte was purged with pure argon (Ar) at least 30 minutes before (and during) the experiments. Electrochemical analysis reagent grade, Bu_4NClO_4 and ACS grade C_2H_3N were used as received.

5.3. Results and Discussion

Fig. 5. 2 shows the excimer fluorescence intensity of various solid films containing Py in the presence of 2, 4-DNT vapor as a function of time. No quenching was observed in the films of Py and Py/$TBAPF_6$ as shown in Fig. 5. 2 (A) and (B), respectively. However, a significant quenching (~ 50%) was observed in the film of Py/PS after 6 mins being exposed by the 2,4-DNT vapor, suggesting that PS is an essential component for the quenching of Py by 2,4-DNT. It has been hypothesized that the phenyl group of PS can promote the fast quenching of Py excimers.[5] The flexibility of PS has also been presumed to provide the mobility of Py to form the excimer and be quenched by $TBAPF_6$.[6]

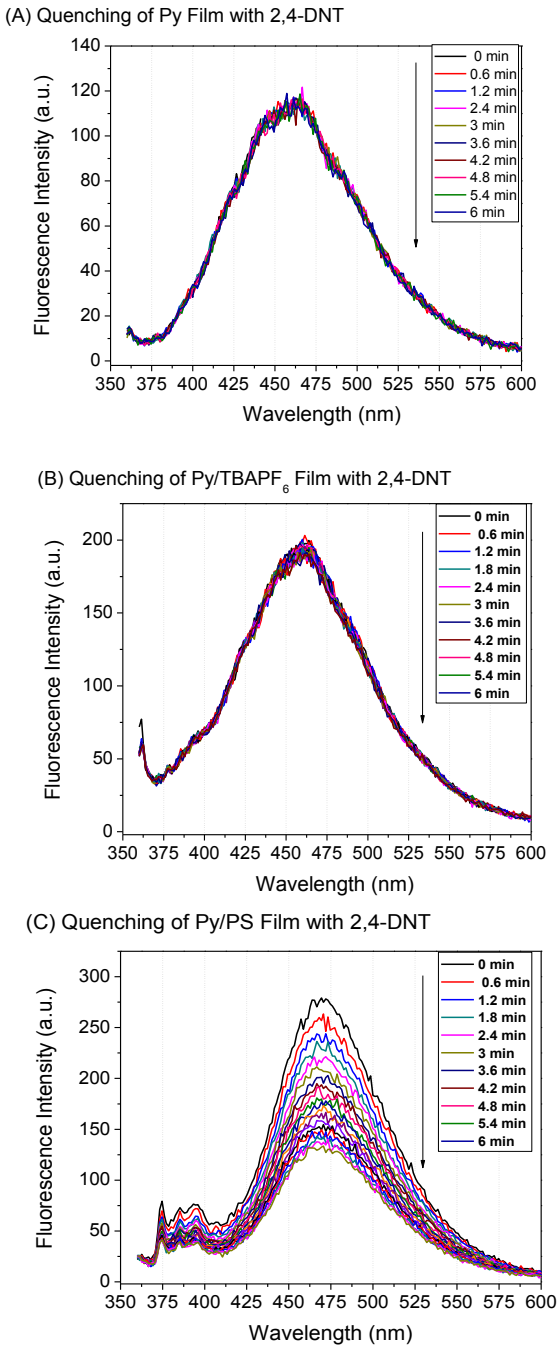

Figure 5.2. The time-dependent fluorescence of (A) Py and (B) Py/$TBAPF_6$ and (C) Py/PS film upon exposure to equilibrium 2, 4-DNT vapor

5.3.1. Effect of PS Architectures and MW

- *Fluorescence Quenching of Py/PS films in presence of 2,4-DNT*

Similar to Fig. 5. 2, Fig. 5. 3 (A) shows a time-dependent quenching behavior of Py/linear PS (MW=500K) film (thickness = 550 $\pm$ 60 nm) with respect to the exposure time in presence of 2,4-DNT vapor. The fluorescence spectra show that the peak at 468 nm decreases with time. It has been reported that a formation of exciplex, a type of charge-transfer complex between electron-rich polymer and nitroaromatic analyte, is occasionally attributed to the fluorescence quenching accompanying with the peak shift in the UV/fluorescence spectra[1, 15]. The observed invariance of the peak position in Fig. 5. 3(A) implies that this quenching may not form a charge-transfer complex between Py/PS and 2,4-DNT. In addition, UV-vis abs spectra of Py/PS film in Fig. 5.S1 also suggests no presence of charge-transfer complex in the system. The Q.E.s of Py in PS of different architectures (i.e., linear, centipede and 4-arm star) are also investigated, indicative of no significant differences from each other as shown in Fig. 5. 3 (B). The result suggests that the effect of PS architecture on the fluorescence quenching by 2,4-DNT is insignificant.

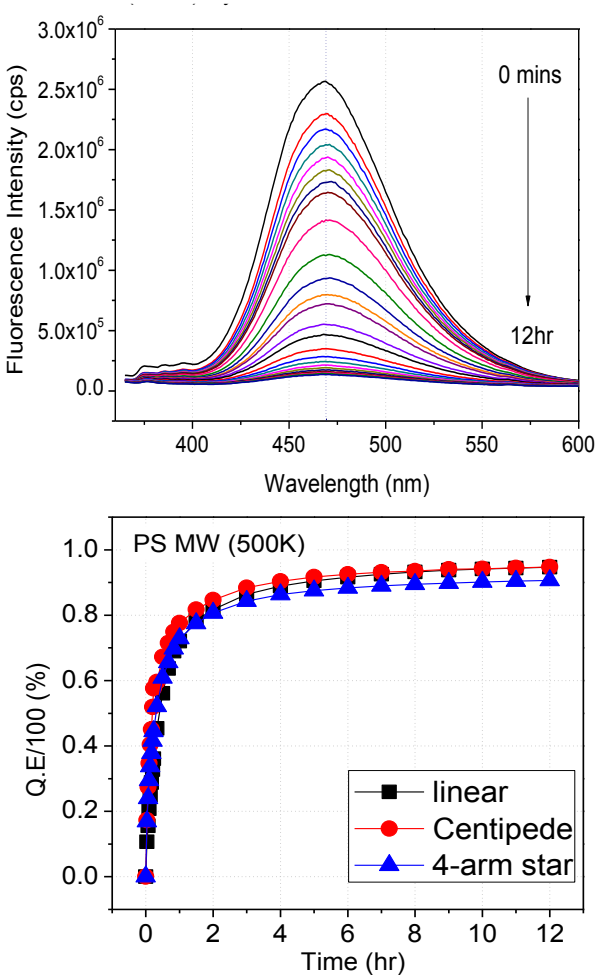

Fig 5.3. (A) The time dependent fluorescence of (A) Py /PS (linear, 500K) film and (B) Quenching efficiency of Py/PS films (black square of linear PS, red circle of centipede PS, and blue triangle of 4-arm star PS)

-Optical and Electrical properties of Py/PS Films

In comparison to the fluorescence spectrum of Py film alone, the spectra of all Py/PS films (including all architectures) exhibit a red shift from 450 to 468 nm [Fig. 5.4 (A)], indicating PS molecules interact with Py excimers in the same way regardless of molecular architectures.

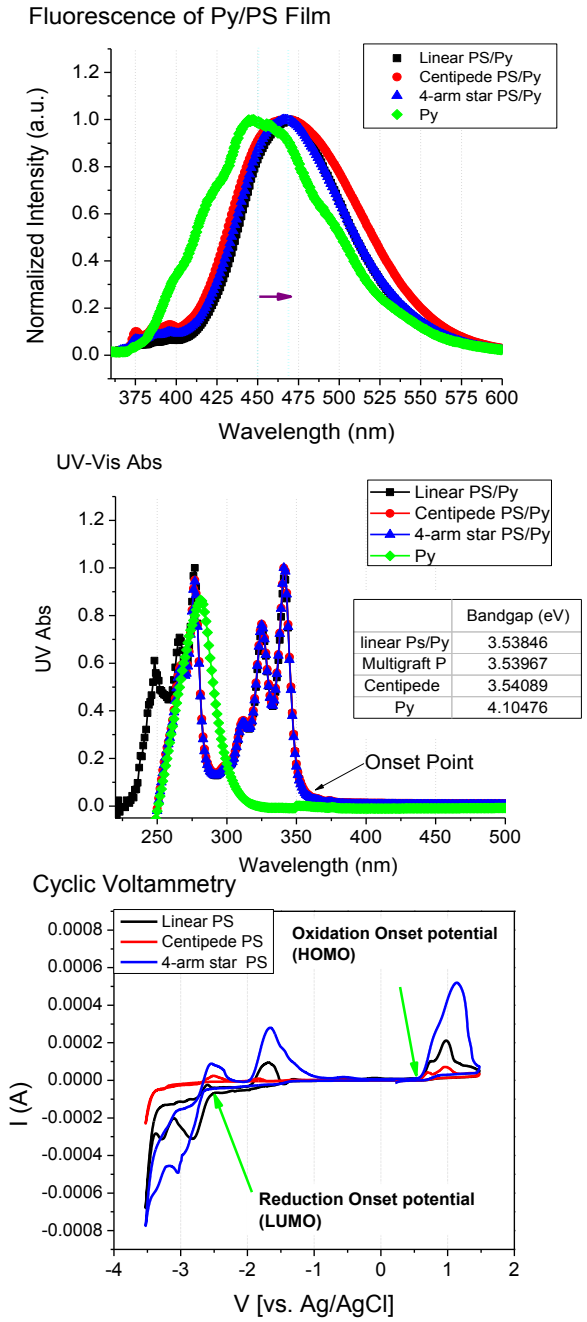

Fig 5.4. (A) Fluorescence spectra (excited at 345 nm) (B) UV-Vis spectra (C) Cyclic voltammetry spectra of different films (i.e. Py, Py/linear PS, Py/Centipede PS, and Py/ 4-arm star PS films)

As the fluorescence of excimer is quenched there are several possible mechanisms: photo-induced electron transfer (PET), Fluorescence (Förster) resonance energy transfer (FRET), excimer/exciplex formation, and photoinduced charge transfer (PCT). The possibility of the formation of charger transfer or exciplex was omitted since the peak locations in the UV-Vis and fluorescence spectra remain invariant through the quenching process [Figs.5. 3 (A). S1, and S2]. The definition of PET is a type of non-radiative deactivation of the excited state, either oxidative and reductive electron transfer processes between donor and acceptor results in fluorescence quenching.[16-17] Accordingly, due to the electron rich nature of polyaromatic hydrocarbon and electron-deficient nature of explosives, the PET process from the sensing film to the explosive molecules was presumed to be the possible reason for effective fluorescence quenching[18-20], which is controlled by the energy gap between the LUMO of donor (i.e. fluorohpore, Py) and that of the acceptor (i.e., explosive) in the oxidative electron transfer process.[17, 21-25] It has known that the quenching efficiency is directly proportional to the rate of the electron transfer (k_{ET}) [17, 22-24]. Based on Marcus theory, the transfer rate can be described as[17, 22-24]

$$k_{ET} = A \exp(-\Delta G^{*}/kT) \quad [1]$$

$$= \frac{2\pi^{3/2}}{h\sqrt{\lambda kT}} V^{2} \exp[-\frac{(\Delta G^{o}+\lambda)^{2}}{4\lambda kT}] \quad [2]$$

where ΔG^{o} is the standard Gibbs free energy difference of the electron transfer reaction, V is the electron coupling between the initial state (D*A)

and final state (D^+A^-), where D and A are electron donor and acceptor, respectively, λ is generally a positive number and represents the reorganization energy which includes two contributions: (i) the internal part λ_i related to the geometric changes of D and A and (ii) the external part λ_e related to the polarizations of the surrounding medium. The ΔG^o is the energy gap between the LUMOs of A (i.e. 2,4,-DNT) and D (i.e. Py/PS films) with one electron approximation.[22-24,28] And electron coupling (V) can be considered as direct LUMOs coupling between D and A, and is strongly dependent upon the distance between and the relative orientation of them. From Eq [2], electron-transfer rate reaches maximum when $-\Delta G^o$ is equal to λ (i.e., $\Delta G^* = 0$). When $|\Delta G^o| < \lambda$, the so-called normal region, the more negative the driving force, the faster the electron transfer rate. When $|\Delta G^o| > \lambda$, the inverted region, the more negative the driving force, the slower the electron transfer rate.

Here, the electrical properties of Py/PS films were investigated through UV-Vis and Cyclic Voltammetry and shown in Fig. 5. 4 (B) and Fig. 5. 4(C). The most commonly accepted approximation for the band gap of structure is derived from the onset point of low energy side absorption in the UV-Vis spectra and converted to the energy (eV) as shown Eq. [3]. The Fig. 5. 4 (B) illustrates the UV-Vis spectra of Py and Py/PS films and its value of band gaps (eV). It shows that after PS is incorporated into the Py films, the onset points of Py/PS films are all shifted to the low energy level compared with that of the Py film along. The band gap of Py/PS films has decreased

about the similar level (~ 0.5eV) regardless of the architecture of PS. From the electrochemistry method, the Highest Occupied Molecular Orbital (HOMO) and the LUMO can be determined from oxidation and reduction onset potentials, where the oxidation onset potential is E_{ox}, and the reduction onset potential is E_{red} according to Eq [4] and shown in Fig.5.4.(C).[26] The value of E_{FOC} for ferrocene is 0.01 V vs. Ag/AgCl and 4.8eV is the energy level of ferrocene under vaccum.[22] Finally, the band gap energy of the Py/PS film can be calculated by Eq. [5] as below.[26] The results are summarized in Table 5.2.

$$E\ (J) = \frac{hc}{\lambda\ (m)}\ ,\ \ E\ (eV) = \frac{1239.84187\ eV{\cdot}nm}{\lambda\ (nm)} \quad [3]$$

$$E_{HOMO/LUMO}\ [V\ vs.\ Ag/AgCl](eV)\ =\ -\ (E_{ox}/E_{red}\ -\ E_{FOC})\ -4.8 \quad [4]$$

$$E_{bandgap}(eV)\ =\ E_{LUMO}\ -E_{HOMO} \quad [5]$$

Samples	Onset oxidation potential [V vs. Ag/AgCl]	Onset reduction potential [V vs. Ag/AgCl]	HOMO potential [V vs. Ag/AgCl]	LUMO potential [V vs. Ag/AgCl]	Band gap potential [V]	
Linear PS	0.63	-2.51	-5.42	-2.28	3.14	±0.06
Centipede PS	0.62	-2.58	-5.41	-2.21	3.20	±0.05
4-arm star PS	0.61	-2.59	-5.40	-2.20	3.19	±0.07

Table 5.2. Evaluated HOMO/LUMO values of Py/PS films

Fig. 5.5 indicates the energy level of LUMO and HOMO of different Py/PS films. It has been reported that PS has a wide energy gap of 6.55eV.[26-27] A noticeable decrease in the LUMO levels of all the Py/PS films was observed in the presence of PS. Hence, this reduction of the band gap as well as the lowered LUMO level of Py/PS films (compared to that of Py film) benefits the 2,4-DNT to accept the electron from the excited state of Py/PS films, leading to PET, consequently quenching the excimer fluorescence. In the same manner, the matching of the LUMO energy of explosives to the excited fluorohpores was attributed to the reason explaining quenching process.[28-29] This reduction of LUMO level of Py in presence of PS is possibly driven by resonance energy transfer between PS and Py. It has been reported that non-radiative energy transfer through non-covalent interaction can change the electron density of molecules.[30] In light of this, the phenyl group of PS may perturb the electronic density state of Py through non-covalent interactions such as π-π interactions.[30]

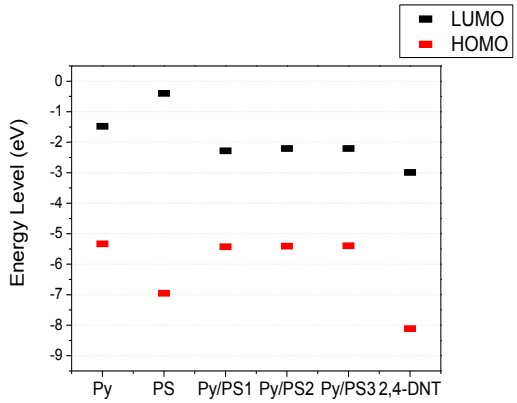

Fig 5.5. Energy Level (eV) of different films (i.e. Py[18, 25], PS[23], Py/PS1 (linear), Py/PS2 (centipede), Py/PS3 (4-arm star) , 2, 4-DNT[26])

To examine the interaction between PS and Py, the UV-Abs and fluorescence were measure and illustrated in Fig. 5.6 (A).It has been reported that PS can form sandwich like excimers through intramolecular associations between excited and unexcited phenyl group in the backbone.[33-36]

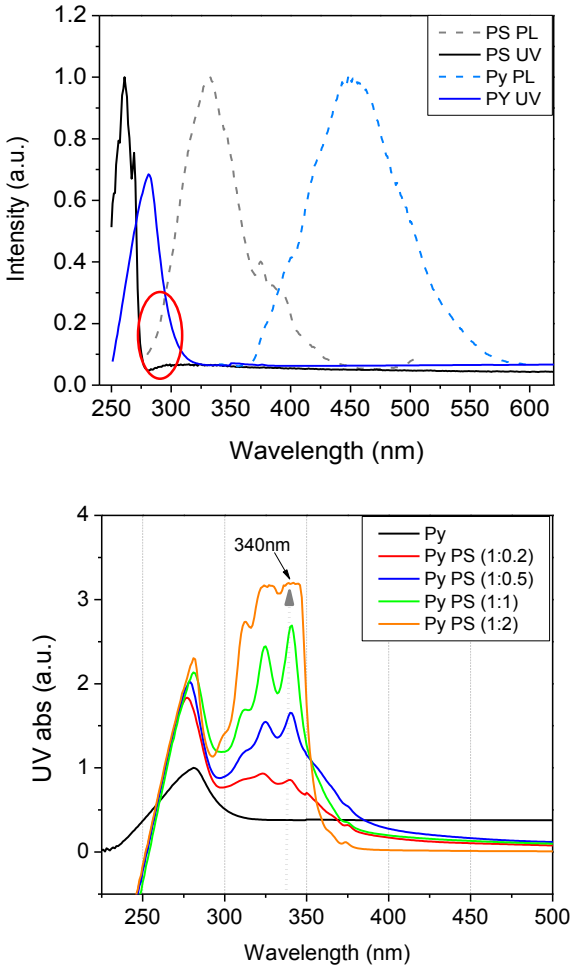

Fig. 5.6 (A) UV abs and fluorescence spectra of Py and PS (B) UV abs spectra of different weight ratio of PS/Py films with fixed concentration (0.1M) of Py

Note that there are the clear overlapping region between the PS emission and the Py UV-absorption spectra in Fig. 5.6 (A), indicative of possible energy transfer from PS to Py. may relate to the interactions between PS excimer and Py excimer.[27, 36] Fig. 5.6 (B) shows an effect of the PS composition on the UV-abs spectra of Py/PS films. By increasing the weight ratio of PS, the UV-abs peak of Py at 340 nm was enhanced, further supporting this proposed energy transfer mechanism from PS to Py through the overlapping region The above-mentioned UV-Vis, fluorescence, and cyclic voltammetry spectra suggest the PS-induced LUMO reduction provides a plausible reason for the effective fluorescence quenching in the presence of 2,4-DNT. Moreover, the energy transfer from PS emission to Py absorption presents a mechanism to enhance the fluorescence of Py excimer. However, different architectures of PS did not show significant contribution to the formation of the excimer or the interaction between Py and PS.

Effect of PS MW

Further investigation on the effect of different MWs of linear PS was conducted to elucidate whether the quenching of Py propagates along the PS backbone. Fig. 5.7 (A) shows similar fluorescence spectra of Py in PS host films of various MWs (from 2.5 to 900 K) with a thickness of 550 ± 60 nm, representing that all PS provide similar environments for Py, also confirmed by the similar UV-vis abs spectra of Py/PS films with the PS of a wide range of MWs (Fig. 5. S4). Fig. 5. 7(B) shows the Q.E. of Py/PS

films of different MW as a function of exposure time in the 2,4-DNT vapor. No strong dependence of the MW on the Q.E. of Py/PS films was found either. This result implies that the quenching of Py by 2,4-DNT may not propagate along the PS backbone, suggesting the "molecular wire" theory may not be applicable in this case.

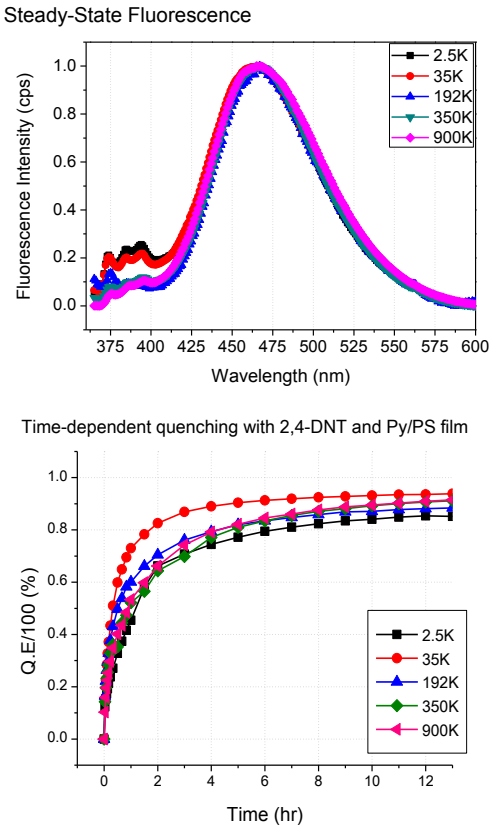

Fig 5.7. (A) Fluorescence spectra (excited at 345 nm) of different MW PS/Py films (B) Quenching efficiency of Py/PS films with respect to 2,4-DNT (i.e. 2.5K (black square), 35K (red circle), 192K (triangle pink), 350K (inverse triangle green), and 900K (rhombus pink)

5.3.2. Effect of film thickness

Fig. 5. 8 shows the Q.E. of the Py/PS films of different architectures of PS and at two thicknesses, i.e., (A) 110 ± 40nm and (B) 550 ± 60 nm in the

presence of saturated 2,4-DNT vapor. The final Q.E.s of both films reaches a similar level of 95% regardless of molecular architectures and film thicknesses. The diffusion coefficient of 2, 4-DNT across the solid film can be calculated through the Fick's second law.

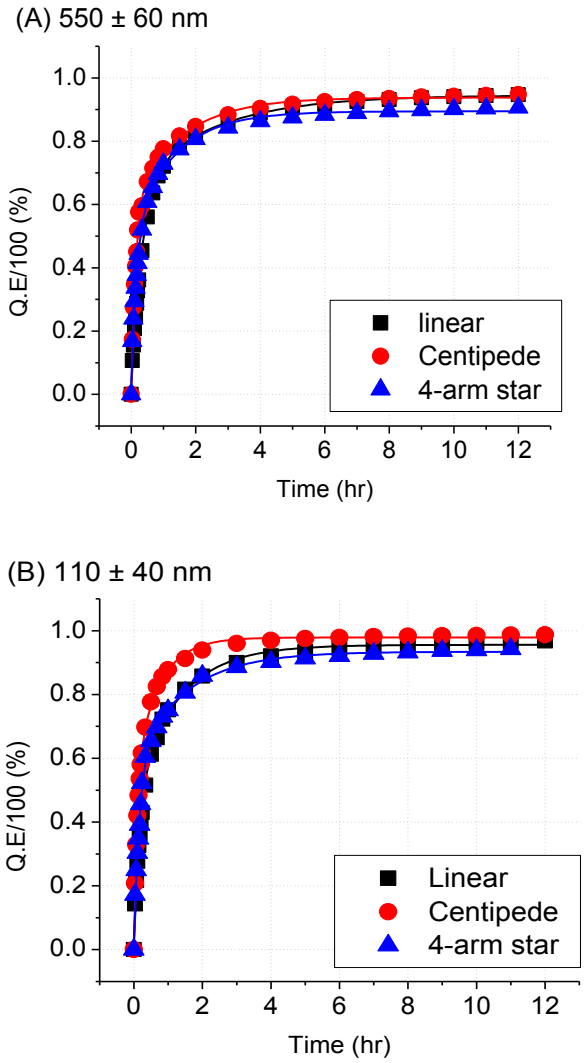

Figure 5.8. The time-dependent fluorescence quenching efficiency of (A) Py/PS films (thickness: 550±60nm) (B) Py/PS films (thickness: 110 ± 40nm) of different PS architecture (linear, centipede and 4-arm star), respectively.

To avoid self-quenching, an investigation on the correlation between the fluorescence intensity and film thickness was conducted prior to the diffusion experiment as shown Fig. 5. 9. Samples should be only selected under the condition that the fluorescence is linearly dependent on the film thickness (i.e., the amount of Py in the film). As a result, two films of thicknesses, (550 ± 60) nm and (110 ± 40) nm were chosen.

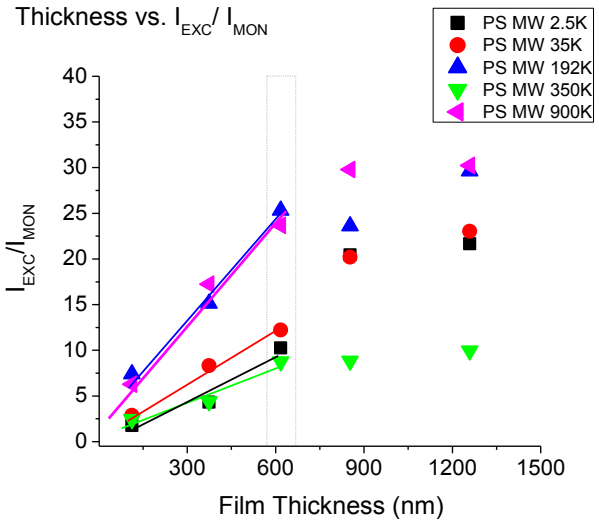

Fig. 5.9. The fluorescence ratio of I_{exc}/I_{mon} of different thicknesses of Py/PS films. Lines indicate the linear fluorescence response of the Py/PS films composed of different-MW polystyrenes.

It is assumed that the concentration of the 2,4-DNT remains constant (at the saturated pressure) near the surface of films and that the quenching of the fluorescence is proportional to the amount of 2,4-DNT in the film with a fixed ratio of stoichiometry. Then, the diffusion of 2,4-DNT across Py/PS films can be described in Eq. [6])[37-39] by assuming a constant diffusion coefficient, for concentration changes in time. As a result, the combination of Stern-Volmer quenching (Eq. [8]) equation and time independent Smoluchowski–Einstein equation (Eq. [9]) yields Eq. [12] which shows a simple form of single exponential decay.[40] The solid curves in Fig. 5. 8 are the best fits based on the calculation of the equations, which capture the quenching phenomenon reasonably well. Assumption is that quenching of Py/PS films follows exponential decay and k_q is single-value and $D_P << D_q$ when the Py/PS is is fixed to the substrate. Eq [8] is modified by expanding in a series with $k_q\tau_0[Q] << 1$ which produces the Eq [10]. During diffusion of 2,4-DNT into the Py/PS films, Py are quenched in the volume which is occupied by 2,4-DNT molecules[Q(t)] at time,t. Then fluorescence intensity at time t can be represented by the volume integration of Eq [11]. Also, it is assumed that Q(t) corresponds to the amount of 2,4-DNT that diffuses into the film(M_t).

$$\frac{C}{C_0} = \frac{x}{d} + \frac{2}{\pi}\sum_{n=1}^{\infty}\frac{\cos n\pi}{n} sin\frac{n\pi x}{d}\exp(-\frac{Dn^2\pi^2 t}{d^2}),\quad M = \int C\ dV \qquad [6]$$

$$\frac{M_t}{M_\infty} = 1 - \frac{8}{\pi^2}\sum_{n=0}^{\infty}\frac{1}{(2n+1)^2}\exp\left(-\frac{D(2n+1)^2\pi^2 t}{d^2}\right) \qquad [7]$$

$$\frac{I_0}{I_t} = 1 + k_q\tau_0[Q], \qquad [8]$$

$$k_q = pk_0 = \frac{4\pi N_A(D_P+D_q)pR}{1000} \qquad [9]$$

$$I_t \approx I_0(1 - k_q\tau_0[Q]), \quad k_q\tau_0[Q] \ll 1 \qquad [10]$$

$$I_t = \frac{\int I\ dv}{\int dv} = I_0\left(1 - \frac{k_q\tau_0}{V}\ Q(t)\right), \quad Q(t) = \int dv[Q] \qquad [11]$$

$$\frac{I_t}{I_0} = A + \frac{8C}{\pi^2}\exp(-\frac{D\pi^2 t}{d^2}) \qquad [12]$$

where d being the film thickness (cm), C_o and C being the concentration of 2,4-DNT at the location of x in the film initially and at time of t, respectively, M_t and M_∞ being the amount of 2,4-DNT that diffuses into the film at t and infinity, respectively. I_0 and I are the fluorescence intensity in presence of the 2,4-DNT initially and at t, respectively. τ_0 is the lifetime of a fluorophore in the absence of quencher, and k_q is the bimolecular quenching rate constant. D_p and D_q are diffusion coefficients of the excited fluorophore and quencher, respectively, p is the quenching probability per collision, R is the sum of the collision radii (R_P + R_q), [Q] is the concentration of the quencher (2,4-DNT) in the environment, where the films are exposed to, and N_A is Avogadro's number. V and dv are the differential and total volume of Py/PS film. $Q(t)$ is the amount of 2,4-DNT

molecules diffuse into the film at time t. The coefficient, C in Eq [12] is $k_q \tau_0 Q(\infty)/V$ and A is equal to 1 − C. Here, Q(∞) is the amount of 2,4-DNT molecules diffused into the film at t=∞.

We have found that though the single exponential decay expressed in Eq. [12] is sufficient to describe the fluorescence decay in the short time (i.e., the first 6 mins in Fig. 5. S5). However, to fit the data over a longer time scale, two exponential decays (i.e., two diffusion coefficients) are required. Figs.5.10 (A) and (B) reveal the best fitting diffusion coefficients of single exponential and double exponential decays from the fluorescence response of the films in cases of short- and long- time frames, respectively. The result indicates that the diffusion coefficients of 2,4-DNT strongly depend on the film thickness. However, no significant dependences of the MWs and molecular architectures of PS on the diffusion coefficient were observed. The average diffusion coefficients for Py/PS films of 110 ± 40 nm and 550 ± 60 nm in a short-time scale (6 mins) are 9.6 $x10^{-14}$ and 1.5 $x10^{-12}$ cm^2/sec, respectively, representing a higher value of diffusion coefficient of 2,4-DNT for the 550-nm film.

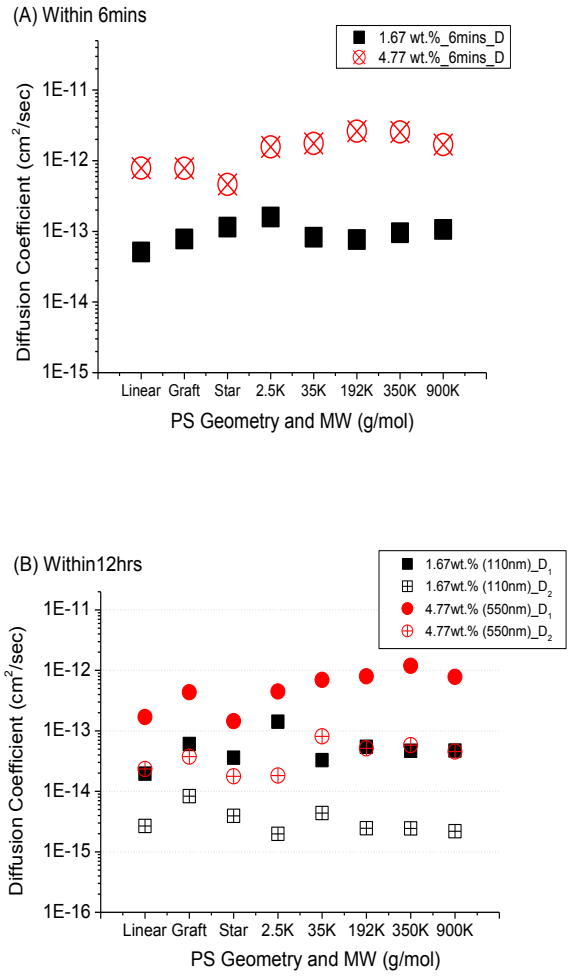

Fig. 5. 10 The best-fitting diffusion coefficients (cm^2/sec) of Py/PS films [110nm (black), and 550nm (red)]. Polystyrenes of the different MWs and architectures are investigated: (A) and (B) reveal the diffusion coefficients obtained from the best-fits of the short-time frame (6 mins) and the long-time frame (12 hrs) experimental data

Fig. 5. 10 (C) shows that the short-time diffusion coefficients obtained from the single-exponential decay are generally consistent with those of the fast-mode diffusion coefficients (D_1) in Fig. 5. 10 (B) obtained from the double-exponential decay (5.5 x 10^{-14} and 5.8 x 10^{-13} cm^2/sec in the case of 110-nm and 550-nm films, respectively).

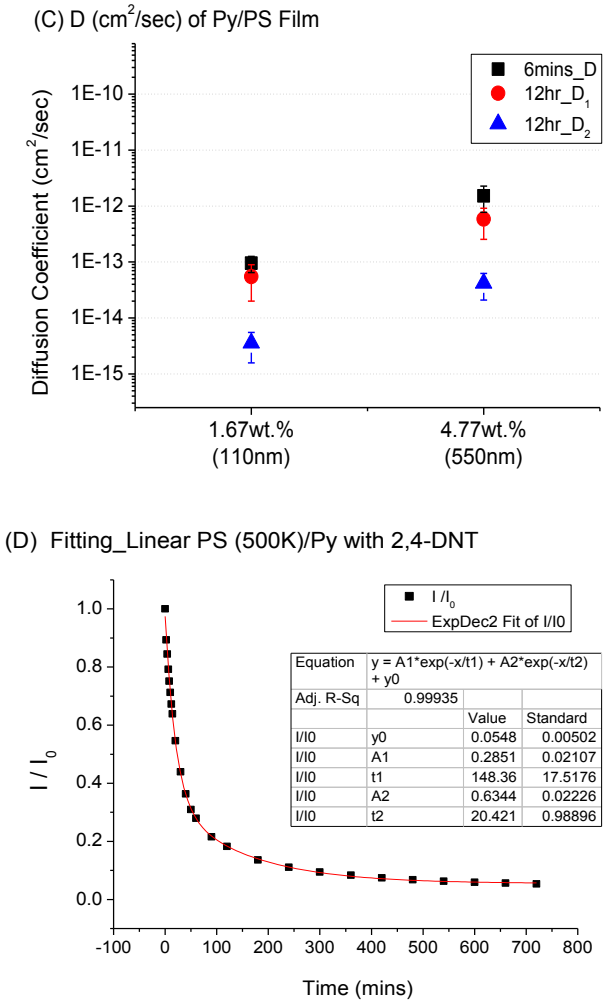

Fig. 5.10 (c) comparison of diffusion coefficients (obtained from single- and double- exponential decay) at two different thicknesses and (D) fluorescence decay of Py/PS films at 468nm and its fitting

The thicker film also yields a higher value of the slow-mode diffusion coefficient (D_2) of 2,4-DNT (4.16×10^{-14} cm^2/sec) in comparison with that in the case of the thinner film (3.55×10^{-15} cm^2/sec). The two diffusion mechanisms of the 2,4-DNT into the Py/PS films, namely the slow and the fast mode, may arise from surface diffusion and molecular diffusion.[41-42] The former may be related to the adsorption nature of 2,4-DNT to the film surface (or accessible pores of the film), while the latter may be accounted for the diffusion through the solid region of the film. The dependence of the film thickness on the 2,4-DNT diffusion constants is possibly attributed to the increased surface roughness and interconnected pores accessible to external vapor with increased film thickness, thus allowing fast gas transport.[41, 43]

5.4. Conclusion

The effect of PS architectures and MWs of the Py/PS thin films on the Py excimer fluorescence and its quenching has been investigated in the presence of 2,4-DNT. Little or no dependence of different architectures and MWs of PS on quenching was observed. However, LUMO level and band gap of Py have been reduced in presence of PS due to the non-radiative energy transfer between PS and Py. The reduction of the LUMO level of Py in presence of PS presumably facilitates the quenching of Py excimer by the 2,4-DNT. No significant peak shift in the fluorescence spectra during the quenching process indicates that quenching mechanism in this system is

most likely driven by the PET process. Finally, the diffusion coefficients of 2,4-DNT in the Py/PS film were evaluated through fluorescence quenching. The result suggests that 2,4-DNT interacts with Py/PS films in two different mechanisms – the fast and slow modes. The thickness of the films presents a key parameter to dictate the diffusion coefficients. Thicker Py/PS film shows higher diffusion coefficients in both modes. This is possibly attributed to the enhanced surface roughness (or porosity) in the thicker films.

5.5. Supporting Information

Fig. 5.S1. UV-Abs and fluorescence emission spectra of different Py/PS films after exposed to 2,4-DNT. The onset point of UV-Abs looks more less similar to each other and also the peak maxima position of Py did not alter during fluorescence quenching with 2,4-DNT in the fluorescence emission spectra, representing no clear bandgap change during the interaction with 2,4-DNT.

(a) Py/PS Film, Thickness, 110 nm

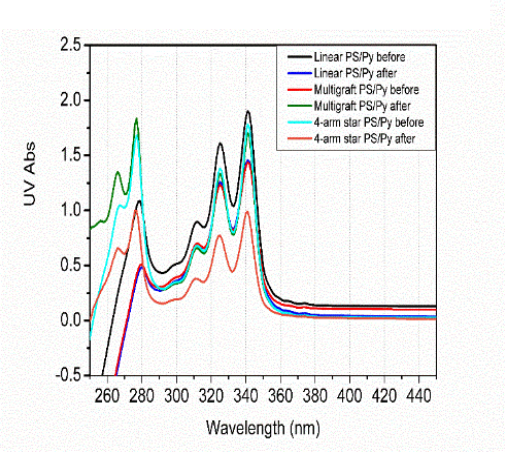

(b) Py/PS Film, Thickness, 550 nm

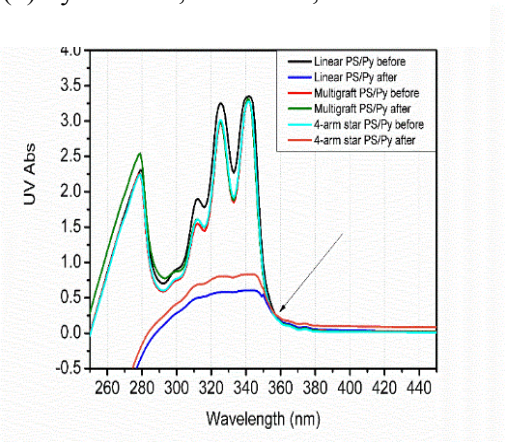

Figure S1. The UV-vis absorption spectra of Py/PS films with thicknesses of (a) 110 nm and (b) 550 nm . The PS has different molecular architectures. The spectra were measured prior to and after exposure of 2,4-DNT. The onset points of UV-vis Abs spectra obtained from different samples are similar to each other.

(a) centipede-PS (500K)/PS thickness = 550 nm

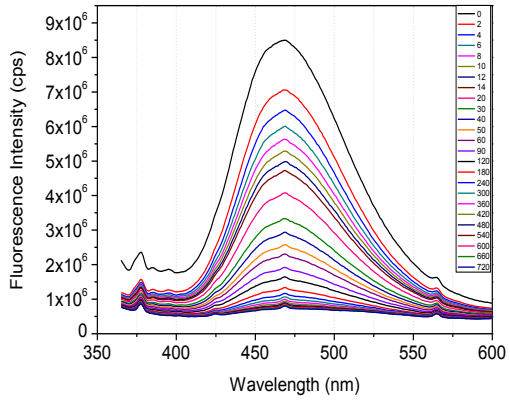

(b) 4arm-star-PS (500K)/PS thickness = 550 nm

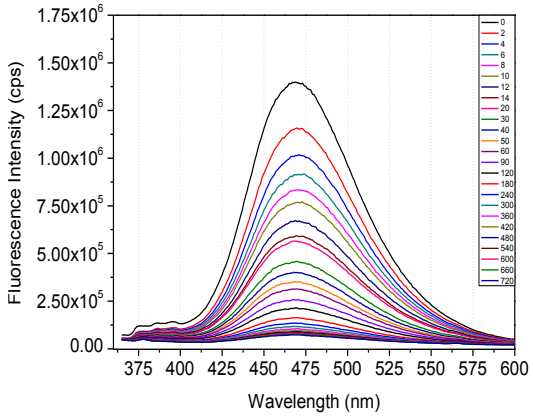

(c) linear-PS (500K)/PS thickness = 110 nm

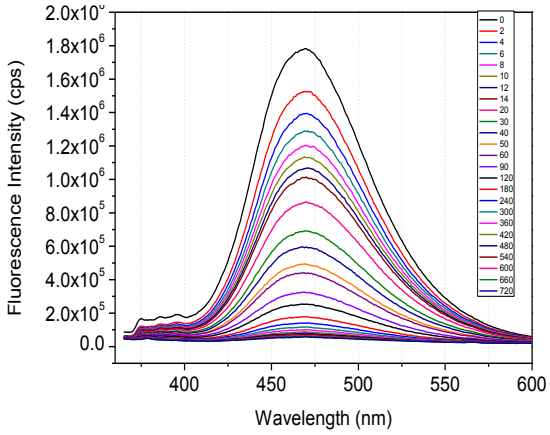

(d) centipede-PS (500K)/PS thickness = 110 nm

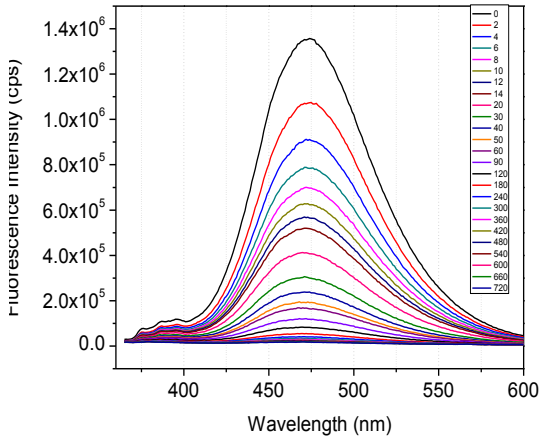

(e) 4arm-star-PS (500K)/PS thickness = 110 nm

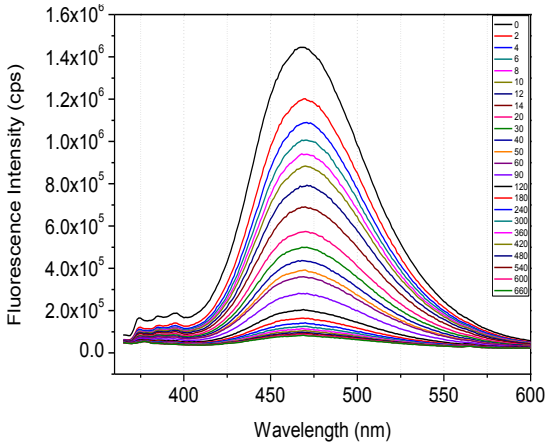

Figure S2. Time-dependent fluorescence emission spectra of Py/PS films composed of PS with different molecular architectures in the presence of 2,4-DNT. (a), (b) are the results obtained from the 550 nm thick film while (c)-(e) represents results from the 110 nm thick films.

Fig.5.S3 Quenching efficiency of the 550-nm Py/PS films in the presence of various nitroexplosives (i.e. 2,4-DNT, 1,3-DNB and picric acid). After 12hrs being exposed to the explosives, all Py/PS films show 90 % or above quenching efficiencies.

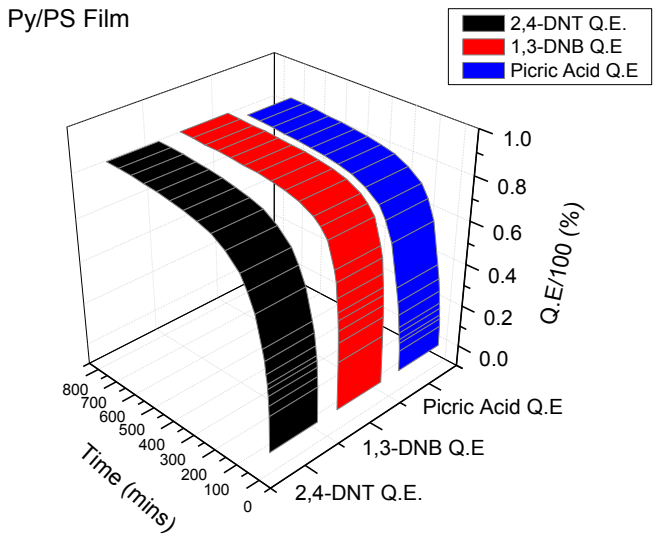

Fig.5.S4 The UV-vis abs spectra of different Py/PS films (i.e. 35K, 192K, 350K and 900K) with a fixed weight ratio of PS to Py (2:1) where the Py concentrations in the solutions for film preparation are also fixed at 0.1 M. The peak positions of different Py/PS films are similar, indicating that no significant MW of PS on change of Py bandgap with fixed weight ratio of PS.

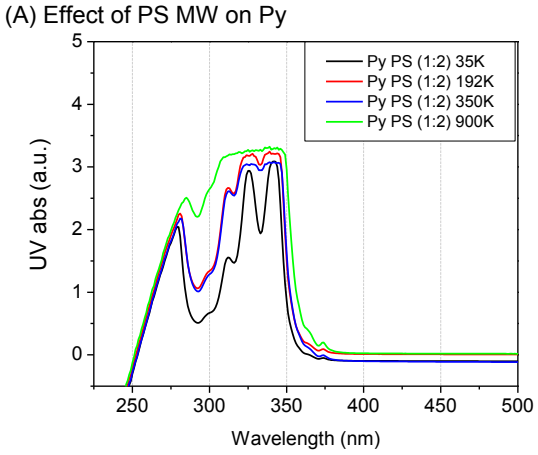

Fig.5.S5 Best fitting results of fluorescence intensity of Py/PS films at 468nm with 2,4-DNT in two time frames: 6 mins (short-time scale) and 12 hrs (long-time scale)

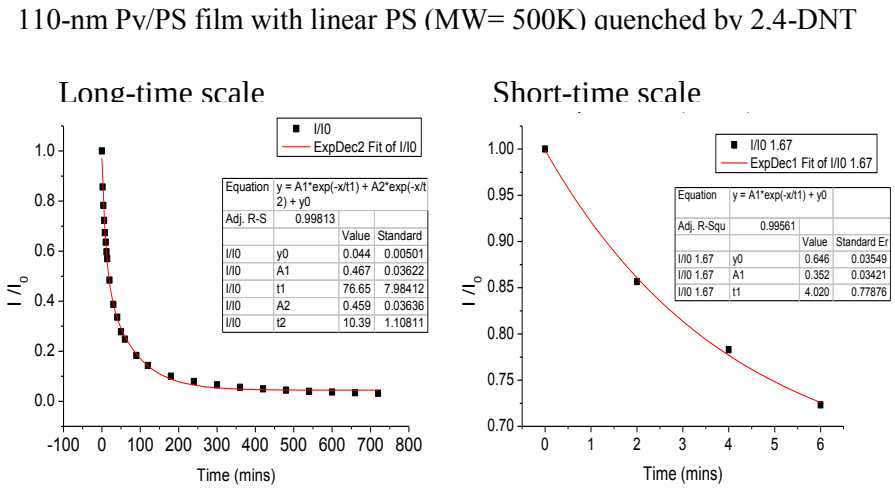

110-nm Py/PS film with 4-arm star PS (MW= 500K) quenched by 2,4-DNT

Long-time scale

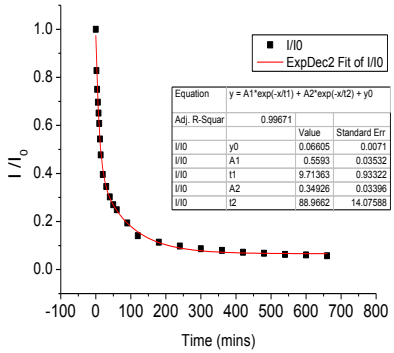

Short-time scale

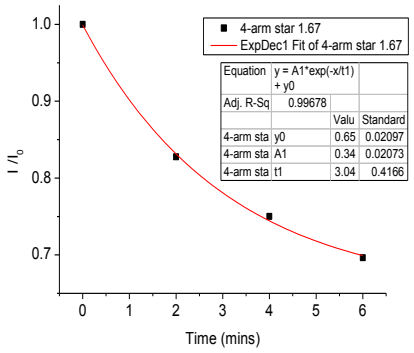

110-nm Py/PS film with centipede PS (MW= 500K) quenched by 2,4-DNT

Long-time scale

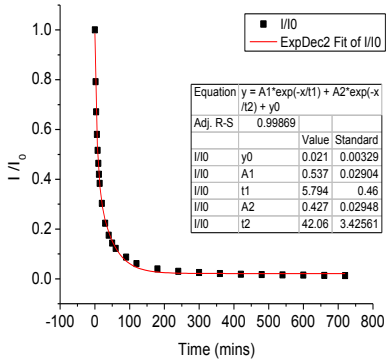

Short-time scale

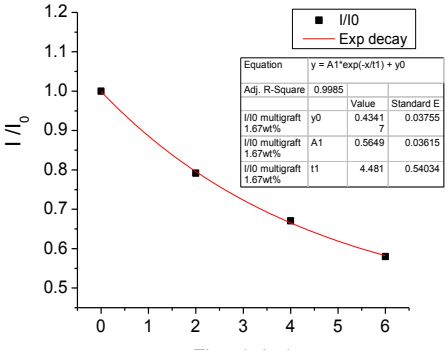

550-nm Py/PS film with linear PS (MW= 500K) quenched by 2,4-DNT

Long-time scale

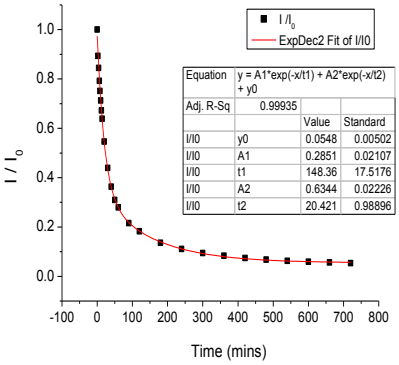

Short-time scale

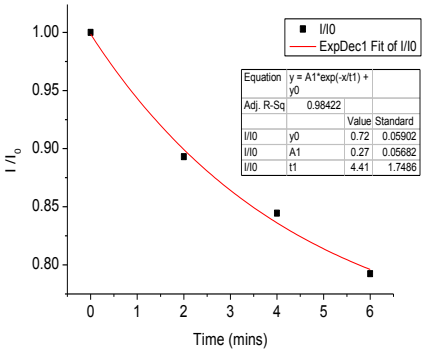

550-nm Py/PS film with 4-arm star PS (MW= 500K) quenched by 2,4-DNT

Long-time scale

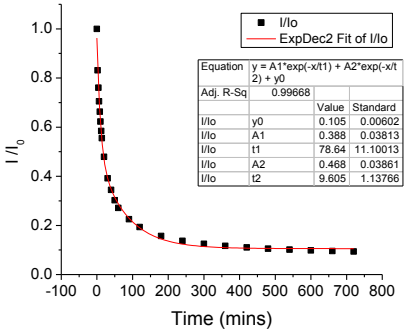

Short-time scale

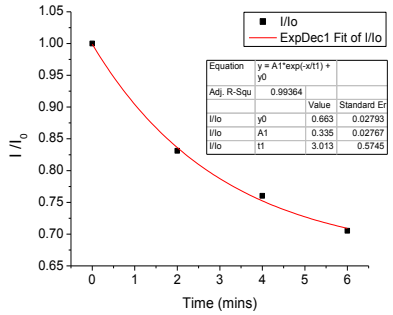

550-nm Py/PS film with centipede PS (MW= 500K) quenched by 2,4-DNT

Long-time scale

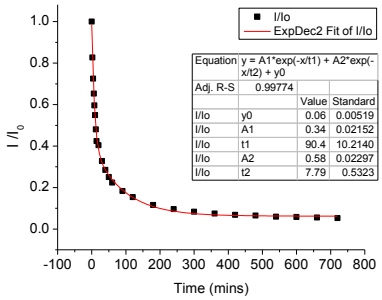

Short-time scale

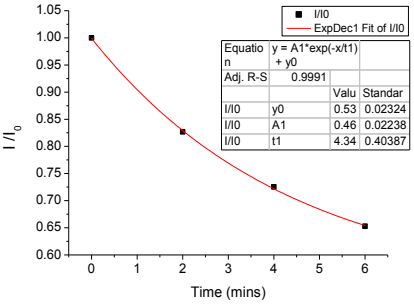

5.6. References

1. Toal, S. J.; Trogler, W. C., Polymer sensors for nitroaromatic explosives detection. *Journal of Materials Chemistry* **2006,** *16* (28), 2871-2883.

2. Sohn, H.; Calhoun, R. M.; Sailor, M. J.; Trogler, W. C., Detection of TNT and Picric Acid on Surfaces and in Seawater by Using Photoluminescent Polysiloles. *Angewandte Chemie International Edition* **2001,** *40* (11), 2104-2105.

3. Swager, T. M., The Molecular Wire Approach to Sensory Signal Amplification. *Accounts of Chemical Research* **1998,** *31* (5), 201-207.

4. Thomas, S. W.; Joly, G. D.; Swager, T. M., Chemical sensors based on amplifying fluorescent conjugated polymers. *Chemical Reviews* **2007,** *107* (4), 1339-1386.

5. Wang, Y.; La, A.; Ding, Y.; Liu, Y.; Lei, Y., Novel Signal-Amplifying Fluorescent Nanofibers for Naked-Eye-Based Ultrasensitive Detection of Buried Explosives and Explosive Vapors. *Advanced Functional Materials* **2012,** *22* (17), 3547-3555.

6. Jang, H.-S.; Wang, Y.; Lei, Y.; Nieh, M.-P., Controllable Formation of Pyrene (C16H10) Excimers in Polystyrene/Tetrabutylammonium Hexafluorophosphate Films through Solvent Vapor and Temperature Annealing. *The Journal of Physical Chemistry C* **2012,** *117* (3), 1428-1435.

7. Jang, H.-S.; Zhao, J.; Lei, Y.; Nieh, M.-P., Unique Effects of the Chain Lengths and Anions of Tetraalkylammonium Salts on Pyrene Excimer Quenching. *Journal of the Applied Interface and Materials* **2014**.

8. Torres, J. M.; Stafford, C. M.; Uhrig, D.; Vogt, B. D., Impact of chain architecture (branching) on the thermal and mechanical behavior of polystyrene thin films. *Journal of Polymer Science Part B: Polymer Physics* **2012,** *50* (5), 370-377.

9. Morton, M.; Fetters, L. J., Anionic Polymerization of Vinyl Monomers. *Rubber Chemistry and Technology* **1975,** *48* (3), 359-409.

10. Hadjichristidis, N.; Iatrou, H.; Pispas, S.; Pitsikalis, M., Anionic polymerization: High vacuum techniques. *Journal of Polymer Science Part A: Polymer Chemistry* **2000,** *38* (18), 3211-3234.

11. Uhrig, D.; Mays, J. W., Experimental techniques in high-vacuum anionic polymerization. *Journal of Polymer Science Part A: Polymer Chemistry* **2005,** *43* (24), 6179-6222.

12. Koutalas, G.; Iatrou, H.; Lohse, D. J.; Hadjichristidis, N., Well-Defined Comb, Star−Comb, and Comb-on-Comb Polybutadienes by Anionic Polymerization and the Macromonomer Strategy. *Macromolecules* **2005,** *38* (12), 4996-5001.

13. Chalari, I.; Hadjichristidis, N., Synthesis of well-defined second-generation dendritic polymers of isoprene (I) and styrene (S): (S2I)3, (SI′I)3, (I″I′I)3, and (I′2I)4. *Journal of Polymer Science Part A: Polymer Chemistry* **2002,** *40* (10), 1519-1526.

14. Driva, P.; Iatrou, H.; Lohse, D. J.; Hadjichristidis, N., Anionic homo- and copolymerization of double-tailed macromonomers: A route to novel macromolecular architectures. *Journal of Polymer Science Part A: Polymer Chemistry* **2005,** *43* (18), 4070-4078.

15. Liu, Y.; Mills, R. C.; Boncella, J. M.; Schanze, K. S., Fluorescent Polyacetylene Thin Film Sensor for Nitroaromatics. *Langmuir* **2001,** *17* (24), 7452-7455.

16. Kim, J. S.; Quang, D. T., Calixarene-Derived Fluorescent Probes. *Chemical Reviews* **2007,** *107* (9), 3780-3799.

17. Valeur, B., *Molecular fluorescence: principles and applications*. Wiley-VCH: **2002**.

18. Goodpaster, J. V.; Harrison, J. F.; McGuffin, V. L., Ab Initio Study of Selective Fluorescence Quenching of Polycyclic Aromatic Hydrocarbons. *The Journal of Physical Chemistry A* **2002,** *106* (44), 10645-10654.

19. Meaney, M. S.; McGuffin, V. L., Investigation of common fluorophores for the detection of nitrated explosives by fluorescence quenching. *Analytica Chimica Acta* **2008,** *610* (1), 57-67.

20. Chernyak, V.; Reisfeld, R., Spectroscopic behaviour of malachite green in sol-gel glasses. *Chemical Physics Letters* **1991,** *181* (1), 39-44.

21. Lakowicz, J. R., *Principles of Fluorescence Spectroscopy: CD-ROM*. Springer: **2006**.

22. Ceroni, P., *The Exploration of Supramolecular Systems and Nanostructures by Photochemical Techniques: Exploration of Supramolecular Systems and Nanostructures By Photochemical Techniques*. Springer: **2011**.

23. Marcus, R. A., Electron transfer reactions in chemistry. Theory and experiment. *Reviews of Modern Physics* **1993,** *65* (3), 599-610.

24. Gaal, D. A.; Hupp, J. T., Photo-Induced Electron Transfer Reactivity at Nanoscale Semiconductor-Solution Interfaces: Case Studies with Dye-Sensitized SnO~ 2-Water Interfaces. **2003**.

25. Skotheim, T. A.; Reynolds, J., *Conjugated Polymers: Processing and Applications*. Taylor & Francis: **2006**.

26. Yin, C.-R.; Han, Y.; Li, L.; Ye, S.-H.; Mao, W.-W.; Yi, M.-D.; Ling, H.-F.; Xie, L.-H.; Zhang, G.-W.; Huang, W., Hindrance-functionalized [small pi]-stacked polymer based on polystyrene with pendent cardo groups for organic electronics. *Polymer Chemistry* **2013,** *4* (8), 2540-2545.

27. Ye, X.; Li, Z.-H.; Wang, W.; Fan, K.; Xu, W.; Hua, Z., The parallel π–π stacking: a model study with MP2 and DFT methods. *Chemical Physics Letters* **2004,** *397* (1–3), 56-61.

28. He, G.; Yan, N.; Yang, J.; Wang, H.; Ding, L.; Yin, S.; Fang, Y., Pyrene-Containing Conjugated Polymer-Based Fluorescent Films for Highly Sensitive and Selective Sensing of TNT in Aqueous Medium. *Macromolecules* **2011,** *44* (12), 4759-4766.

29. Fei, T.; Jiang, K.; Zhang, T., Highly sensitive TNT photoluminescent sensing by a phosphorescent complex. *Sensors and Actuators B: Chemical* (0).

30. Fernando, K. A. S.; Lin, Y.; Wang, W.; Kumar, S.; Zhou, B.; Xie, S.-Y.; Cureton, L. T.; Sun, Y.-P., Diminished Band-Gap Transitions of Single-Walled Carbon Nanotubes in Complexation with Aromatic Molecules. *Journal of the American Chemical Society* **2004,** *126* (33), 10234-10235.

31. Hammonds, M.; Pathak, A.; Sarre, P. J., TD-DFT calculations of electronic spectra of hydrogenated protonated polycyclic aromatic hydrocarbon (PAH) molecules: implications for the origin of the diffuse interstellar bands? *Physical Chemistry Chemical Physics* **2009,** *11* (22), 4458-4464.

32. Sanchez, J. C.; DiPasquale, A. G.; Rheingold, A. L.; Trogler, W. C., Synthesis, Luminescence Properties, and Explosives Sensing with 1,1-Tetraphenylsilole- and 1,1-Silafluorene-vinylene Polymers. *Chemistry of Materials* **2007,** *19* (26), 6459-6470.

33. Hirayama, F., Intramolecular Excimer Formation. I. Diphenyl and Triphenyl Alkanes. *The Journal of Chemical Physics* **1965,** *42* (9), 3163-3171.

34. Vala, M. T.; Haebig, J.; Rice, S. A., Experimental Study of Luminescence and Excitation Trapping in Vinyl Polymers, Paracyclophanes, and Related Compounds. *The Journal of Chemical Physics* **1965,** *43* (3), 886-897.

35. YANARI, S. S.; BOVEY, F. A.; LUMRY, R., Fluorescence of Styrene Homopolymers and Copolymers. *Nature* **1963,** *200* (4903), 242-244.

36. Klöpffer, W., ENERGY TRANSFER IN FILMS OF POLYMERS WITH AROMATIC SIDE-GROUPS. *Annals of the New York Academy of Sciences* **1981,** *366* (1), 373-386.

37. Szabo, A., Theory of diffusion-influenced fluorescence quenching. *The Journal of Physical Chemistry* **1989,** *93* (19), 6929-6939.

38. Wilson, J. E., Diffusion Effects in the Photochemistry of Solid Films. *The Journal of Chemical Physics* **1954,** *22* (2), 334-343.

39. Yekta, A.; Masoumi, Z.; Winnik, M. A., Luminescence measurements of oxygen permeation and oxygen diffusion in thin polymer films. *Canadian Journal of Chemistry* **1995,** *73* (11), 2021-2029.

40. Yargı, Ö.; Uğur, Ş.; Pekcan, Ö., Fluorescence quenching method for monitoring oxygen diffusion into PS/CNT composite films. *Progress in Organic Coatings* **2013,** *76* (12), 1805-1809.

41. Sakai, G.; Matsunaga, N.; Shimanoe, K.; Yamazoe, N., Theory of gas-diffusion controlled sensitivity for thin film semiconductor gas sensor. *Sensors and Actuators B: Chemical* **2001,** *80* (2), 125-131.

42. Choi, J.-G.; Do, D. D.; Do, H. D., Surface Diffusion of Adsorbed Molecules in Porous Media: Monolayer, Multilayer, and Capillary Condensation Regimes. *Industrial & Engineering Chemistry Research* **2001,** *40* (19), 4005-4031.

43. Sun, J.-N.; Hu, Y.; Frieze, W. E.; Chen, W.; Gidley, D. W., How Pore Size and Surface Roughness Affect Diffusion Barrier Continuity on Porous Low-k Films. *Journal of The Electrochemical Society* **2003,** *150* (5), F97-F101.

Chapter 6.

Incorporation of AuNPs into lipids bilayers via self-assembly

6.1. Introduction

Gold nanoparticles (AuNPs) have gained attentions in biomedical applications for their advantages of low toxicity, high contrast in imaging, and capability of absorbing or emitting the infrared which has a high penetration to tissues.[1-4] SERS effect of AuNPs has introduced to enhance the infrared absorption or emission about a factor of 10^8.[5-6] It is well established that shape, size of and distance between the NPs are crucial for SERS/plasmonic effect.[8-11] As well as a roughness on the surfaces can greatly enhance the Raman signal by many orders of magnitude. Such enhancement empowers many applications including single-molecule sensing,[6, 12-13] bio-diagnosis,[14-15] and therapeutics.[16-17] For in-vivo applications (diagnostic or therapeutic), challenges on biocompatibility and size-control need to be addressed. In this regard, phospholipids have been used as theranostic carriers due to their biocompatibility as well as the ease of entrapping foreign molecules. As a result, utilization of the lipid template to carry AuNPs may provide a way to overcome the aforementioned

challenges. The interaction between AuNP and lipids has been studied extensively. In most cases, vesicle is the most general structure observed since only one type of lipid was involved in the studies.[18-25] It has been reported that various morphologies of lipid aggregates can be designed in a mixture of lipids with distinct hydrophobic chain lengths.[26-31]

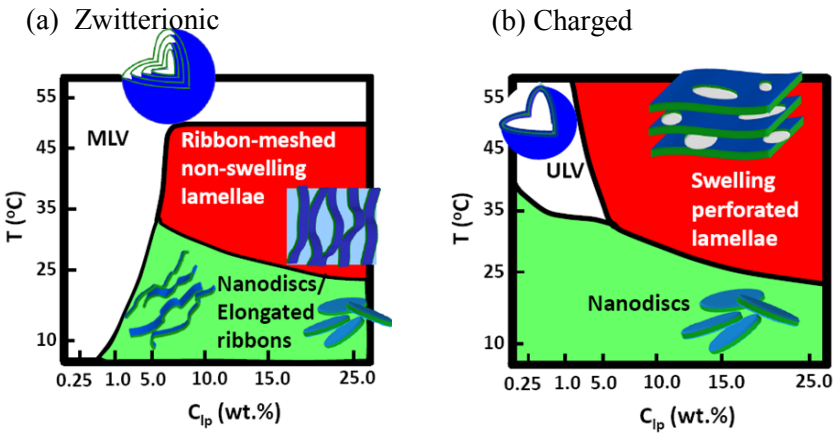

Fig. 6.1 Spontaneous structural phase diagrams of (a) zwitterionic mixture of DMPC/DHPC and (b) charged mixture of DMPC/DHPC/DMPG

Fig 6.1 summarizes the spontaneous structures of a lipid mixture composed of a long-chain dimyristoyl phosphatidyl choline (DMPC) and a short-chain dihexanoyl phosphatidyl choline (DHPC) as a function of temperature, T and total lipid concentration, C_{lp} based on the results of nuclear magnetic resonance (NMR),[32] cryogenic transmission electron microscopy (cryo-TEM)[33] and small angle neutron scattering (SANS).[27, 31] These structural transformations are strongly influenced by the packing parameters of the molecules and the miscibility between DMPC and DHPC. At low temperature (24°C), DMPC is in the gel (crystalline) phase – immiscible

with DHPC in the fluidic (L) phase. The two lipids segregate from each other forming discoidal micelles (i.e., nanodiscs) or bilayered ribbons, where the low-curvature planar and high-curvature rim regions are made of gel-phase DMPC and L-phase DHPC, respectively. With increased T the DMPC melts into L□ phase – becoming more miscible with DHPC, and drawing DHPC into the bilayer, thus resulting in increased line tension at the rim. Consequently the nanodiscs or ribbons coalesce into larger aggregates such as lamellae or vesicles.[26, 34] The nanodiscs are uniform with radii of 10 ~ 25 nm and a thickness of 5 nm.[29, 34] The hydrophobic core of the nanodiscs has a great potential to incorporate hydrophobic molecules. In addition to temperature, the charge density of the bilayer may also play an important role in the morphological transformation. Fig 6.1 (B) illustrates a spontaneous structural diagram of a slightly charged mixture,[27, 31] where a small amount of charged long-chain lipid, dimyristoyl phosphatidyl glycerol (DMPG) is added to the system. The resultant structures are different from those in the corresponding zwitterionic system as indicated that the multilamellar vesicles (MLVs) completely unbind into either perforated lamellae or unilamellar vesicles (ULVs) which are reasonably uniform with radii ranged from 15 to 50 nm.[34-35] The objective of this chapter is to testify the ability of nanodiscs to encapsulate the AuNPs without a disruption of morphology for a possible bio-diagnosis sensor based on the principle of self-assembly.

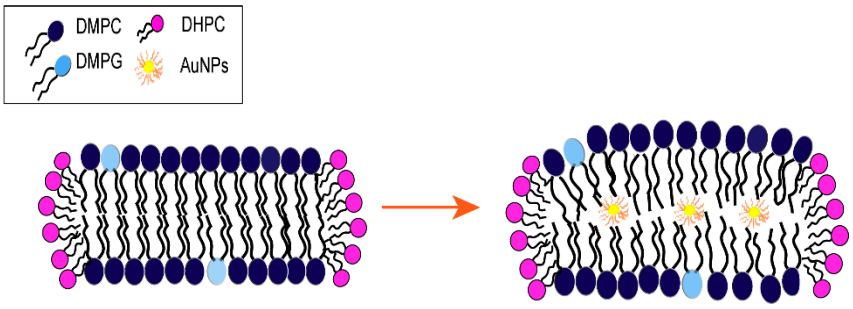

Fig. 6.2. The possible structures of Au/Lipid nanocomplexes at low-T (10^{o}C)

6.2. Experimental

Materials and solutions preparations:

DMPC, DHPC and DMPG were purchased from Avanti Polar Lipids and used without further purification. The molar ratios of long-to-short (Q) and charge-to-non charged lipids (R) are prepared at 3.5 and 0.02, respectively, which yields a disc-like morphology at 10^{o}C.[31] The different carbon chain lengths of AuNPs (i.e. C4, C8, C12, C16 and C18, respectively) were synthesized by Dr. Flavio Maran's research group (University of Padova, Italy), which contain a hydrophobic surface. The initial concentration of AuNPs was prepared in the benzene with 0.25 wt. % and 20ul of AuNPs solution mixed with lipids mixtures of DMPC, DMPG and DHPC together in chloroform, leading to 5 AuNPs per nanodics. After all solutes are well-dispersed in organic solvents, the mixture was dried with a gentle stream of nitrogen and full vacuum for overnight. The thin films of lipid mixtures and AuNPs were dispersed in 0.1mL of water (20 wt. %) to form the nanodiscs at low T (~ 10 ^{o}C) and diluted to 0.5 wt. % before characterizations.

Characterization:

Small Angle X-ray Scattering (SAXS): The size and morphology of lipid mixtures and AuNPs were determined by the SAXS (Nanostar, Bruker). The attainable minimum q (scattering vector) is from 0.07/nm to 0.2/nm. The λ of 1.5418A^{o} was used in this experiment.

High-Resolution Transmission Electron Microscopy (HR-TEM)

The morphology and the presence of AuNPs in lipids mixture were confirmed by HR-TEM (JEM-2010, JEOL) with an accelerating voltage of 200 kV. The negative staining TEM was conducted in following steps. A 5 μL of solution (0.5mg/mL) was placed on a copper grid coated with Formvar/carbon film for one minute and excessive solution being removed by filter paper. Right after, the sample was negatively stained with 5 μL of Uranyl acetate solution in water (20 mg/mL) and the excessive staining solution was again removed. Afterwards, the grid was dried at vacuum for an hour. All this procedure was done below T_M of DMPC (24^{o}C) to prevent the specimen from changing a morphology.

Dynamic Light Scattering (DLS)

DLS is used to determine the R_h of particle with ALV compact goniometer system (CGS-3MD). The λ of 632.8 nm has used with a 22 mW He–Ne laser.

6.3. Results and Discussion

6.3.1 Determination of size of hydrophobated AuNPs

To resolve the size of the hydrophobated AuNP (C12), SAXS is introduced in this study. Recall the chapter 3, the scattering intensity, I, can be presented as a function of scattering vector, q which is defined as $4\pi/\lambda$ [sin $(\theta/2)$], where λ and θ are the wavelength of the X-ray and scattering angle, respectively. Fig.6.3 shows the Guinier plot from the SAXS results of the hydrophobic AuNPs in benzene, where $q\langle R_G^2\rangle^{1/2} \ll 1$ and log I linearly decreases with q^2. The slope of the fitted line is $\langle R_G^2\rangle/3$, resulting in the best fit $\langle R_G^2\rangle^{1/2}$ = (0.92 ± 0.10) nm. Also, the complimentary method of TEM was also conducted to examine its size and distribution and shown in Fig.6.4. All results indicates no indication of large aggregates of AuNPs.

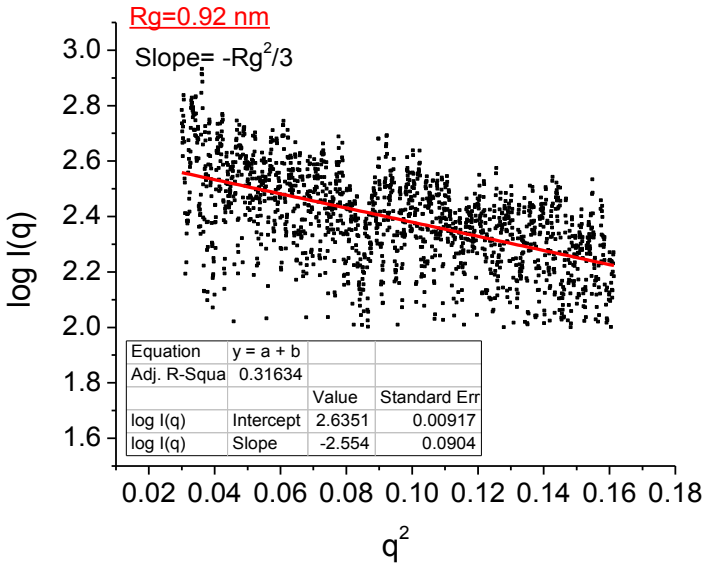

Fig. 6.3. SAXS results of the hydrophobated C12 AuNPs in benzene and the best Guinier fit

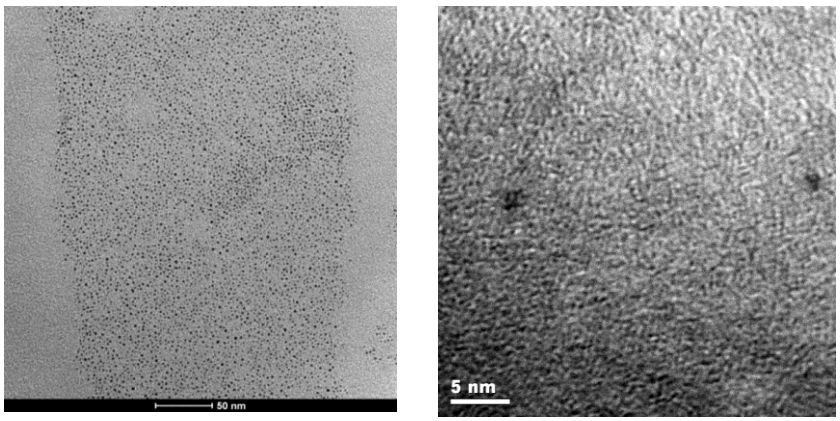

Fig.6.4. HR-TEM of hydrophobated AuNPs (C12) at different scale bars of 50 nm and 5 nm

6.3.2. Incorporation of AuNPs in the Lipid Bilayers

Since it has reported that the DMPC/DMPG/DHPC solutions in absence of AuNPs at 10 ^{o}C form nanodisc,[29, 31, 34, 36] the same disc-like morphology is assumed for the system in presence of AuNPs. To extract the detailed dimensions of morphology from the SAXS data, a new combined model has been designed in this chapter with a core-shell cylinder model as a form factor and the Hayter-Penfold model as a structure factor which describes the interaction between charged particles.[37] The SAXS data then were best fit using this combined model to obtain the average radius and the thickness of the nanodiscs as well as the change in the electron density of the bilayer core. As shown in Fig 6.5, the best fits are in good agreement with the data. The best fitting radii of nanodiscs in absence and presence of AuNPs are (10.5 ± 1.0) and (9.5 ± 1.0) nm, respectively. Two noteworthy results were (1) the best fitting bilayer thickness varied from (4.5 ± 0.6) to (5.3 ± 0.6) nm after the incorporation of AuNPs, consistent with the shift of the high-q

peak toward lower q, and (2) the difference of the electron densities in Table 6.1 between the core and the shell drops by 40%, indicating that the entrapped AuNPs enhance the electron density of the hydrophobic regime significantly.

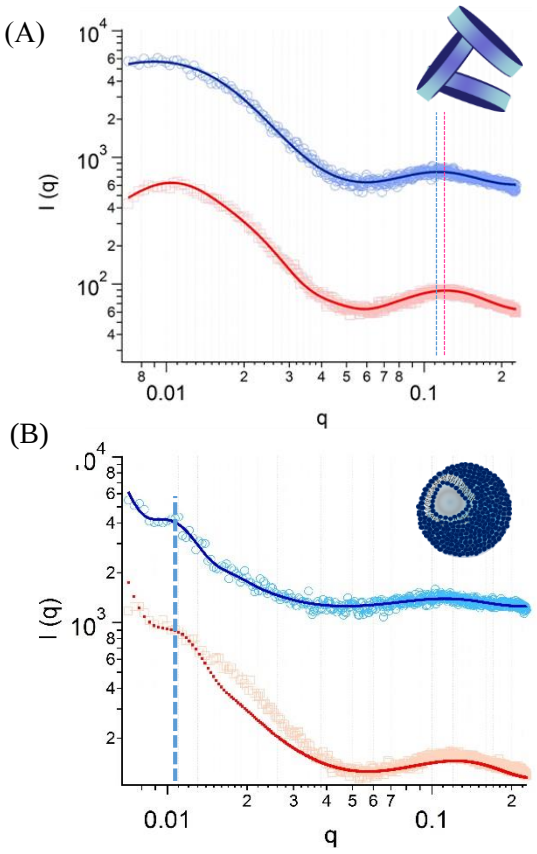

Fig.6.5. SAXS results of lipids [red] and lipids with hydrophobatd AuNPs (C12) [blue] at (A) 10°C and (B) 40°C

	Lipids	Lipids with AuNPs
SLD core ($Å^{-2}$)	-2.33E-04	-1.14E-04

Table 6.1. Best fitted SAXS results of scattering length density (SLD) of hydrophobic core in the disc

The nanodiscs → ULV transition induced by increased T was also examined in the AuNP/lipid solution. Fig 6.5 (B) shows the SAXS data of the same lipid mixtures in absence and presence of AuNPs at 40 ^{o}C. The scattering patterns are clearly different from those of the low-T (10 ^{o}C) samples – an indication of the structural transformation. The broad peak at low q (the structure factor) was replaced by one or two weak oscillations along the curve corresponding to the regular diameter of spontaneously forming ULVs. Moreover, the oscillations take place at similar q values for both samples, indicative of similar ULV sizes. A three-layer (hydrophilic-hydrophobic-hydrophilic) spherical shell model was applied to fit both SAXS data. The best fit agrees with the SAXS data well for the sample with AuNPs, while the SAXS data of the sample without AuNPs could not be fitted by the same model. The discrepancy was presumably attributed to the residue of nanodiscs, which did not transform into ULVs completely - consistent with a previous report for a higher charge-density system.[29] The best-fit vesicular radii in both samples are similar [i.e., around (380±20) Å], consistent with the notion that both oscillations take place at similar q values (dotted line in Fig 6.5 (B)). The radii of ULVs has incresed significantly

compared to that of nanodiscs at 10°C. In a same manner, DLS results of Fig. 6.6) show a increased R_H from 8 nm to 11 nm and the enhanced scattering intensity after increased T in both of lipids and C12AuNPs with lipids.

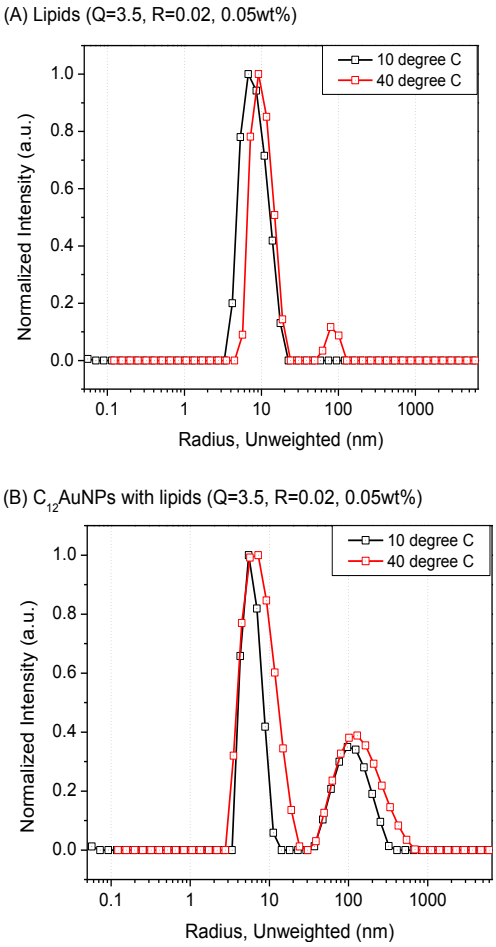

Fig. 6.6. The R_h of (A) lipids mixtures (B) C12AuNPs with lipids mixtures at different temperature of 10°C and 40°C

The effects of AuNPs on the R_h and scattered intensity were observed in Fig.6.6 (B) and (D). Two peaks of R_h around 10 nm and 100 nm, respectivley become more obvious in presence of AuNPs and a spicky

scattered intensity was shown regardless of T, possibly driven by the plasmonic effect of AuNPs.

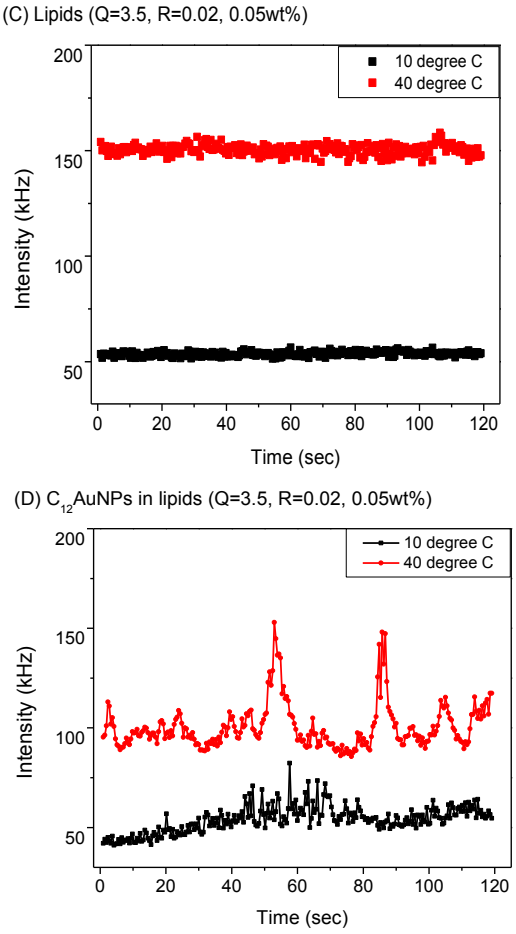

Fig. 6.6. The scattering intensity of (C) lipids mixtures (D) C12AuNPs with lipids mixtures at different temperature of 10°C and 40°C

In addition to the SAXS and DLS data, HR-TEM results of Fig. 6.7 directly show the incorporation of AuNPs into lipid bilayers. Note that uranium and gold have high atomic numbers of 92 and 79, respectively. Therefore, a phase contrast can be aroused from the interference of the beam with different atoms resulting in the different periodicities of d-spacing in the image. As a result, uranyl acetate shows a d-spacing of 0.317 nm and also

AuNPs in a nanodiscs exhibits the d- spacing of 0.212 nm, further confirming the entrapment of AuNPs in the lipid bilayer.

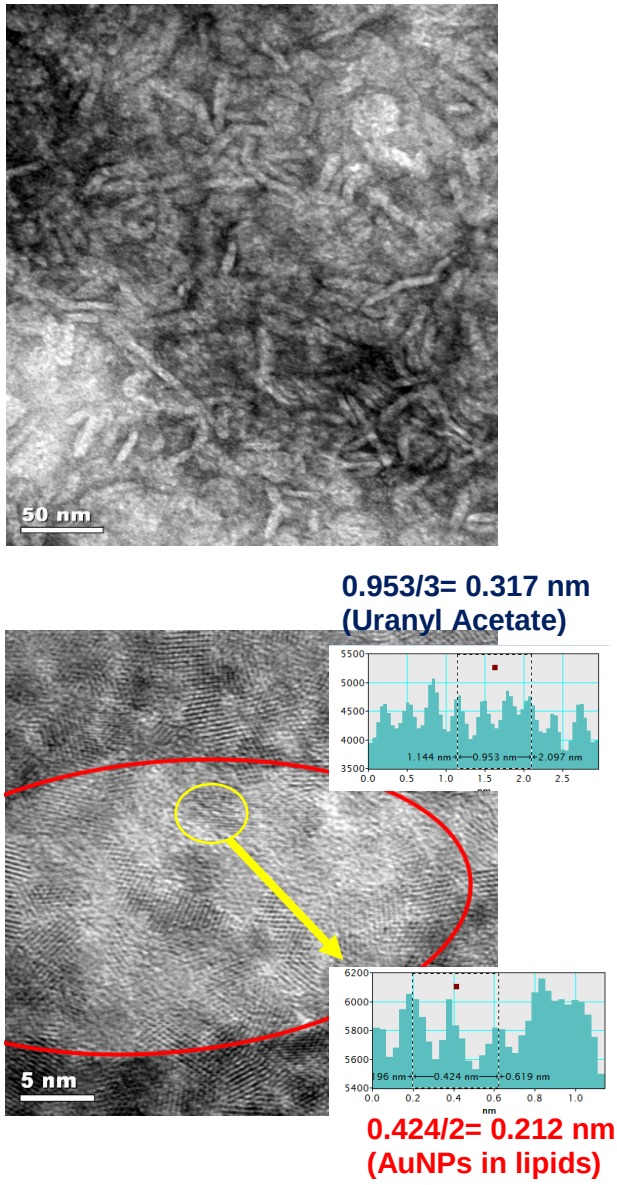

Fig. 6.7. HR-TEM of (a) Nanodiscs composed of DMPC/ DHPC /DMPG (b) Nanodicss with hydrophobatd AuNPs (C12)

6.4. Conclusion

The incorporation of hydrophobated AuNPs into the lipids bilayer composed of DMPC/ DMPG/ DHPC was examined through SAXS and HR-TEM. The results show that the insertion of 1-nm hydrophobated AuNPs in lipids bilayers was successful without severe disruptions of morphology (i.e. nanodisc, ULV). After the incorporation of AuNPs into the bilayer, the increased bilayer thickness and electron density in the hydrophobic core were observed. Further study will be investigated with different sizes of AuNPs, lengths of lipids, and maximum number density of AuNPs in the lipids cargo (i.e. nanodics, ULVs).

6.5. References

1. Mieszawska, A. J.; Mulder, W. J.; Fayad, Z. A.; Cormode, D. P., Multifunctional gold nanoparticles for diagnosis and therapy of disease. *Molecular pharmaceutics* **2013,** *10* (3), 831-846.

2. Ahmed, N.; Fessi, H.; Elaissari, A., Theranostic applications of nanoparticles in cancer. *Drug discovery today* **2012,** *17* (17), 928-934.

3. Agasti, S. S.; Rana, S.; Park, M.-H.; Kim, C. K.; You, C.-C.; Rotello, V. M., Nanoparticles for detection and diagnosis. *Advanced drug delivery reviews* **2010,** *62* (3), 316-328.

4. Bhattacharya, R.; Mukherjee, P., Biological properties of "naked" metal nanoparticles. *Advanced Drug Delivery Reviews* **2008,** *60* (11), 1289-1306.

5. Kleinman, S. L.; Sharma, B.; Blaber, M. G.; Henry, A.-I.; Valley, N.; Freeman, R. G.; Natan, M. J.; Schatz, G. C.; Van Duyne, R. P., Structure enhancement factor relationships in single gold nanoantennas by surface-

enhanced Raman excitation spectroscopy. *Journal of the American Chemical Society* **2012,** *135* (1), 301-308.

6. Dong-Kwon, L.; Ki-Seok, J.; Jae-Ho, H.; Hyoki, K.; Sunghoon, K.; Yung Doug, S.; Jwa-Min, N., Highly uniform and reproducible surface-enhanced Raman scattering from DNA-tailorable nanoparticles with 1-nm interior gap. *Nature Nanotechnology* **2011,** *6* (7), 452-460.

6. Basu, S.; Pande, S.; Jana, S.; Bolisetty, S.; Pal, T., Controlled interparticle spacing for surface-modified gold nanoparticle aggregates. *Langmuir* **2008,** *24* (10), 5562-5568.

8. Bao, L. L.; Mahurin, S. M.; Liang, C. D.; Dai, S., Study of silver films over silica beads as a surface-enhanced Raman scattering (SERS) substrate for detection of benzoic acid. *Journal of Raman Spectroscopy* **2003,** *34* (5), 394-398.

9. Félidj, N.; Aubard, J.; Lévi, G.; Krenn, J.; Salerno, M.; Schider, G.; Lamprecht, B.; Leitner, A.; Aussenegg, F., Controlling the optical response of regular arrays of gold particles for surface-enhanced Raman scattering. *Physical Review B* **2002,** *65* (7), 075419.

10. Wang, M.-H.; Hu, J.-W.; Li, Y.-J.; Yeung, E. S., Au nanoparticle monolayers: preparation, structural conversion and their surface-enhanced Raman scattering effects. *Nanotechnology* **2010,** *21* (14), 145608.

11. Yan, H.; Lim, S. I.; Zhang, L.-C.; Gao, S.-C.; Mott, D.; Le, Y.; Loukrakpam, R.; An, D.-L.; Zhong, C.-J., Rigid, conjugated and shaped arylethynes as mediators for the assembly of gold nanoparticles. *Journal of Materials Chemistry* **2011,** *21* (6), 1890-1901.

12. Lim, D. K.; Jeon, K. S.; Kim, H. M.; Nam, J. M.; Suh, Y. D., Nanogap-engineerable raman-active nanodumbbells for single-molecule detection. *Nature Materials* **2010,** *9* (1), 60-66.

13. Gordon, R.; Sinton, D.; Kavanagh, K. L.; Brolo, A. G., A new generation of sensors based on extraordinary optical transmission. *Accounts of chemical research* **2008,** *41* (8), 1049-1056.

14. Kundu, S., A new route for the formation of Au nanowires and application of shape-selective Au nanoparticles in SERS studies. *Journal of Materials Chemistry C* **2013,** *1* (4), 831-842.

15. Indrasekara, A. S. D. S.; Paladini, B. J.; Naczynski, D. J.; Starovoytov, V.; Moghe, P. V.; Fabris, L., Dimeric Gold Nanoparticle Assemblies as Tags for SERS-Based Cancer Detection. *Advanced Healthcare Materials* **2013,** *2* (10), 1370-1376.

16. Song, J.; Zhou, J.; Duan, H., Self-Assembled Plasmonic Vesicles of SERS-Encoded Amphiphilic Gold Nanoparticles for Cancer Cell Targeting and Traceable Intracellular Drug Delivery. *Journal of the American Chemical Society* **2012,** *134* (32), 13458-13469.

16. Jain, P. K.; Huang, X.; El-Sayed, I. H.; El-Sayed, M. A., Noble Metals on the Nanoscale: Optical and Photothermal Properties and Some Applications in Imaging, Sensing, Biology, and Medicine. *Accounts of Chemical Research* **2008,** *41* (12), 1578-1586.

18. Van Lehn, R. C.; Atukorale, P. U.; Carney, R. P.; Yang, Y.-S.; Stellacci, F.; Irvine, D. J.; Alexander-Katz, A., Effect of Particle Diameter and Surface Composition on the Spontaneous Fusion of Monolayer-Protected Gold Nanoparticles with Lipid Bilayers. *Nano Letters* **2013,** *13* (9), 4060-4066.

19. Tatur, S.; Maccarini, M.; Barker, R.; Nelson, A.; Fragneto, G., Effect of functionalized gold nanoparticles on floating lipid bilayers. *Langmuir* **2013,** *29* (22), 6606-6614.

20. An, X.; Zhan, F.; Zhu, Y., Smart Photothermal-Triggered Bilayer Phase Transition in AuNPs–Liposomes to Release Drug. *Langmuir* **2013,** *29* (4), 1061-1068.

21. Von White, G.; Chen, Y.; Roder-Hanna, J.; Bothun, G. D.; Kitchens, C. L., Structural and Thermal Analysis of Lipid Vesicles Encapsulating Hydrophobic Gold Nanoparticles. *ACS Nano* **2012,** *6* (6), 4678-4685.

22. Preiss, M. R.; Bothun, G. D., Stimuli-responsive liposome-nanoparticle assemblies. *Expert opinion on drug delivery* **2011,** *8* (8), 1025-1040.

23. Binder, W. H.; Sachsenhofer, R.; Farnik, D.; Blaas, D., Guiding the location of nanoparticles into vesicular structures: a morphological study. *Physical Chemistry Chemical Physics* **2007,** *9* (48), 6435-6441.

24. Paasonen, L.; Laaksonen, T.; Johans, C.; Yliperttula, M.; Kontturi, K.; Urtti, A., Gold nanoparticles enable selective light-induced contents release from liposomes. *Journal of Controlled Release* **2007,** *122* (1), 86-93.

25. Park, S.-H.; Oh, S.-G.; Mun, J.-Y.; Han, S.-S., Loading of gold nanoparticles inside the DPPC bilayers of liposome and their effects on membrane fluidities. *Colloids and Surfaces B: Biointerfaces* **2006,** *48* (2), 112-118.

26. Nieh, M.-P.; Raghunathan, V. A.; Pabst, G.; Harroun, T.; Nagashima, K.; Morales, H.; Katsaras, J.; Macdonald, P., Temperature Driven Annealing of Perforations in Bicellar Model Membranes. *Langmuir* **2011,** *27* (8), 4838-4846.

26. Soong, R.; Nieh, M.-P.; Nicholson, E.; Katsaras, J.; Macdonald, P. M., Bicellar Mixtures Containing Pluronic F68: Morphology and Lateral Diffusion from Combined SANS and PFG NMR Studies. *Langmuir* **2009,** *26* (4), 2630-2638.

28. Harroun, T. A.; Koslowsky, M.; Nieh, M.-P.; de Lannoy, C.-F.; Raghunathan, V. A.; Katsaras, J., Comprehensive Examination of Mesophases Formed by DMPC and DHPC Mixtures. *Langmuir* **2005,** *21* (12), 5356-5361.

29. Nieh, M.-P.; Glinka, C. J.; Krueger, S.; Prosser, R. S.; Katsaras, J., SANS study on the effect of lanthanide ions and charged lipids on the morphology of phospholipid mixtures. *Biophysical journal* **2002,** *82* (5), 2487-2498.

30. Nieh, M.-P.; Glinka, C. J.; Krueger, S.; Prosser, R. S.; Katsaras, J., SANS Study of the Structural Phases of Magnetically Alignable Lanthanide-Doped Phospholipid Mixtures. *Langmuir* **2001,** *17* (9), 2629-2638.

31. Katsaras, J.; Harroun, T.; Pencer, J.; Nieh, M.-P., "Bicellar" Lipid Mixtures as used in Biochemical and Biophysical Studies. *Naturwissenschaften* **2005,** *92* (8), 355-366.

32. Diller, A.; Loudet, C.; Aussenac, F.; Raffard, G.; Fournier, S.; Laguerre, M.; Grélard, A.; Opella, S. J.; Marassi, F. M.; Dufourc, E. J., Bicelles: A natural 'molecular goniometer' for structural, dynamical and topological studies of molecules in membranes. *Biochimie* **2009,** *91* (6), 744-751.

33. van Dam, L.; Karlsson, G.; Edwards, K., Direct observation and characterization of DMPC/DHPC aggregates under conditions relevant for biological solution NMR. *Biochimica et Biophysica Acta (BBA) - Biomembranes* **2004,** *1664* (2), 241-256.

34. Nieh, M.-P.; Kučerka, N.; Katsaras, J., Spontaneously formed unilamellar vesicles. *Methods in enzymology* **2009,** *465*, 3-20.

35. Nieh, M.-P.; Harroun, T.; Raghunathan, V.; Glinka, C.; Katsaras, J., Concentration-independent spontaneously forming biomimetric vesicles. *Physical review letters* **2003,** *91* (15), 158105.

36. Nieh, M.-P.; Katsaras, J.; Qi, X., Controlled release mechanisms of spontaneously forming unilamellar vesicles. *Biochimica et Biophysica Acta (BBA)-Biomembranes* **2008,** *1778* (6), 1467-1471.

36. Hayter, J.; Penfold, J., Determination of micelle structure and charge by neutron small-angle scattering. *Colloid and Polymer Science* **1983,** *261* (12), 1022-1030.

Chapter 7.

Self-linked Liposomes with Triblock-copolymer of PPO-PEO-PPO

7.1. Introduction

7.1.1. Liposome

A liposome is a spherical vesicle composed of a lipid bilayer, first characterized by Bangham and co-workers. [1] The lipid bilayer is driven by the hydrophobic force from hydrocarbon chains of the phospholipids.[2-4] In general, the phospholipids generally consist of hydrophobic tails and a hydrophilic head as shown in Fig.7.1. These hydrophobic tails of phospholipids come together and form an inner layer to be shielded from water while the polar head groups hydrated by water, provide a thin outer layer shell.

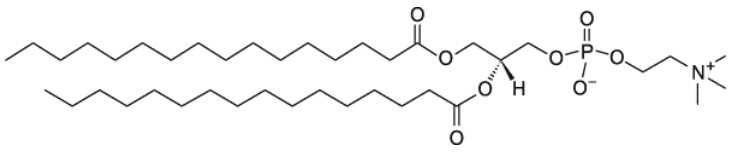

Fig.7.1. The structure of 1, 2-dipalmitoyl-sn-glycero-3-phosphocholine (DPPC), a type of phospholipids

To be more specific, the formation of liposomes requires layer separation and bending. At the initial stage of the liposome formation, two forces,

normal and tangential, play a crucial role in forming a liposome, which cause repulsion between lipid layers and the bending of lipid layers.[5] To prevent an interaction of water with the hydrophobic core of the bilayer at the edges, a self-close of lipid bilayers results in large multilamellar vesicles (MLVs), similar to the structure of onions.[6] These spontaneously formed MLVs can be converted to the single lipid bilayered structure of unilamellar vesicle (ULVs) in Fig. 7.2 by inputting an external energy (i.e., sonication, extrusion) to the system which causes reduction of the particle size. [7-8]

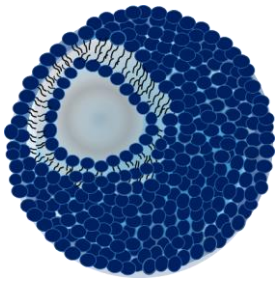

Fig.7.2. the structure of unilamellar vesicle (ULV) composed of phospholipids

As the structure of lipid bilayers is likely similar to biological cell membranes, liposomes have been used as models for cell membranes for drug delivery systems (DDS)[9-10], imaging agents[11-12]. For instance, drug or dye molecules can be incorporated into either an aqueous interior or hydrophobic lipid bilayer in the liposome and easily transported through biological membranes.[13] Also, Liposomes have relatively large internal volume and the ability to modify their outer-membrane with various bio-

recognition elements. All these characteristic make liposomes a versatile tool for bio-sensing and drug delivery.

7.1.2. Triblock copolymer of PPO-PEO-PPO (Pluronic®)

Block copolymers have received much attention due to various properties of molecular architecture and self-assembly. In the area of emulsifiers and stabilizers, the commonly used triblock copolymer with liposomes is PEO-PPO-PEO.[14-15] In this thesis, the inverse case of PPO-PEO-PPO triblock polymers (17R4, Pluronic®), in which PEO is the hydrophilic poly (ethylene oxide) and PPO is the hydrophobic poly (propylene oxide) is used. Fig. 7.3 shows the chemical structure of PPO-PEO-PPO (17R4, Pluronic), which contains 14 repeat units of PPO and 24 repeat units of PEO, respectively. The amount of PEO within PPO-PEO-PPO attributes to 40 wt. %. In water, many of the triblock polymers have been shown to aggregate in the form of micelles with a self-assembled structure of a hydrophobic core (PPO) and hydrated corona (PEO).[16] The magnitude of the aggregation as well as the phase propensity generally depends on the molecular weight and the segment composition of the particular block copolymer.[17] Moreover, the formation of micelles (and other aggregates) has been found to be an extremely temperature-dependent process.[15, 17-19] It has been reported that 17R4 possesses a high critical micelle concentration (CMC) of 0.091g/mL at 40^{o}C but small aggregation number and small micellar radius in water.[18-19] This special characteristic is ascribed to the entropic penalty associated

with the looping geometry of the middle block of PEO.[20]

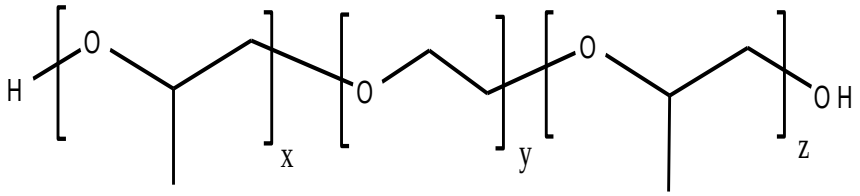

Fig.7.3. The structure of tribolock copolymer (17R4), PPO_x-PEO_y-PPO_z, where x, z are 14 and y is 24.

7.1.3. Objectives

In this chapter, the possibility of self-linked liposomes with a triblock copolymer of PPO-PEO-PPO in water phase will be attempted for the possible platform of bio-diagnosis sensors. The effect of characteristics of liposomes (i.e. defect, charge, curvature of liposomes and concentrations of lipid mixtures) as well as different weight ratios of polymer to liposome on the liposome aggregation will be briefly introduced. This concept may provide basic baselines for developing a successful bio-diagnosis sensor in the future.

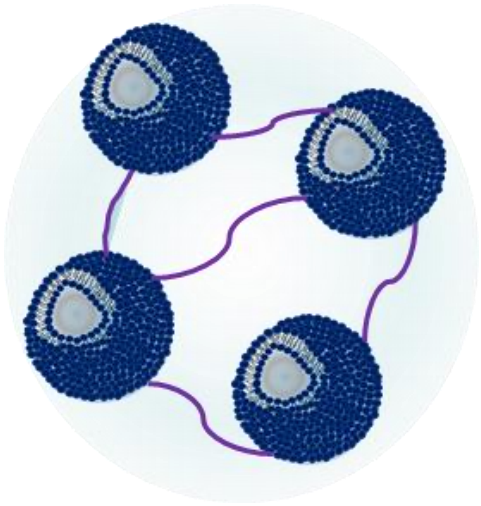

Fig.7.4. The possible structure of self-linked liposomes with triblock copolymer of PPO-PEO-PPO (17R4, Pluronic®)

7.2. Experimental

The different chain lengths and charge of phospholipids [i.e. Dipalmatoyl phosphatidylcholine (DPPC), dihexanoyl phosphatidylcholine (DHPC), and dipalmatoyl phosphatidylglycerol (DPPG)] were purchased from Avanti Polar Lipids (Alabaster, AL) and used without further purification. The triblock copolymer of Pluronics 17R4 (PPO-PEO-PPO) was purchased from Sigma-Aldrich. The concentration of PPO-PEO-PPO was prepared below the CMC (0.091g/mL) and further filtered through a pore size of 0.2μm. To add a defect on the surface of liposomes, different molar ratio of Q ([Long chain lipids (i.e. DMPC, DMPG)]/ [Short chain lipids (i.e. DHPC)]) were prepared at Q= ∞, 10 and 3. Different charge ratios of R ([Charge lipids]/ [Non-charged lipids]) were also introduced from R=0, 0.01 and 0.02, correspondingly. All lipid mixtures were prepared at two concentrations, 0.5 and 0.1 wt. %, and first dispersed in chloroform.

Chloroform was removed under a gentle stream of nitrogen and vacuum. To hydrate the dry lipid film, DI water was added and vortexed vigorously above 40°C. The lipid mixtures were then subjected to bath-sonication and freeze thaw cycles at least 4 times. Lastly, the varying size of liposomes are produced by using the mini-extruder (Avanti®) with different pore sizes (i.e. 100nm, 50nm and 30nm) of polycarbonate filters above the T_m of lipid mixtures. After the liposome is prepared, in general, a fixed weight ratio of polymer to liposome (i.e. 1 to 1) was introduced for the aggregation of liposomes with the exception of some cases which will be discussed in section 7.3.3.

Light Scattering: The Dynamic Light Scattering technique, also known as photon correlation spectroscopy (PCS) was used to determine the size and aggregation of liposomes at 25°C which are driven by diffusion coefficients of the liposomes based on the Stokes-Einstein equations as shown in Eqn.7.1. In this experiment, a compact goniometer of ALV CGS 3MD was used with the fixed angle of 90°. The laser source has a power of 22 mW and produces a wavelength of 632.8 nm.

$$D = \frac{kT}{6\pi\eta R} \qquad \text{Eqn. 7.1}$$

where D is diffusion coefficients, k is Boltzmann constant, T is temperature (K), η is the viscosity of medium and R is the hydrodynamic radius of particles

7.3. Results and Discussion

7.3.1. Effect of defects

In order to vary the defects and elasticity of liposomes, different mole ratios (Q) of long-(DPPC) to short chain (DHPC) lipids was introduced from ∞, 10 and 3, respectively at a fixed concentration (0.5 wt. %) of lipids mixtures. Fig. 7.5 and 7.6 show that increasing defects on the liposome with the short chain phospholipids of DHPC, obvious aggregation of liposomes was observed as a function of time with PPO-PEO-PPO. The pronounced impact of defects on the aggregation of liposomes was shown at Q=3. The aggregation of liposomes with PPO-PEO-PPO is possibly driven by a hydrophobic force from the PPO blocks in the triblock copolymer in water phase.

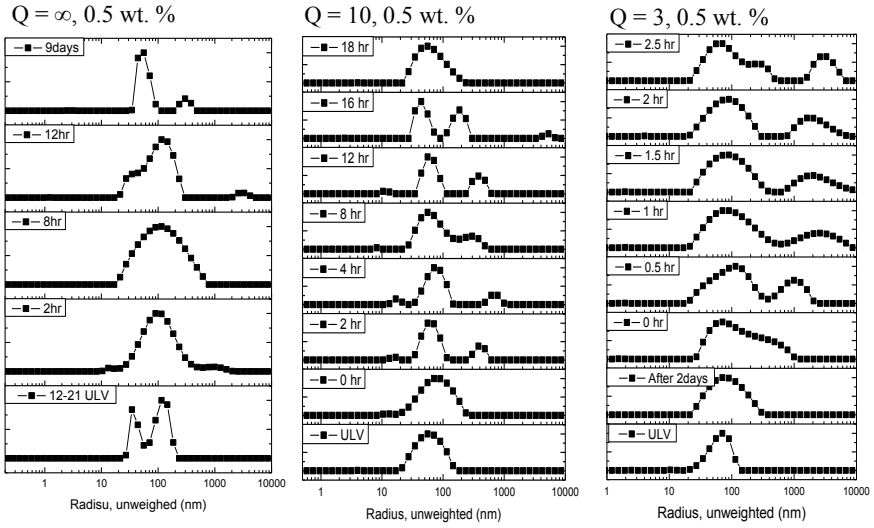

Fig. 7.5.. The R_h of liposomes with different ratio of Q (i.e. ∞, 10 and 3) with PPO-PEO-PPO as a function of time at fixed concentrations of 0.5 wt. % of lipids and 0.5 wt. % of polymer in DI water

It is speculated that the defects of the liposome provide the PPO blocks with an enhanced local surface area to interact with hydrophobic tails of lipids. Also, the different melting temperature of DPPC and DHPC may affect elasticity on the surface of the liposome which is possible to induce a loose packing and less resistance to stretching and bending on the liposome.[21] In fact, while the DHPCs exist in a melting phase at 25^{o}C, DPPCs are in a rigid phases due to its relatively high T_M of 41^{o}C. Therefore, it is possible that the DHPC induces the facilitated interactions between PPO and acyl chains of DPPC in the water phase. However, the stability of the liposome remains unclear in this study. The representative instability of liposome as a function of time is shown in Fig. 7.7. The instability of liposome has a tendency to appear at high concentrations of lipid mixtures, below the T_M

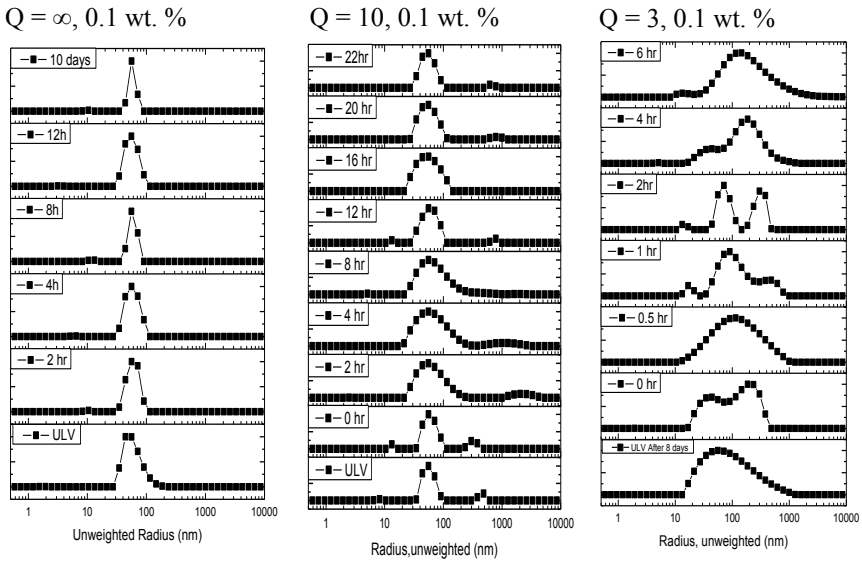

Fig. 7.6 The R_h of liposomes with different ratio of Q (i.e. ∞, 10 and 3) with PPO-PEO-PPO as a functions of time at fixed concentration of 0.1 wt. % of lipids and 0.1 wt. % of polymer in DI water

of DPPC, large size and high defects of liposome (i.e. high content of DHPC). Even though there is the possibility of MLV formation which may relate to other types of aggregations, in general, it tends to form more aggregates of liposomes with PPO-PEO-PPO in the presence of defects on the liposome. Indeed, a fast kinetic liposome aggregation was observed at a high concentration (0.5 wt. %) of lipid mixtures compared to that of a low concentration (0.1 wt. %). This may relate to a collision frequency between PPO-PEO-PPO and liposomes. The more detailed experiments will be introduced in part of 7.3.3. The possibility of MLV formation in the case of 0.1 wt. % liposome may also facilitate the aggregation with PPO-PEO-PPO in Fig.7.5. However, this part will be explored in future study.

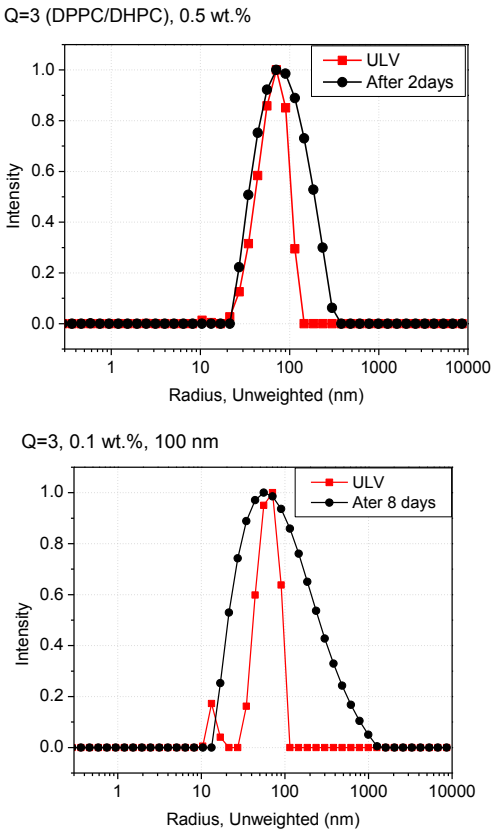

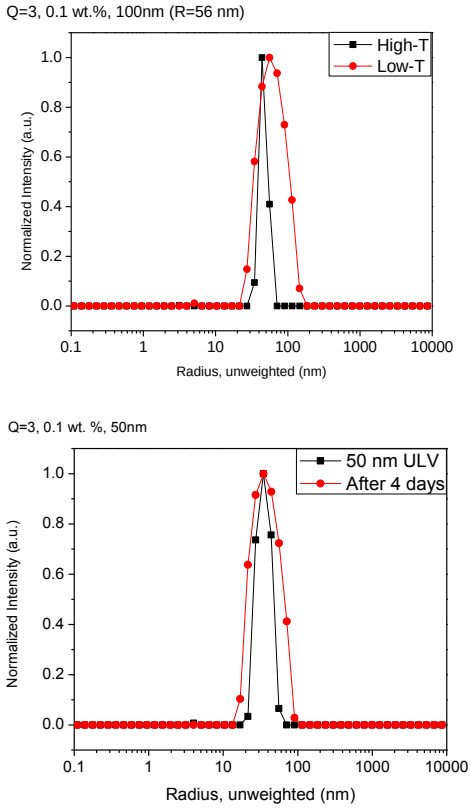

Fig. 7.7. The change of R_h of liposomes by time, size, concentrations and temperature above and below T_M of DPPC.

7.3.2. Effect of charge

It is known that a negatively charged phospholipid such as DPPG in the bilayer helps to stabilize the morphology composed of DPPC/DHPC in the water phase due to its enhanced Coulombic repulsion forces.[22] Since the instability of the DPPC or DPPC/DHPC liposomes as a function of time was observed, the negatively charged DMPG was introduced to the lipid bilayer of DPPC and DPPC/DHPC from R=0, 0.01 and 0.02, respectively to examine its effects on interaction with PPO-PEO-PPO for the liposome aggregation and negate the possibility of other types of aggregation. Fig.

7.8 and 7.9 illustrate the R_h of liposome with PPO-PEO-PPO corresponding to the time, showing that once charge is included

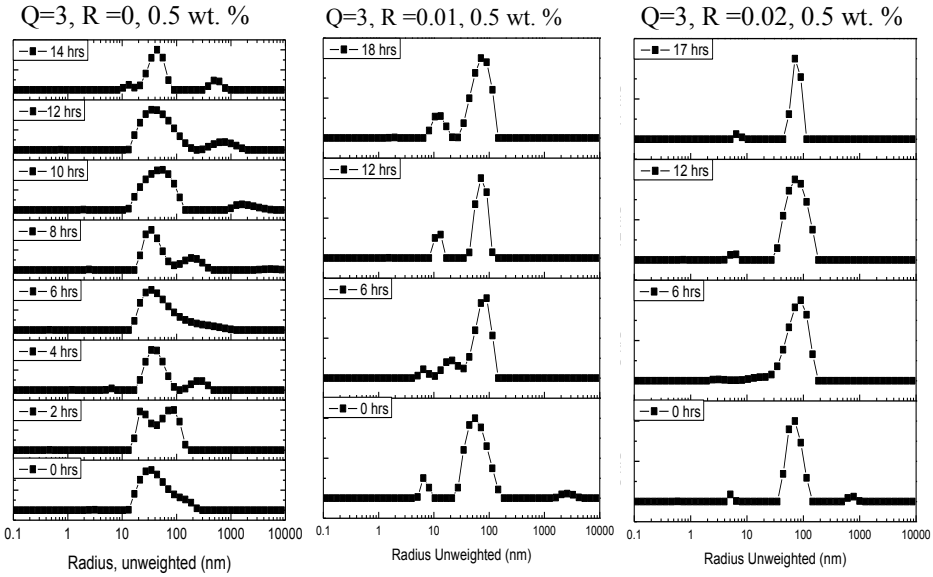

Fig. 7.8. The R_h of liposomes with different ratio of R (i.e. 0, 0.01 and 0.02) at Q=3 with PPO-PEO-PPO as a functions of time at fixed concentration of 0.5 wt. % of lipids and 0.5 wt. % of polymer in DI water

in the liposome surfaces, no distinct aggregation was observed regardless of concentrations and defects of liposomes. This is probably because of a repulsion force between DPPG on the liposome surface and PEG block of the triblock copolymer. Many studies proved that PEG, which can also enhance steric and repulsion forces, resulted in a long blood circulation time with a reduced reticuloendothelial system (RES) uptake.[23-24] Hence, the effect of charge on the liposome surface may cancel out the hydrophobic force between lipid bilayer and PPO block resulting in no aggregation of liposomes.

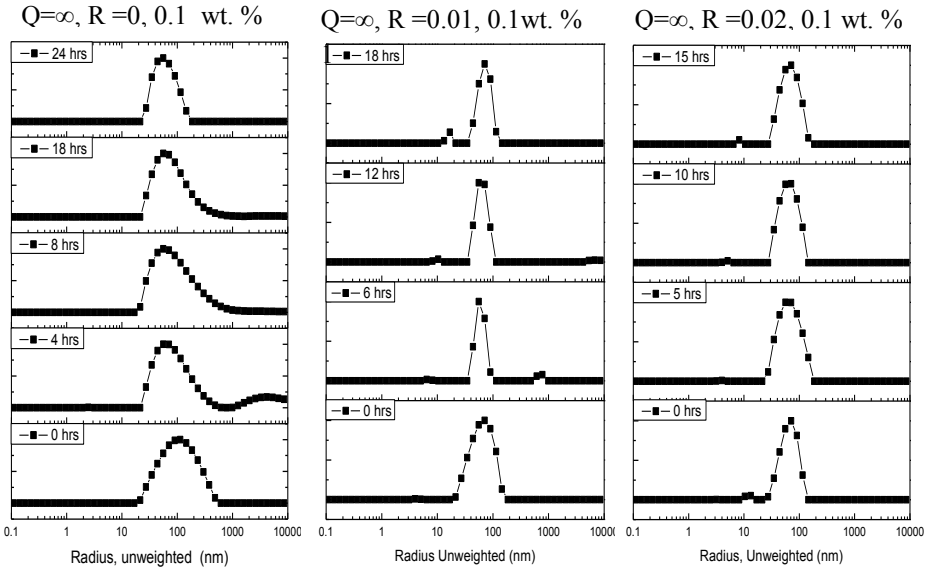

Fig. 7.9. The R_h of liposomes with different ratio of R (i.e. 0, 0.01 and 0.02) at Q=∞ with PPO-PEO-PPO as a functions of time at fixed concentration of 0.1 wt. % of lipids and 0.1 wt. % of polymer in DI water

7.3.3. Effect of number of density of liposomes and weight ratio of polymer to liposomes

The interaction between liposome and PPO-PEO-PPO was investigated through the utilization of different sized liposomes and weight ratios of polymer to liposome. Fig. 7.10 illustrates the kinetics of different sized o liposomes ranging from 30, 50, 100 and 200nm with a fixed weight ratio of polymer to lipids of 1:1. Note that a larger size of liposome takes more surface area to interact with polymer. However, the aggregation of liposomes with polymer was shown in the case of relatively smaller sized liposomes (i.e. 30nm and 50nm). This suggests that there is an importance of number density of liposomes to interact with polymer in the water phase.

The bilayered liposome contains two outer and inner layers exposed to water phase, respectively. The thickness of the bilayers is about 5 nm and the surface area of hydrophilic head group in the phospholipids is around 0.65 nm^2. Therefore the number of lipids composing the liposome can be driven by dividing the total surface area of lipid bilayer with the individual surface area of lipids. Also, at a given mole concentration of lipids in the solution, the number of phospholipids was calculated with Avogadro's constant. After combining all the information, the number of liposomes with different sizes (i.e. 30 nm, 50 nm, 100 nm and 200 nm) in a given concentration of lipids mixtures of 0.1 wt. % and 0.5 wt. % was calculated and plotted in Fig.7.11. As the size of liposomes become smaller, the number of liposomes increase from 2 to 6 times in a fixed concentration of 0.1 wt. %. In a same manner, the number of polymers in 0.1 wt. % solution was evaluated in Table 7.1, showing an increase of at least ~ 4 orders of magnitude higher than that of liposomes. [In previous, different ratios of polymer to liposome was attempted from 0.001 wt. % to 1 wt. % in the case of 100 nm. No clear aggregation was observed. (Data not shown)] Hence, this result indicates that the increased number of liposomes with reduced size may enhance a collision frequency to interact with polymer and reduce the intermolecular distance of liposomes.

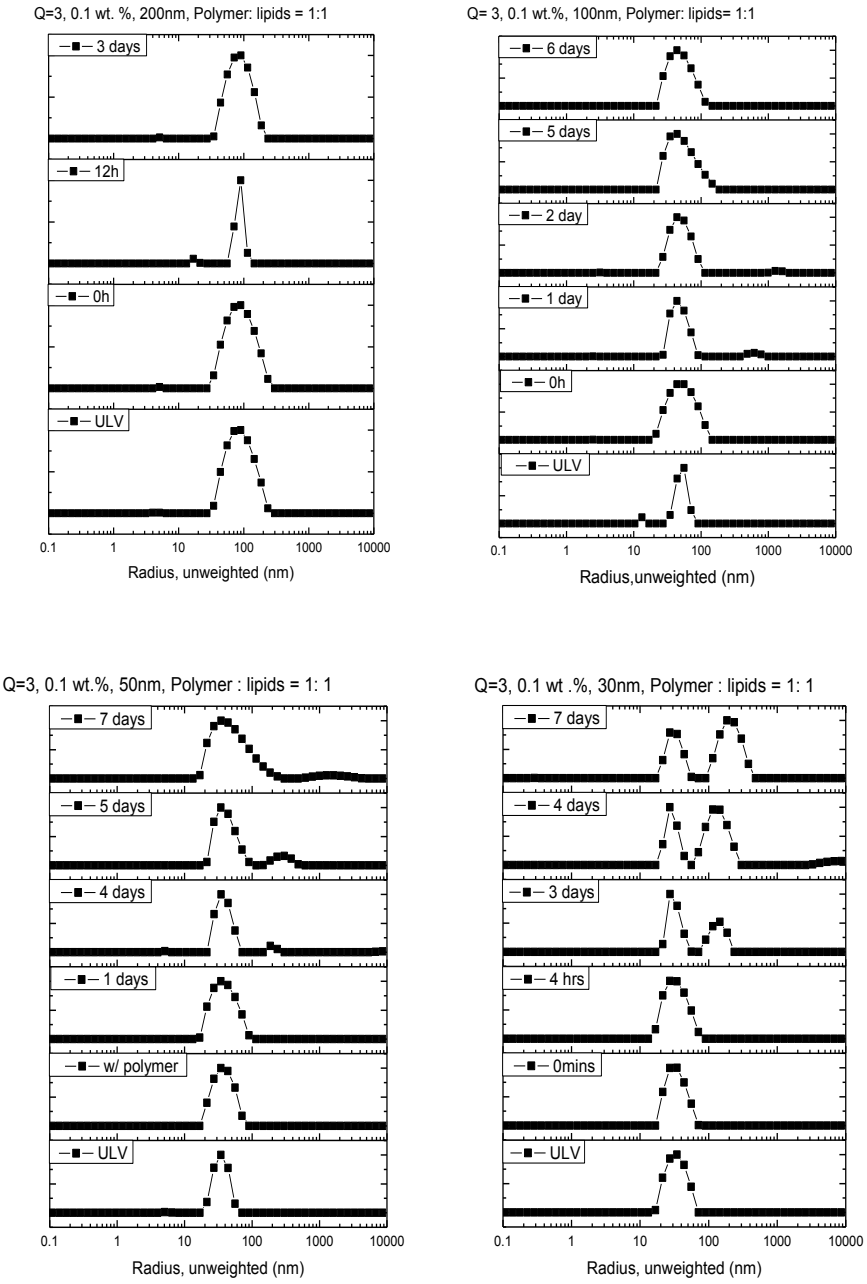

Fig. 7.10. The kinetics of different sizes of liposomes (i.e. 30, 50, 100 and 200 nm) at fixed concentration of 0.1 wt. % of lipids and 0.1 wt. % of PPO-PEO-PPO in DI water

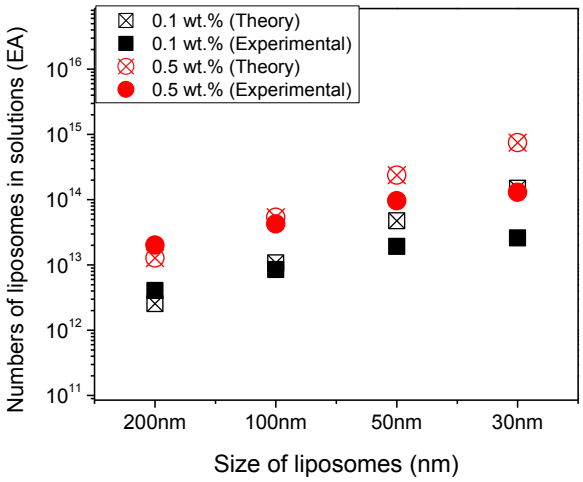

Fig. 7.11. The calculated numbers of liposomes in different sizes of liposomes. (The experimental size of liposome shows a deviation from the theoretical size of liposome after the extrusions, resulted in the differences of number of liposome in the aqueous solution.)

To support this speculation, an increase in the amount of polymer to larger size of liposomes (i.e. 100 nm and 200 nm) from 2 to 4 and illustrated in Fig. 7.12 was attempted. The aggregation of liposomes was shown in the case of 100 nm as increasing the weight ratio of polymer to liposome up to 2, indicating that the probability of interactions between liposome and polymer plays an important role in resulting aggregation in the system. However, no obvious aggregation was shown in the case of 200 nm liposome with polymer ratio up to 4 even after 3 days, implying that either kinetic liposome aggregation is too slow or there are certain barriers of inter-particle distances to link between polymer and larger sized liposomes. Further study will be investigated to prove this point.

	Number of PPO-PEO-PPO in 1mL	
Mw 2700	0.1wt.%	0.5wt. %
EA	2.2304E+17	1.11519E+18

Table 7.1 The calculated numbers of PPO-PEO-PPO in the case of 0.1 wt. % and 0.5 wt. % in DI water

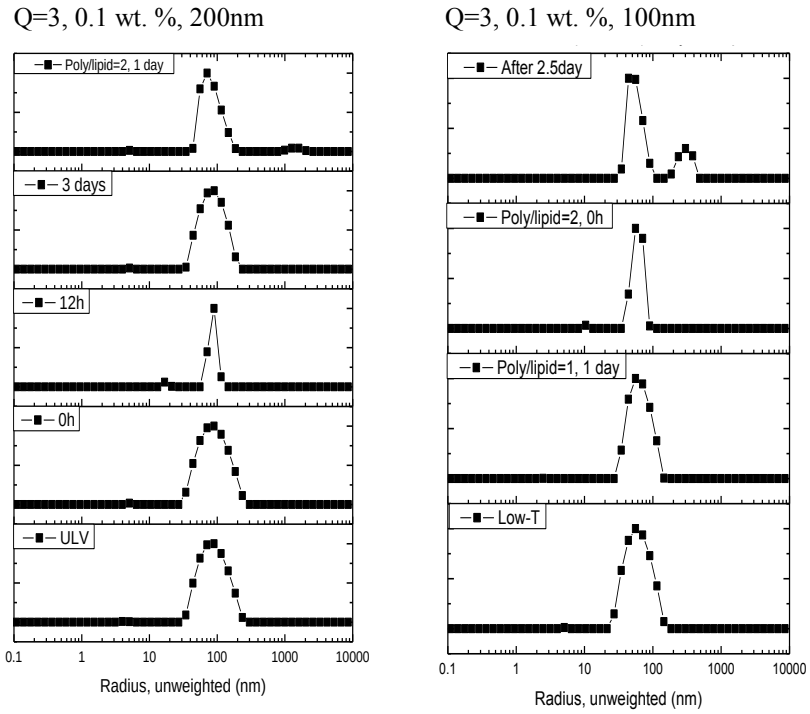

Fig. 7.12. The kinetics of liposome aggregations with different polymer weight ratio to lipids

7.4. Conclusion

The possibility of a self-linked liposome with triblock copolymer of PPO-PEO-PPO was first attempted with different concentrations of lipids mixtures, charge, defects on the liposome surface and sizes of liposomes. Also, the different stoichiometric ratios of polymer to liposome were

investigated to understand the interactions between polymer and liposome. The results show that the DHPC plays an important role in providing defects and elasticity to the DPPC liposome and facilitating the interactions with hydrophobic PPO in the polymer. However, the aggregation of liposome was impeded once the negative charged DMPG was added onto the liposome surface, probably due to the increase of repulsion force between DMPG and PEO block in the polymer. Also, the hydrophobic interaction between PPO blocks and lipid bilayer is affected by the number density of liposome and/or polymer in the water. While smaller sizes of liposomes, 30nm and 50nm, show an obvious aggregation in the presence of PPO-PEO-PPO in a relatively short time, larger sizes of liposome, 100 nm and 200 nm, require extra polymer to shorten the kinetics for liposome aggregations in the water. However, the trends of liposome instability were observed at a high concentration of lipid mixtures, below the T_m of DPPC, large size and high defects of liposome. Further study is needed to resolve these issues.

7.5. References

1. Bangham, A. D.; Horne, R. W., Negative staining of phospholipids and their structural modification by surface-active agents as observed in the electron microscope. *Journal of Molecular Biology* **1964,** *8* (5), 660-IN10.

2. Israelachvili, J. N.; Mitchell, D. J.; Ninham, B. W., Theory of self-assembly of hydrocarbon amphiphiles into micelles and bilayers. *J. Chem. Soc., Faraday Trans. 2* **1976,** *72*, 1525-1567.

3. Israelachvili, J. N., *Intermolecular and Surface Forces*. Elsevier Science: **2010**.

4. Kent, C., Eukaryotic Phospholipid Biosynthesis. *Annual Review of Biochemistry* **1995,** *64* (1), 315-343.

5. Bagatolli, L. A.; Gratton, E., A correlation between lipid domain shape and binary phospholipid mixture composition in free standing bilayers: A two-photon fluorescence microscopy study. *Biophysical Journal* **2000,** *79* (1), 434-447.

6. Brandl, M., Liposomes as drug carriers: a technological approach. In *Biotechnology Annual Review*, Elsevier: **2001**, pp 59-85.

7. Papahadjopoulos, D.; Miller, N., Phospholipid model membranes. I. Structural characteristics of hydrated liquid crystals. *Biochimica et Biophysica Acta (BBA) - Biomembranes* **1967,** *135* (4), 624-637.

7. Szoka Jr, F.; Papahadjopoulos, D., Comparative properties and methods of preparation of lipid vesicles (liposomes). *Annual review of biophysics and bioengineering* **1980,** *9* (1), 467-507.

9. Allison, A. C.; Gregoriadis, G., *Liposomes in biological systems*. J. Wiley: **1980**.

10. Chonn, A.; Cullis, P. R., Recent advances in liposomal drug-delivery systems. *Current Opinion in Biotechnology* **1995,** *6* (6), 698-707.

11. Torchilin, V. P., Liposomes as delivery agents for medical imaging. *Molecular Medicine Today* **1996,** *2* (6), 242-249.

12. Matteucci, M. L.; Thrall, D. E., The role of liposomes in drug delivery and diagnostic imaging: A review. *Veterinary Radiology & Ultrasound* **2000,** *41* (2), 100-107.

13. Allen, T. M., Liposomal drug delivery. *Current Opinion in Colloid & Interface Science* **1996,** *1* (5), 645-651.

14. Mortensen, K., PEO-related block copolymer surfactants. *Colloids and Surfaces A: Physicochemical and Engineering Aspects* **2001,** *183–185* (0), 277-292.

15. Alexandridis, P.; Alan Hatton, T., Poly(ethylene oxide)‧ poly(propylene oxide)‧ poly(ethylene oxide) block copolymer surfactants in aqueous solutions and at interfaces: thermodynamics, structure, dynamics, and modeling. *Colloids and Surfaces A: Physicochemical and Engineering Aspects* **1995,** *96* (1–2), 1-46.

16. Mortensen, K., Phase Behaviour of Poly(ethylene oxide)-Poly(propylene oxide)-Poly(ethylene oxide) Triblock-Copolymer Dissolved in Water. *EPL (Europhysics Letters)* **1992,** *19* (7), 599.

17. Alexandridis, P.; Holzwarth, J. F.; Hatton, T. A., Micellization of poly (ethylene oxide)-poly (propylene oxide)-poly (ethylene oxide) triblock copolymers in aqueous solutions: thermodynamics of copolymer association. *Macromolecules* **1994,** *27* (9), 2414-2425.

17. Chu, N. Y. C.; Kawaoka, K.; Kearns, D. R., Investigation of Energy-Transfer Mechanisms in Pyrene Crystals. *The Journal of Chemical Physics* **1971,** *55* (7), 3059-3067.

19. Huff, A.; Patton, K.; Odhner, H.; Jacobs, D. T.; Clover, B. C.; Greer, S. C., Micellization and Phase Separation for Triblock Copolymer 17R4 in H2O and in D2O. *Langmuir* **2011,** *27* (5), 1707-1712.

20. Ten Brinke, G.; Hadziioannou, G., Topological constraints and their influence on the properties of synthetic macromolecular systems. 2. Micelle formation of triblock copolymers. *Macromolecules* **1987,** *20* (3), 486-489.

21. Saad, S. M. I.; Policova, Z.; Acosta, E. J.; Hair, M. L.; Neumann, A. W., Mixed DPPC/DPPG Monolayers at Very High Film Compression. *Langmuir* **2009,** *25* (18), 10907-10912.

22. Nieh, M.-P.; Glinka, C. J.; Krueger, S.; Prosser, R. S.; Katsaras, J., SANS study on the effect of lanthanide ions and charged lipids on the morphology of phospholipid mixtures. *Biophysical journal* **2002,** *82* (5), 2487-2497.

23. Torchilinl, V.; Papisov, M., Why do polyethylene glycol-coated liposomes circulate so long?: Molecular mechanism of liposome steric

protection with polyethylene glycol: Role of polymer chain flexibility. *Journal of liposome research* **1994,** *4* (1), 725-739.

24. Allen, T., The use of glycolipids and hydrophilic polymers in avoiding rapid uptake of liposomes by the mononuclear phagocyte system. *Advanced drug delivery reviews* **1994,** *13* (3), 285-309.